

UNIVERSITÉ DU QUÉBEC À MONTRÉAL

ÉTUDE DE L'ÉCOULEMENT À FINE-ÉCHELLE AVEC UN LIDAR DOPPLER LORS D'ÉVÈNEMENTS DE
PRÉCIPITATIONS DANS LES ROCHEUSES CANADIENNES EN 2019

MÉMOIRE

PRÉSENTÉ

COMME EXIGENCE PARTIELLE

MAÎTRISE EN SCIENCES DE L'ATMOSPHÈRE

PAR

AURÉLIE DESROCHES-LAPOINTE

OCTOBRE 2023

UNIVERSITÉ DU QUÉBEC À MONTRÉAL
Service des bibliothèques

Avertissement

La diffusion de ce mémoire se fait dans le respect des droits de son auteur, qui a signé le formulaire *Autorisation de reproduire et de diffuser un travail de recherche de cycles supérieurs* (SDU-522 – Rév.04-2020). Cette autorisation stipule que «conformément à l'article 11 du Règlement no 8 des études de cycles supérieurs, [l'auteur] concède à l'Université du Québec à Montréal une licence non exclusive d'utilisation et de publication de la totalité ou d'une partie importante de [son] travail de recherche pour des fins pédagogiques et non commerciales. Plus précisément, [l'auteur] autorise l'Université du Québec à Montréal à reproduire, diffuser, prêter, distribuer ou vendre des copies de [son] travail de recherche à des fins non commerciales sur quelque support que ce soit, y compris l'Internet. Cette licence et cette autorisation n'entraînent pas une renonciation de [la] part [de l'auteur] à [ses] droits moraux ni à [ses] droits de propriété intellectuelle. Sauf entente contraire, [l'auteur] conserve la liberté de diffuser et de commercialiser ou non ce travail dont [il] possède un exemplaire.»

REMERCIEMENTS

Tout d'abord, j'exprime ma gratitude au Conseil de recherche en sciences naturelles et en génie (CRSNG), au Fonds de recherche Nature et technologies du Québec (FRQNT) et au programme de recherche Global Water Future (GWF) pour avoir contribué au financement de ce projet.

Je tiens à offrir mes sincères remerciements aux nombreuses personnes m'ayant apporté leur soutien dans la réalisation de ce projet de maîtrise, en commençant par ma directrice de recherches Pre. Julie M. Thériault qui m'a épaulé tout en me permettant la liberté scientifique encourageant l'initiative. Travailler sous sa supervision m'a également permis de prendre part à la campagne de terrain SPADE 2019 dans les Rocheuses canadiennes, et ainsi de développer une expertise de travail technique et appliquée en collaboration avec une équipe de recherche pancanadienne. Je me dois de remercier spécialement mon co-directeur Zen Mariani, chercheur scientifique (Division de la recherche météorologique, ECCC) sans qui ce projet n'aurait pu être possible. Il m'a généreusement offert de son temps et beaucoup de matériel informatique et académique grâce à quoi j'ai réalisé le traitement des données du lidar.

Je remercie chacune des personnes qui ont contribué au bon déroulement de cette campagne de mesure, notamment la dynamique responsable de projet Juris Almonte, le personnel de ECCC (Environnement et Changement Climatique Canada), aux équipes de UNBC (University of Northern British-Columbia), de USASK (University of Saskatchewan) et de UofM (University of Manitoba).

J'aimerais également remercier le personnel et corps professoral du Centre ESCER de l'UQAM, plus particulièrement l'admirable Eva Monteiro, qui depuis mon arrivée aux études en sciences de l'atmosphère, a su me motiver à travailler toujours plus fort. Finalement, je suis reconnaissante des encouragements et de l'aide importante apportée par mes collègues et mes proches, notamment Nicolas Leroux, Ludovick S. Pelletier, Sara-Ann Piscopo, Priscilla Busseau et Charlie Hébert-Pinard.

AVANT-PROPOS

Être récipiendaires des bourses de recherches du CRSNG et du FRQnt m'a permis une plus grande liberté dans le choix de mon sujet de recherche de maîtrise. Au moment de choisir mon sujet et mon superviseur, j'avais un grand intérêt pour le domaine de la couche limite planétaire, qui a d'ailleurs constitué mon cours préféré du programme de maîtrise. Bien qu'il ne s'agisse pas du domaine d'intérêt principal d'aucun professeur(e) du département des sciences de la Terre et de l'atmosphère à l'UQAM, ceci s'inscrivait bien dans le travail de recherche de la Pre. Julie M. Thériault qui se spécialise sur l'étude des précipitations, avec qui j'avais auparavant eu la chance d'effectuer deux stages de recherches.

Ainsi, au moment de débuter ma maîtrise, la Pre. Julie M. Thériault mettait en œuvre la campagne de terrain SPADE dans les Rocheuses Canadiennes. L'objectif étant d'y étudier les précipitations ainsi que la circulation atmosphérique associées, des lidars Doppler à vents y seraient déployés. J'ai alors été impliquée dans ce projet et ce dans le cadre de mon projet de maîtrise.

Au même moment, dans le cadre du cours de télédétection atmosphériques, je me suis formée sur le fonctionnement et les utilités de ces lidars. Il s'avère qu'ils permettent de mesurer, avec grande précision, les écoulements atmosphériques de la couche limite planétaire. Ainsi, l'étude des vents de fine-échelle, en relation avec les évènements de précipitations de la campagne de terrain SPADE, ont permis de mieux caractériser les écoulements associés aux tempêtes documentées.

TABLE DES MATIÈRES

REMERCIEMENTS	ii
AVANT-PROPOS.....	iii
LISTE DES FIGURES	vi
LISTE DES TABLEAUX	ix
LISTE DES ABRÉVIATIONS, DES SIGLES ET DES ACRONYMES.....	x
LISTE DES SYMBOLES ET DES UNITÉS	xii
RÉSUMÉ.....	xiii
ABSTRACT.....	xiv
SIGNIFICANCE STATEMENT	xv
INTRODUCTION	16
CHAPITRE 1 FINE-SCALE FLOW FIELD AND PRECIPITATION EVENTS IN THE CANADIAN ROCKIES USING DOPPLER LIDARS DURING SPADE-2019.....	26
1.1 INTRODUCTION.....	28
1.2 EXPERIMENTAL DESIGN	32
1.2.1 Overview of the Field Experiment	32
1.2.2 Instrumentation.....	33
1.2.3 Precipitation Events.....	35
1.3 DATA ANALYSIS	36
1.3.1 Quality Control.....	36
1.3.2 Wind Field Retrieval.....	38
1.3.3 Turbulence Characterization.....	39
1.3.4 Atmospheric Water Content.....	41
1.4 OVERVIEW OF THE PRECIPITATION EVENTS	42
1.4.1 Precipitation Events: Description and Synoptic Overview.....	42
1.4.2 Surface Winds	43
1.5 ATMOSPHERIC AND SURFACE CONDITIONS OF THE CASE STUDIES	45
1.5.1 Atmospheric and Surface Conditions of the Reference Case	45
1.5.2 Atmospheric and Surface Conditions of the Event #1	46
1.5.3 Atmospheric and Surface Conditions of the Event #8	48
1.5.4 Atmospheric and Surface Conditions of the Event #13	50
1.6 HORIZONTAL FINE-SCALE FLOW-FIELDS OF THE CASE STUDIES	52
1.6.1 Fine-Scale Horizontal Flow-Fields of the Reference Case	52

1.6.2	Fine-Scale Horizontal Flow-Fields of the Event #1.....	54
1.6.3	Fine-Scale Horizontal Flow-Fields of the Event #8.....	55
1.6.4	Fine-Scale Horizontal Flow-Fields of the Event #13.....	56
1.7	VERTICAL FINE-SCALE FLOW-FIELD AND TURBULENCE OF THE CASE STUDIES.....	57
1.7.1	Vertical Fine-Scale Flow-Field and Turbulence of the Reference Case	58
1.7.2	Vertical Fine-Scale Flow-Field and Turbulence of the Event #1.....	60
1.7.3	Vertical Fine-Scale Flow-Field and Turbulence of the Event #8.....	63
1.7.4	Vertical Fine-Scale Flow-Field and Turbulence of the Event #13	66
1.7.5	RELATIVE CONTRIBUTION OF TURBULENCE SOURCES	69
1.8	DISCUSSION AND CONCLUSIONS	71
	ANNEXE A HYDROMETEOR TYPES DIAGNOSIS	75
	CONCLUSION	77
	RÉFÉRENCES	81

LISTE DES FIGURES

Figure 1.1 - Cartography of the studied domain. The terrain elevation is indicated by the color bar. The red line represents the continental divide and red dots are the observation sites Fortress Junction Station and Fortress Powerline Station. Red dashed line represents the Mount James Walker.	32
Figure 1.2 - a) Instruments setup and b) precipitation gauge located 30 m farther, adapted from Thériault et al. (2021). c) High-resolution topography of the Fortress Mountain region along with locations of FPS and FJS sites.	33
Figure 1.3 -Distribution of frequency occurrences (no units) encompassing both lidars Stare observations during the entire campaign for the determination of the Signal-to-Noise Ratio threshold value.	37
Figure 1.4 - Wind roses of occurrence of surface wind speeds and directions during the documented precipitation events at FPS (a) and FJS (b). and between the precipitation events at FPS (c) and FJS (d) measured by WXT520 (Thériault, et al., 2022).....	44
Figure 1.5 - Synoptic patterns during the case studies represented by the surface (MSL) pressure patterns (black lines) and upper level 500 hPa geopotential heights (red lines) computed by ERA5. a) event #1; b) event #2, c) event #3, d) reference case.	46
Figure 1.6 - Meteogram for on-site surface conditions during 3 days from 26 to 28 April 2019, including storm #1. Top three panels respectively represent surface atmospheric conditions as observed by the WXT520 (blue for FPS; red for FJS); a) station pressure (P); b) temperature (T) in solid lines and dew point temperature (T_d) in dotted lines; c) surface winds barbs. Bottom two panels show precipitation rates (pcpn rate) as measured by precipitation gauges and main hydrometeor types at the surface retrieved from disdrometers measurements (R: rain, G: graupels or snow pellets, WS: wet snow, DS: dry snow, black is unknown) at FPS (d) and at FJS (e). For all panels, sunrise and sunset are depicted by yellow and blue vertical lines respectively.....	47
Figure 1.7 - Meteogram for surface conditions during 3 days from 29 to 31 May 2019, including storm #8 and the reference day. Top three panels respectively represent surface atmospheric conditions as observed by the WXT520 (blue for FPS; red for FJS); a) pressure (P); b) temperature (T) in solid lines and dew point temperature (T_d) in dotted lines; c) surface winds barbs. Bottom two panels show precipitation rates (pcpn rate) as measured by precipitation gauges and main hydrometeor types at the surface retrieved from disdrometers measurements (R: rain, G: graupels or snow pellets, WS: wet snow, DS: dry snow, black is unknown) at FPS (d) and at FJS (e). For all panels, sunrise and sunset are depicted by yellow and blue vertical lines respectively.....	49
Figure 1.8 - Meteogram for surface conditions during 3 days from 19 to 21 June 2019, including storm #13. Top three panels respectively represent surface atmospheric conditions as observed by the WXT520 (blue for FPS; red for FJS); a) pressure (P); b) temperature (T) in solid lines and dew point temperature (T_d) in dotted lines; c) surface winds barbs. Bottom two panels show precipitation rates (pcpn rate) as measured by precipitation gauges and main hydrometeor types at the surface retrieved from disdrometers measurements (R: rain, G: graupels or snow pellets, WS: wet snow, DS: dry snow, black is unknown) at FPS (d) and at FJS (e). For all panels, sunrise and sunset are depicted by yellow and blue vertical lines respectively.	51

Figure 1.9 - Horizontal winds speed (colors) and direction (arrow) at FJS (a) and FPS (b) during the reference day, 29 May 2019, obtained by lidars VAD scan. Vertical shear of the horizontal wind (colors) at FJS (c) and FPS (d). Horizontal lines represent respectively from higher to lower altitudes, the Continental Divide (CD), Mount James Walker (MJW), FPS site and FJS site.....53

Figure 1.10 - Horizontal winds speed (colors) and direction (arrow) at FJS (a) and FPS (b) during the precipitation event #1, 27 April 2019, obtained by lidars VAD scan. Vertical shear of the horizontal wind (colors) at FJS (c) and FPS (d). Horizontal lines represent respectively from higher to lower altitudes, the Continental Divide (CD), Mount James Walker (MJW), FPS site and FJS site.....54

Figure 1.11 - Horizontal winds speed (colors) and direction (arrow) at FJS (a) and FPS (b) during the precipitation event #8, 30 May 2019, obtained by lidars VAD scan. Vertical shear of the horizontal wind (colors) at FJS (c) and FPS (d). Horizontal lines represent respectively from higher to lower altitudes, the Continental Divide (CD), Mount James Walker (MJW), FPS site and FJS site.....56

Figure 1.12 - Horizontal winds speed (colors) and direction (arrow) at FJS (a) and FPS (b) during the precipitation event #13, 21 June 2019, obtained by lidars VAD scan. Vertical shear of the horizontal wind (colors) at FJS (c) and FPS (d). Horizontal lines represent respectively from higher to lower altitudes, the Continental Divide (CD), Mount James Walker (MJW), FPS site and FJS site.....57

Figure 1.13 - Time-height section on the 29 May 2019 on the reference day from collected Doppler Lidar measurements at FJS (left) and FPS (right) sites. a-b) backscatter coefficient with higher (lower) values indicating more (less) reflectivity. Inverted triangles correspond to the cloud-base-height (CBH).; c-d) Vertical velocity with blue (red) indicating downward (upward) motions. Yellow dots indicate the planetary boundary layer (PBL) height.; e-f) Variance of the vertical velocity with larger (lower) values in red (blue).; g-h) Skewness of the vertical velocity with blue (red) indicating negative (positive) values. a-h) Grey solid horizontal lines represent FJS and FPS heights and black dotted lines illustrate Mount James Walker (MJW) and the continental divide (CD)'s heights. e-h) ML base (top) heights are given by the solid (dashed) lines.59

Figure 1.14 - Time-height section on the 27 April 2019 during the precipitation event #1 from collected Doppler Lidar measurements at FJS (left) and FPS (right) sites. a-b) backscatter coefficient with higher (lower) values indicating more (less) reflectivity. Inverted triangles correspond to the cloud-base-height (CBH).; c-d) Vertical velocity with blue (red) indicating downward (upward) motions. Yellow dots indicate the planetary boundary layer (PBL) height.; e-f) Variance of the vertical velocity with larger (lower) values in red (blue).; g-h) Skewness of the vertical velocity with blue (red) indicating negative (positive) values. a-h) Grey solid horizontal lines represent FJS and FPS heights and black dotted lines illustrate Mount James Walker (MJW) and the continental divide (CD)'s heights. e-h) ML base (top) heights are given by the solid (dashed) lines.61

Figure 1.15 - Time-height section on the 30 May 2019 during the precipitation event #8 from collected Doppler Lidar measurements at FJS (left) and FPS (right) sites. a-b) backscatter coefficient with higher (lower) values indicating more (less) reflectivity. Inverted triangles correspond to the cloud-base-height (CBH).; c-d) Vertical velocity with blue (red) indicating downward (upward) motions. Yellow dots indicate the planetary boundary layer (PBL) height.; e-f) Variance of the vertical velocity with larger (lower) values in red (blue).; g-h) Skewness of the vertical velocity with blue (red) indicating negative (positive) values. a-h) Grey solid horizontal lines represent FJS and FPS heights and black dotted lines illustrate Mount James Walker (MJW) and the continental divide (CD)'s heights. e-h) ML base (top) heights are given by the solid (dashed) lines.65

Figure 1.16 - Time-height section on the 21 June 2019 during the precipitation event #13 from collected Doppler Lidar measurements at FJS (left) and FPS (right) sites. a-b) backscatter coefficient with higher (lower) values indicating more (less) reflectivity. Inverted triangles correspond to the cloud-base-height (CBH).; c-d) Vertical velocity with blue (red) indicating downward (upward) motions. Yellow dots indicate the planetary boundary layer (PBL) height.; e-f) Variance of the vertical velocity with larger (lower) values in red (blue).; g-h) Skewness of the vertical velocity with blue (red) indicating negative (positive) values. a-h) Grey solid horizontal lines represent FJS and FPS heights and black dotted lines illustrate Mount James Walker (MJW) and the continental divide (CD)'s heights. e-h) ML base (top) heights are given by the solid (dashed) lines. Vertical axes are of reduced extent in comparison to figures 13-15 to better suit the data.....68

Figure 1.17 - Statistic of the relative contributions of turbulences sources at both sites as retrieved from lidars data. a) Mixing induced by under the air parcel (combination of surface warming and shear). b) Mixing induced by above the air parcel due to cooling. On both panels, horizontal grey lines represent the altitude of both lidar's sites FJS and FPS and green dotted lines identify the altitude of MJW and the CD.....70

LISTE DES TABLEAUX

Table 1.1- Instrumental specifications of StreamLine ^{XR} Doppler Lidar, Halo Photonics Ltd.....	34
Table 1.2 - Documented precipitation events of SPADE field campaign. Accumulated precipitation (pnpn acc) at FPS and at the main hydrometeor types at both sites. R = Rain; WS = wet snow; G = snow pellets; DS = dry snow.	36
Table 1.3 - Empirical relationships used for identification of hydrometeor types using equation 7 from diameter [mm] and fall speed [m s^{-1}].	75

LISTE DES ABRÉVIATIONS, DES SIGLES ET DES ACRONYMES

AB	Alberta
ACC	Accumulation
ACL	Adiabatic Condensation Level
AGL	Above Ground Level
AMSL	Above mean Sea Level
BC	British-Columbia
CAD	Canadian dollars
CBH	Cloud Base Height
CD	Continental Divide
DS	Dry snow
FJS	Fortress Junction Station
FPS	Fortress Powerline Station
G	Graupel or Snow Pellet
IP	Ice Pellet
Lidar	Light Detection and Ranging
LOS	Line-of-sight
MDT	Mountain Date Time
MJW	Mount James Walker
ML	Mixing Layer
MSL	Mean Sea Level
NCA	Niveau de condensation adiabatique
PBH	Planetary Boundary layer's Height
PBL	Planetary Boundary Layer
Pcpn	Precipitation
PPI	Plan Position Indicator
PWE	Precipitation Water Equivalent
R	Rain
Radar	Radio Detection and Ranging
RHI	Range Height Indicator
SNR	Signal-to-Noise Ratio

SPADE Storms and Precipitation Across the Continental Divide Experiment

UTC Universal Date Time

VAD Vertical Azimuth Display

VWS Vertical Wind Shear

WS Wet snow

LISTE DES SYMBOLES ET DES UNITÉS

Français (*anglais*) variable [unités]

Accumulation de précipitation (*precipitation accumulation*) [mm]

Altitude (*altitude*) z [m]

Asymétrie de la vitesse verticale (*skewness of the vertical velocity*) σ^3_w [$m^2 s^{-2}$]

Azimut (*Azimuth*) θ [$^\circ$]

Cisaillement vertical du vent horizontal (*bulk vertical shear of the horizontal wind*) VWS [s^{-1}]

Diamètre effectif des particules (*particle's effective diameter*) D [mm]

Élévation (*elevation*) ϕ [$^\circ$]

Longueur d'onde (*wavelength*) [μm]

Pression (*pressure*) P [hPa]

Taux d'accumulation de précipitation (*accumulation precipitation*) [mm h^{-1}]

Température (*temperature*) [$^\circ C$]

Vitesse terminale de chute des particules (*particle's terminal fall speed*) v_T [$m s^{-1}$]

Variance de la vitesse verticale (*variance of the vertical velocity*) σ^2_w [$m^2 s^{-2}$]

Vitesse horizontale du vent (*horizontal wind speed*) u (ou u et v) [$m s^{-1}$]

Vitesse verticale (*vertical velocity*) w [$m s^{-1}$]

RÉSUMÉ

En Terrain complexe, l'orographie perturbe l'écoulement atmosphérique à toutes les échelles, ce qui affecte les interactions des particules qui précipitent dans l'atmosphère. Ces interactions ont des répercussions sur les conditions météorologiques à la surface et en altitude. À grande-échelle, le soulèvement dynamique est le processus principale responsable des précipitations orographiques. À des petites échelles, ces interactions sont attribuables à une multitude de processus, tels que le mécanisme de renforcement de la formation des précipitations (*seeder-feeder mechanism* en anglais), les changements de phases et la déposition préférentielle. Les caractéristiques et les types des hydrométéores reçus à la surface sont le résultat des conditions atmosphériques dans lesquelles ils se forment et précipitent, dû aux interactions entre ces particules et l'environnement. Cette étude vise à caractériser l'écoulement de fine-échelle associé à des événements de précipitations survenus dans le sud-est des Rocheuses canadiennes au printemps 2019. Des observations ont été collectées par des instruments de surface in-situ et de télédétection lors de la campagne de terrain de SPADE-2019. Les mesures ont été effectuées à deux différentes altitudes le long de la montagne Fortress en Alberta: Au pied de la montagne dans la vallée de Kananaskis (1591 m) et sur plus haut sur la montagne Fortress (2076 m), nommées *Fortress Junction Station* (FJS) et *Fortress Powerline Station* (FPS). Des stations automatiques ont mesuré les conditions météorologiques à la surface et des disdromètres optiques étaient déployés pour caractériser les types d'hydrométéores à la surface. Des lidars Doppler ont mesuré avec haute-précision l'écoulement en trois dimensions de l'atmosphère au-dessus de chaque site, ainsi que la composition de la couche limite atmosphérique (CLA) et les couches de nuages et de précipitation. Ceci a permis d'investiguer l'écoulement de fine échelle comprenant les vents en trois dimensions ainsi que l'intensité et l'origine de la turbulence lors des 13 événements de précipitation de la campagne *Storms and Precipitation Across the Continental Divide Experiment* (SPADE) en 2019. Une étude de cas plus approfondie de trois de ces événements, en comparaison avec un cas de référence de ciel-clair fait l'objet de cette étude. Les vents de bas niveaux, l'intensité et les sources de turbulence incluant le cisaillement du vent, le contenu en aérosols, la structure de la CLA, la hauteur des couches nuageuses et de précipitations en altitude ainsi que les types d'hydrométéores à la surface sont étudiés et reliés entre eux. Les résultats montrent une plus grande variabilité dans l'écoulement et plus de turbulence à FPS qu'à FJS lors des événements de précipitation. En comparaison avec la journée de ciel-clair où le réchauffement solaire domine la turbulence, les processus menant turbulence associée aux précipitations sont divers et incluent notamment les refroidissements en altitude, les chauffages près de la surface et le cisaillement du vent. La turbulence est aussi plus importante à des altitudes inférieures à la division continentale qu'au-dessus où l'écoulement synoptique est plus uniforme. La CLA est également plus profonde à FPS qu'à FJS. Aussi, les hydrométéores collectés à FPS sont plus solides et mixtes qu'à FJS où il sont plus mixtes et liquides. Cette étude contribue à améliorer notre compréhension des interactions entre l'écoulement de fine-échelle et les précipitations dans les Rocheuses canadiennes pour mieux se préparer aux événements de précipitation.

Mots clés : Terrain complexe, couche limite planétaire, vent, Lidar Doppler, turbulence, précipitation, disdromètre optique, convection, cisaillement du vent, Rocheuses canadiennes, météorologie

ABSTRACT

In complex terrain, the orography disturbs the atmospheric flow-field at all scales, affecting its interactions with the precipitating particles. This impacts the meteorological conditions at the surface and aloft. At large-scales, orographic precipitations are driven by dynamical lifting. At small-scales, the interactions include various thermodynamic processes such as seeder-feeder mechanism cloud formation, phase changes and preferential deposition. Hydrometeor types at the surface result from the atmospheric conditions within which they form and precipitate. This study aims to characterize the fine-scale flow-field during precipitation events. In-situ and remote sensing observations were collected at two different elevations in the southeastern Canadian Rockies Alberta, during SPADE-2019 field-campaign: Fortress Junction Station (FJS) in the valley (1591 m AMSL) and Fortress Powerline Station (FPS) on the mountain (2076 m AMSL). Automatic weather stations measured surface meteorological conditions and optical disdrometers were deployed to characterize hydrometeor types. Doppler lidars measure atmospheric motions with a high precision and were deployed to measure 3D wind fields, the planetary boundary layer (PBL) properties and clouds and precipitation layers. This serves to characterize the fine-scale flow-fields, turbulence intensity and its causes. 13 precipitation events were documented during the SPADE field campaign and are presented in this paper. Three of them are investigated in-depth from synoptic to fine scale. These three case studies are compared with a clear-sky reference day. Data reveals more wind variability and turbulence at FPS with thicker PBL and more solid hydrometeor than FJS. Overall, this study contributes to improving the understanding of fine-scale flow-field and turbulence in the Canadian Rockies to better predict precipitation events.

Keywords: Complex terrain, Flow-field, Planetary boundary layer, Winds, Doppler Lidar, Turbulence, Precipitation, Optical Disdrometer, Convection, Wind Shear, Mixing layer, Canadian Rockies, meteorology.

SIGNIFICANCE STATEMENT

Fine-scale wind fields in mountainous regions are affected by the orography and impacts the onset of precipitation and cloud formation. In remote areas where observations are sparse, Lidar can provide cloud and precipitation layer characteristics, winds-field behaviour, turbulence intensity and origins along with the presence of low-level jets. They are key elements in aviation safety and in our understanding and further modelling of fine-scale processes. This study focuses on the processes associated with fine-scale flow-fields and turbulence during precipitation events near Fortress Mountain, Alberta. Doppler lidars installed at two elevations were used to measure winds and precipitation from the mountain to the valley, associated with precipitation events. The presence of clouds and precipitation strongly affects the diurnal PBL cycle of turbulence decreasing the instability due to solar heating. Evaporative cooling also generates instability and turbulence during precipitation events, which are crucial mechanisms that need to be accurately characterized to improve predictions of precipitation and severe weather.

INTRODUCTION

En terrain complexe, l'orographie perturbe l'écoulement atmosphérique à toutes les échelles, ce qui affecte l'interaction entre l'écoulement de l'air et les particules qui s'y forment et y précipitent. Ceci a des répercussions sur les conditions météorologiques en altitude et à la surface, telle que les quantités et types de précipitation reçue ainsi que la direction et la vitesse des vents et des rafales.

Les grandes échelles, typiquement de l'ordre de 1 à 100 km, vont de l'échelle d'une chaîne de montagne à l'échelle synoptique. À ces échelles, les précipitations sont principalement dues au soulèvement orographique des masses d'air à la rencontre de l'obstacle. Précisément, lorsque la masse d'air est bloquée par la présence d'une chaîne de montagne, elle est forcée de monter dynamiquement. Lors de l'ascension, elle subit un refroidissement adiabatique en raison de la diminution de la température avec l'altitude. Lorsque ce refroidissement est suffisant pour atteindre la saturation en altitude, il y a formation de nuage et possiblement de précipitations dites orographiques.

En ce qui concerne les fines échelles, allant de quelques dizaines de mètres à l'ordre du kilomètre, elles correspondent aux échelles d'une montagne entière à une pente de montagne. Les interactions entre les écoulements atmosphériques et les précipitations à fine-échelle comprennent une grande variété de processus thermodynamiques. On y retrouve notamment les changements de phases, la circulation de méso-échelle induite par la fonte, la formation de nuage et de précipitations de type *seeder-feeder* et la déposition préférentielles. Ces interactions affectent conjointement l'écoulement de fine-échelle, les types et quantités de précipitations reçues à la surface ainsi que les conditions atmosphériques à la surface et en altitude.

Dans le passé, l'importance de la collaboration entre les différentes branches de recherches sur les précipitations hivernales a été soulevées, notamment en incluant les tempêtes affectées par l'orographie (Stewart, et al., 1995). Des études récentes ont démontré que les conditions atmosphériques à fine-échelle doivent être considérées dans l'étude des événements de précipitation de grande-échelle, particulièrement en terrain montagneux où la complexité de la topographie engendre des phénomènes de micro et méso-échelles (Poirier, Thériault, & Leriche, 2019). Par exemple, dans les systèmes dépressionnaires comprenant des précipitations solides, liquides et mixtes, les processus à fine-échelle de changements de phases amènent la dépression à se creuser davantage. Ce phénomène de circulation

secondaire induite, mieux connue sous le terme anglophone de *melting-induced circulation*, est un exemple parmi d'autres d'interactions entre les précipitations, les conditions atmosphériques et l'écoulement ambiant aux différentes échelles impliquées dans les événements de précipitation (Gonzalez, et al., 2019). Nous reviendrons plus en détails sur ce processus.

De grandes quantités de précipitations peuvent être perçues sur Sud-Est des Rocheuses Canadiennes lorsque s'y abattent des tempêtes hivernales et printanières, pouvant causer des inondations à la base des montagnes. De telles catastrophes ont des répercussions sur la population, notamment sur les infrastructures telles que les routes et immeubles, ainsi que sur l'industrie touristique. Ces tempêtes engendrent évidemment des coûts importants à la société. L'inondation de Calgary survenue à la fin du printemps 2013 est la deuxième catastrophe naturelle la plus couteuse au pays après les incendies de Fort McMurray, avec une facture s'élevant à plus de 6 milliards de dollars (CAD), selon Milrad, Gyakum & Atallah (2015) et Pomeroy, Marks & Fang (2016).

Considérant la nécessité d'accroître notre compréhension de l'écoulement atmosphérique associé à des événements de précipitations en régions montagneuses, et considérant l'importance des événements de précipitation dans le Sud-Est des Rocheuses Canadienne, cette étude vise à caractériser de tels écoulements survenus lors d'événements de précipitations dans cette région. Plus particulièrement, cette recherche s'inscrit dans le projet *Storms and Precipitation Across the Continental Divide Experiment* (SPADE) dans le cadre duquel une campagne de terrain s'est déroulée dans le Sud-Est des Rocheuses Canadiennes en 2019, telles que détaillée dans Thériault et al. (2021) et (2022). Des données d'observations y ont été récoltées sur la montagne Fortress et dans la vallée de Kananaskis en Alberta. L'objectif est d'utiliser ce jeu de données pour évaluer l'influence de la topographie, en terrain complexe, sur l'écoulement atmosphérique de fine-échelle, notamment les mouvements verticaux dans la couche limite planétaire associé à la formation et la précipitation de types variés d'hydrométéores.

À notre connaissance, peu d'études ont à ce jour investiguer conjointement les écoulements de fine-échelle et les caractéristiques des précipitations, particulièrement en utilisant des données d'observations (Kim et al., 2021; Houze Jr 2012). Nous savons que certains projets d'observations sur l'écoulement à fine-échelles en terrain montagneux se sont tenus dans les Alpes Européennes (Steiner, Bousquet, Houze Jr, Smull & Mancini, 2003; Gerber, Mott & Lehning, 2019; Gonzalez et al., 2019; Raderschall, Lehning, & Schär, 2008) et aux États-Unis d'Amérique (Bossert, Sheaffer & Reiter, 1989; Henn et al., 2018).

Plusieurs de ces études ont utiliser des données modélisées. Premièrement, Gerber, Mott, & Lehning (2019) ont modéliser les interactions entre les précipitations et l'écoulement atmosphérique sur trois chaînes de montagnes Davos, Suisse, lors de deux évènements de précipitation. Ils ont soulevé l'importance des interactions entre les précipitations et l'écoulement en terrain complexe et démontré que ces interactions sont dépendantes des conditions atmosphériques de températures et d'humidité. Leurs résultats indiquent aussi que des conditions de faible stabilité sont nécessaires à la formation de grésil. Deuxièmement, Henn et al. (2018) ont également utilisé des modèles pour démontrer que les champs de courants atmosphériques doivent être considérés pour bien reproduire la distribution des précipitations dans les Sierra Nevada, Californie (États-Unis) afin d'améliorer la représentation de la précipitation orographique. Finalement, Raderschall, Lehning, & Schär (2008) ont simuler une tempête d'une durée de 120h sur une crête alpine apique pour investiguer la déposition préférentielle des hydrométéores interagissant avec l'écoulement atmosphérique.

D'autres études ont plutôt utilisé des données d'observations. Premièrement, Steiner, Bousquet, Houze Jr, Smull & Mancini (2003) ont étudier des évènements de pluie en automne 1999 sur le côté méditerranéen des Alpes à l'aide d'un radar Doppler pour mieux comprendre les interactions entre la pluie et l'écoulement d'une vallée situé dans une barrière topographique. Ils ont démontré que la subsidence causée par le refroidissement évaporatif des gouttes de pluie et de fonte des particules solide lors de la formation des gouttes de pluie contribue à la formation d'un écoulement descendant la vallée. Deuxièmement, Gonzalez, et al. (2019) ont utilisé un radar à bande-K, conjointement à un disdromètre optique pour étudier le lien entre les processus microphysiques des précipitations et les courant induits par les montagnes, plus particulièrement les ondes de montagne. Ils ont analysé un seul évènement de deux jours dans l'est des Pyrénées (Espagne) mais n'ont cependant pas trouvé d'évidence que les ondes de montagnes et la turbulence de bas niveaux influencent le givrage ou l'agrégation des particules en altitude, ni la distribution de taille et de vitesse de chute des hydrométéores à la surface. Finalement, Bossert, Sheaffer & Reiter (1989) ont étudié la circulation de méso-échelle lors de quatre étés entre 1984 et 1987, à 19 sites en terrain montagneux dans les Rocheuses États-Uniennes. Ils ont porté une attention particulière à l'oscillation diurne des vents et ont démontré que la convection diurne estivale menant à des averses a un fort influence sur les patrons de circulation à petite-échelle. Ils ont démontré que les courants turbulents dus à convection d'origine thermique sont plus observés principalement lorsque les

forçages par les systèmes synoptiques sont faibles. Ils ont aussi observé des processus de refroidissement en présence de nuage.

En sol Canadiens, des études d'écoulement de fine-échelles ont eu lieu dans la région de Toronto (ON), d'Iqaluit (NU) ainsi qu'en terrain montagneux à Whitehorse (YK) et à Squamish (BC) (Mariani, Stanton, Whiteway, & Lehtinen, 2020). Ces études ayant pour but de comparer les données d'observations aux modèles de prévision numérique du temps ont souligné les difficultés des modèles à résoudre les vents en terrain montagneux. Cela justifie la pertinence des données d'observations des vents de fine-échelle en terrain montagneux. Cependant, ces études ne focussent pas sur les événements de précipitations et il n'y a pas de publications concernant les lidars déployés en régions de montagneuses de Squamish et Whitehorse.

La portion Sud des Rocheuses Canadiennes, situé sur la frontière entre l'Alberta et la Colombie-Britannique, sépare les bassins versants de l'océan Pacifique (rivière du Columbia) et de la Baie d'Hudson (la rivière Nelson) (Ressource Naturelles Canada, 2022). Cette chaîne de montagne est composée de plusieurs sommets, dont le plus haut est le Mont Robson à 3954 m d'altitude. Ainsi l'apport d'humidité dans cette région provient de diverses sources, en fonction de la circulation atmosphérique à grande échelle. En effet, les précipitations qui atteignent cette limite de partage des eaux continentales dans le sud-est des Rocheuses canadiennes peuvent provenir du Pacifique, de l'Arctique ou encore du golfe du Mexique (Stoelinga, et al., 2003) et sont réparties de façon hétérogène au la région.

Lorsque la circulation atmosphérique qui provient de l'ouest ou du nord-ouest, la majeure partie de l'humidité transportée est souvent perdue sur le côté ouest de la chaîne de montagne sous forme de précipitations orographiques avant de rejoindre le côté est des Rocheuses. Il arrive également que l'humidité originaire de l'océan Pacifique entre sur le continent et traverse les montagnes Rocheuses. D'avantage d'humidité en provenance du Golfe du Mexique peut être advecté vers les Rocheuses Canadiennes. Lorsqu'une masse d'air atteint le Sud-Est des Rocheuses canadiennes avec une grande quantité d'humidité, d'importantes précipitations peuvent s'y accumuler. Tel que mentionné précédemment, de telles tempêtes peuvent avoir de graves répercussions gravement sur la population. Finalement, lorsque de l'air est advecté de l'Arctique, ce dernier étant froid et sec, il ne génère pas de forte précipitation.

La cause principale des tempêtes hivernales au Canada est les cyclones extratropicaux puisqu'ils transportent beaucoup d'humidité et de chaleur (Stewart, et al., 1995). Plus précisément, la circulation autour du centre de basse-pression cause l'advection d'humidité et des bandes de précipitations. Les bandes de fortes intensités de précipitation se produisent souvent près des centres dépressionnaires ou encore près du front chaud où l'atmosphère est instable. Au passage de telle bandes, de larges hydrométéores de neige mouillée peuvent être observés près de la surface causant une importante accumulation d'eau au sol (Reuter & Yau, 1990). Il se peut aussi que lorsqu'un système dépressionnaire traverse au-dessus d'une chaîne de montagne, il génère une atmosphère stable et de forts vents descendants sur le côté sous le vent (*leeward side* en anglais) de la montagne (Lilly, 1978).

Les types de précipitation reçue à la surface et les conditions dans lesquelles elles sont accumulées est de grande importance dans l'évaluation des risques qui y sont associés. Par exemple, l'inondation de Calgary en 2013 veut son ampleur au fait que de la pluie aient précipité sur de la neige, ce qui a accéléré la fonte de cette dernière et accru la quantité d'eau s'écoulant en piedmont (Pomeroy, Marks, & Fang, 2016). Généralement, lors des tempêtes hivernales canadiennes, les types de précipitations observés sont généralement la neige sèche, la neige mouillée (ou givrée, *rimmed* en anglais), le grésil (*ice pellets* en anglais), la pluie, la pluie verglaçante ou quelconque mélange de ceux-ci (Stewart, et al., 1995). Plus spécifiquement, pendant la saison froide, les patrons météorologiques synoptiques apportant la précipitation sur le côté Est des Rocheuses canadiennes, génèrent des précipitations en phases mixtes (Almonte & Stewart, 2019). De plus, la fraction liquide des hydrométéores atteignant la surface diminue avec l'altitude qui augmente (Thériault, et al., 2021). Dans un même système, là où les différentes phases de précipitations coexistent se nomme la région de transition pluie/neige. Le passage de cette région en un endroit donné correspond souvent à la période d'intensité maximale de précipitation du système, selon Stewart & Yiu (1993) et Stewart et al., (1995).

Il est connu que le type et la phase des hydrométéores qui atteignent la surface n'est pas que fonction de la température au sol, et ce d'autant plus en terrain montagneux. Au printemps 2015, lors d'une campagne de terrain précédente dans la même région, des particules de glace ont été observées à des températures de surface aussi élevées que 9°C dans des conditions de surface sous-saturées (Thériault, Hung, Vaquer, Stewart, & Pomeroy, 2018). Il existe abaissement de la région de transition pluie/neige sur le côté sous le vent (*windward side*, en anglais) d'une montagne, causé par le refroidissement diabatique latent de la fonte des particules solides ainsi que par le refroidissement adiabatique du soulèvement de l'air (Minder,

Durran, & and Roe, 2011). Enfin, il a été démontré que ces processus thermodynamiques affectent les vents en région montagneuses ainsi que l'évolution et la distribution des quantités et types de précipitations (Poirier, Thériault, & Leriche, 2019).

En terrain montagneux, le réchauffement non-uniforme du sol par le soleil ainsi que les vents de vallée affectent les profiles verticaux de températures, d'humidité et de vents. Ceci engendre des variations sur les conditions atmosphériques à la surface et au-dessus de celle-ci, pouvant se traduire par divers types de précipitations observées au sol (Thériault, Stewart, Milbrandt, & Yau, 2006). Effectivement, on définit le type d'un hydrométéore en fonction de ses caractéristiques, qui dépendent des conditions atmosphériques dans lesquelles la particule s'est formée et développées lors de sa chute du nuage jusqu'au sol.

L'interaction entre les hydrométéores et leur environnement est telle que les conditions de l'atmosphère sont affectées en retour par les processus thermodynamiques impliqués par la formation et l'évolution des particules. Particulièrement, tout changement de phase fait intervenir la chaleur latente conduisant à une modification de la température ambiante. Cette variation thermique affecte les hydrométéores, et ainsi suite, dans une boucle de rétroaction. Par exemple, la croissance d'un noyau glaçogène en flocon avec l'eau surfondue environnante crée un relâchement de chaleur latente de solidification, ce qui a pour effet d'augmenter la température ambiante. Le gradient thermique alors généré modifie les vents de fine-échelle par la création de courant ascendants et horizontaux. De l'instabilité naît également de ce réchauffement à fine-échelle par la force de flottabilité créée. Cette instabilité créée un brassage d'air turbulent. Dans le même ordre d'idée, des particules précipitant dans une couche sous-saturée, entraînent l'absorption de chaleur latente par évaporation (solide et/ou liquide), affectant les conditions ambiantes de température, d'humidité et de vents.

Introduit précédemment, le phénomène de circulation secondaire induite (*melting-induced circulation*) amène une dépression à se creuser davantage à cause du gradient horizontal diabatique engendré par le dégagement de la chaleur latente de changement de phase à fines-échelles. Une circulation secondaire de méso-échelle est induite avec des mouvements ascendants (descendants) de part et d'autre de la région de transition pluie-neige (Stewart & Donaldson, 1989). Ces modifications des conditions atmosphériques affectent les conditions de formation des hydrométéores, et conséquemment, divers types d'hydrométéores sont formés. Du côté froid (chaud) de la région de transition, la production de

précipitations solides (liquides) est favorisée en raison d'un refroidissement (réchauffement) adiabatique dans le courant ascendant (descendant).

Les patrons de dépositions de la précipitation au sol dépendent des interactions entre les hydrométéores qui précipitent et l'écoulement qui les entoure (Lehning, Löwe, Ryser, & Raderschall, 2008). Ceci est d'autant plus vrai pour les particules de neige sèche, en opposition aux gouttes de pluie, considérant que les caractéristiques physiques des hydrométéores influencent leurs portances et leurs frictions dans l'air (Thériault, Rasmussen, Ikeda, & Landolt, 2012). Par exemple, des flocons secs plus grands et légers suivront plus facilement les lignes de courant du vent que des particules denses et givrées ou mouillées. Conséquemment, les irrégularités dans l'écoulement amènent à de la turbulence dynamique and influence directement la dynamique du couvert neigeux. Ceci va sans dire que la dynamique du manteau neigeux en terrain montagneux est d'une grande importance pour les communautés en piedmont, puisque l'eau emmagasinées sous forme de neige dans les montagnes constitue à la fois une source primaire d'eau fraîche et un potentiel risque d'inondation (Hauer, et al., 1997).

La couche limite planétaire (CLA) est la portion de l'atmosphère qui est en contact avec la surface terrestre et directement influencée par celle-ci dynamiquement et thermiquement. D'abord, la CLA est dynamiquement influencée par la rugosité de la surface terrestre qui agit comme une condition frontière inertuelle à l'écoulement. Un fort gradient de vitesse des vents existe alors entre l'air en altitude, non contraint à ralentir, et l'air près de la surface, forcé de ralentir par la surface. Ce gradient génère un cisaillement du vent, qui engendre mélange turbulent de l'air par mouvements rotatifs des parcelles d'air, surtout près de la surface inertuelle. Dans les cas de CLA où la turbulence est uniquement dynamique, les tourbillons observés auront tendance à être plus aplatis et la couche de mélange sera moins profonde. Ainsi, l'énergie d'un écoulement moyen (laminaire, par exemple) est convertie à de la turbulence par cisaillement, et l'écoulement devient alors turbulent. Les diverses échelles météorologiques¹ spatiales ($L \sim$) et temporelles ($T \sim$) interagissent entre-elles, des grandes aux petites, par une multitude de processus, comme par exemple, la cascade d'énergie de Richardson qui transmet l'énergie dynamique de

¹ Les fines-échelles ($L \sim 1 - 10^4$ m, $T \sim 10^{-4} - 1$ h) sont caractérisées par un régime tridimensionnel non-hydrostatique où la force de Coriolis est négligeable, et incluent les échelles micro- ($L \sim 1$ m, $T \sim 1$ min) et méso- ($L \sim 10$ km, $T \sim 1$ h) où la turbulence et les processus convectifs sont dominants. Les grandes échelles ($L \sim 10^6 - 10^8$ m, $T \sim 1 - 10^3$ h) sont caractérisées par un régime bidimensionnel quasi-hydrostatique où la force de Coriolis domine, et incluent les échelles synoptique- ($L \sim 1000$ km, $T \sim 1$ jour) et planétaire- ($L \sim 10\,000$ km, $T \sim 1$ semaine) (Markowski & Richardson, 2011) via (Xue, 2015).

l'écoulement moyen de grande-échelle vers les échelles de plus en plus petites, jusqu'à l'échelle micro (Richardson, 1922).

Ensuite, la CLA est soumise aux variations diurnes solaires thermiques, et en absence de nuage, les radiations solaires réchauffent la surface terrestre durant le jour, qui se refroidit ensuite la nuit. Les nuages limitent la quantité de chaleur atteignant la surface terrestre en réfléchissant et diffusant l'énergie solaire, et ils absorbent la radiation terrestre limitant les refroidissements nocturnes. Donc, en présence de nuage, les gains et pertes de chaleurs sont amoindris et les variations de températures à la surface sont amorties. Les pertes de chaleur sont d'ailleurs d'autant plus limitées que les nuages sont froids et hauts. Le réchauffement solaire de la surface déstabilise thermiquement la couche limite, de façon que l'air près de la surface devenant plus chaud (donc moins dense) que l'air au-dessus de lui s'élève par des mouvements ascendants convectifs. C'est ce que qu'on appelle la turbulence due au chauffage de la surface, ou au chauffage par-dessous d'une parcelle d'air. En effet, un tel effet de réchauffement peut également se produire au sommet d'une couche nuageuse, ou un même phénomène d'instabilité convective est observé. Dans ce cas, on observera des courants ascendants forts et larges, compensés par des courants descendant faibles et étroits, ce qui se traduit mathématiquement par une asymétrie (*skewness* en anglais) positive de la vitesse verticale.

Tout comme la CLA peut être déstabilisée par un réchauffement de la surface, elle peut également l'être par un refroidissement en altitude. Ainsi, de l'air froid et dense se retrouve au-dessus d'air plus chaud et moins dense, et des mouvements de subsidence turbulents sont créés afin de rétablir un équilibre dans la CLA. Dans ce cas, on observera des courants descendant forts et larges, compensés par des courants ascendants faibles et étroits, ce qui se traduit mathématiquement par une asymétrie (*skewness* en anglais) négative de la vitesse verticale. Dans le cas d'une CLA turbulente convective, les tourbillons formant la couche de mélange seront bien développés sur la verticale, couvrant des tailles allant de l'échelle micro à la profondeur de la couche de mélange.

Des changements des conditions atmosphériques à la verticale ainsi que des mouvements verticaux de l'air sont engendrés par le mélange dans la couche limite planétaire. Les courants ascendants convectifs de l'air chaud de la basse CLA peut mener à la formation de nuage si l'air en ascension atteint le niveau de condensation adiabatique (NCA) (Berg, Newsom, & Turner, 2017). De plus, les profiles verticaux de températures et d'humidité dans la CLA dépendent du mélange turbulent, qui modifient uniformise les

conditions de températures et d'humidité dans la CLA. Donc, la turbulence modifie le taux de refroidissement de l'air avec l'altitude, et conséquemment peut modifier la hauteur du NCA. Les tourbillons turbulents jouent également un rôle clé dans la dynamique de l'atmosphère puisqu'ils transportent verticalement la chaleur, l'humidité et la quantité de mouvement de la surface vers le sommet de la couche de mélange, et qu'ils altèrent la quantité de mouvement de l'écoulement moyen de plus grande-échelle.

Dans cette étude, deux lidars Doppler sont utilisés pour mesurer les couches de précipitation et de nuages ainsi que les vitesses et directions des vents de la couche limite. En particulier, un lidar fut déployé dans la vallée de Kananaskis à 1591 m d'altitude et un second sur la montagne Fortress à 2076 m d'altitude. Ces lidars pointaient verticalement vers le haut (*Stare scans*) et effectuaient des balayages en cônes (*VAD scans*). Des algorithmes statistiques sont appliqués sur ces vents afin de quantifier l'intensité et l'origine de la turbulence. Précisément, la variance de la vitesse verticale permet de quantifier l'intensité de la turbulence et la présence de couche de mélange. L'asymétrie (*skewness* en anglais) est utilisée pour distinguer les cas de turbulence due au chauffage de la surface terrestre des cas de turbulence due au refroidissement en altitude. L'utilisation combinée de variance et d'asymétrie a fait ses preuves pour caractériser l'intensité et l'origine de la turbulence de la CLA en ciel clair et nuageux (Hogan, Grant, Illingworth, Pearson, & O'Connor, 2009).

On y distingue les cas de turbulence dynamique due au cisaillement des vents des cas d'instabilités thermiques initiées par un chauffage à la base d'une parcelle d'air ou encore par un refroidissement en altitude. D'autre part, les types de précipitations sont retrouvés à l'aide de disdromètres optiques déployés à ces deux mêmes sites. Finalement, des stations automatiques de surface aussi déployées aux deux stations sont utilisées pour y mesurer les conditions météorologiques.

En combinant les observations de ces instruments, il est possible de produire une analyse de l'écoulement atmosphérique de fine-échelle associé à des précipitations sans avoir d'observations humaines ou de lancement de radiosondage. Cela constitue un avantage considérable en région éloignée ou difficilement accessible. De plus, les lidars constituent une valeur ajoutée même là où les radiosondages sont possibles puisqu'ils fournissent des observations continues en altitude entre les lancements de ballons-sondes (Mariani, et al., 2018). Des études précédentes ont également caractérisé la CLA à l'aide de lidar Doppler, notamment, Hogan, Grant, Illingworth, Pearson & O'Connor (2009) ont évalué l'évolution diurne de la CLA

en distinguant les cas de turbulence de chauffage de surface de ceux de refroidissement en altitude. Ils n'ont cependant pas étudié les vents horizontaux ainsi que la turbulence de cisaillement.

Ce mémoire comprend un premier chapitre présenté sous forme d'article scientifique portant sur l'analyse des écoulements en lien avec les évènements de précipitation documentés dans le cadre du projet SPADE 2019. La section 1.1 réintroduit le sujet en anglais. La méthodologie sur le terrain ainsi que les algorithmes de traitement des données sont présentés dans la section 1.2 et 1.3 respectivement. Les résultats sont présentés dans les sections 1.4 à 1.7.

CHAPITRE 1

FINE-SCALE FLOW FIELD AND PRECIPITATION EVENTS IN THE CANADIAN ROCKIES USING DOPPLER LIDARS DURING SPADE-2019

Ce chapitre est présenté sous forme d'article scientifique. Il porte sur la caractérisation de l'écoulement de fine-échelle à partir d'observations de lidars déployés dans le sud-est de l'Alberta, Canada. Plus particulièrement, il s'agit de l'analyse des écoulements en lien avec les événements de précipitation documentés dans le cadre du projet SPADE 2019. Cet ouvrage présente d'abord une revue des connaissances sur les interactions entre les précipitations et l'écoulement, et ce, des grandes aux petites échelles. Ensuite, les objectifs de recherche sont présentés en perspectives des travaux existants sur le sujet. Une présentation détaillée de la méthodologie utilisée s'ensuit.

Les événements de précipitations sont ensuite présentés sommairement et trois d'entre eux font l'objet d'étude de cas, en comparaison avec une journée de ciel clair. Les patrons synoptiques sont d'abord détaillés afin de bien comprendre l'origine de l'humidité menant à la précipitation sur la région d'intérêt. Ensuite, les vents à la surface et en altitudes sont analysés et présentés, et leur analyse statistique est utilisée pour retrouver l'intensité et l'origine de la turbulence dans la couche limite planétaire. Finalement, les couches de nuages et de précipitations en altitude, ainsi que les types de précipitations collectées à la surface par des disdromètres optiques y sont également présentés afin de bien caractériser les interactions entre les particules et l'écoulement.

Ce chapitre est le fruit de travail de maîtrise effectué sous la supervision de la Professeure Julie M. Thériault et la co-supervision du chercheur Zen Mariani de la division de recherche du Centre Météorologique Canadien à Environnement et Changement Climatique Canada. Nicolas R. Leroux, stagiaire postdoctoral a également contribué à ce projet.

**Fine-Scale Flow Field and Precipitation Events in the Canadian Rockies Using Doppler Lidars
during SPADE-2019**

Aurélie Desroches-Lapointe,^a Zen Mariani,^b Julie M. Thériault,^a Nicolas R. Leroux,^a

^a Centre ESCER, Department of Earth and Atmospheric Sciences, *Université du Québec à Montréal,
Montreal, Quebec, Canada*

^b Meteorological Research Division, *Environment and Climate Change Canada, Toronto, Ontario, Canada*

Corresponding author: Aurélie Desroches-Lapointe (aurelie.desroches.lapointe@gmail.com)

1.1 INTRODUCTION

The mountain snowpack is of primary source of fresh water to downstream communities and is a key element in the assessment of natural hazards (Hauer, et al., 1997). The eastern side of the Canadian Rockies (fig. 1) is a region prone to extreme precipitation events that can have major consequences. When winter and spring storms travel over eastern side of the Canadian Rockies, high amounts of precipitation can be accumulated, sometimes resulting in major flooding events (Pomeroy, Marks, & Fang, 2016). These catastrophes are of major interest for many public domains such as transports and roads, tourism, and the recreational sector. According to The Candian Press (2023), the well-known Calgary flood that occurred during late spring in 2013 is among the three most expensive natural hazards in Canadian history, with costs exceeding CAD \$6 billions (Milrad, Gyakum, & Atallah, 2015; Pomeroy, Marks, & Fang, 2016). The precipitation types reaching the surface and the conditions in which they accumulate on the ground is of major importance in the assessment of natural hazards (Hauer, et al., 1997).

Over the southeastern Canadian Rockies, the most common pattern leading to winter storms is extra-tropical cyclones (Stewart, et al., 1995) with moist air from the Pacific further south or from the Gulf of Mexico can travel inland and produce high-impact precipitation events. The precipitation types are generally wet/rimed snow, dry snow, ice pellets, rain, freezing rain, or any mixture of these (Stewart et al. 1995). At lower elevations on the eastern side of the Canadian Rockies, during the cold season, synoptic weather patterns leading to precipitation often produce mixed precipitation (Almonte & Stewart 2019; Thériault et al., 2021). The importance of various aspects of winter storms including orographically affected storms have been highlighted (Stewart, et al., 1995). Recent studies have shown that fine-scale atmospheric conditions need to be considered to better study precipitation events, especially in mountainous regions where the complexity of the terrain lead to meso- and micro-scale phenomena (Poirier, Thériault, & Leriche, 2019).

Deposition patterns of the precipitation on the ground are driven by the interactions between the precipitating hydrometeors and the surrounding flow-field (Lehning, Löwe, Ryser, & Raderschall, 2008). Terrain irregularities encountered by wind-flow directly modifies this wind-flow inducing dynamical turbulence, and consequently influence the snow cover dynamics. This is also in relationship with the hydrometeor's characteristics and types, as it influences the likeliness of a particles to be transported by winds (Thériault, Rasmussen, Ikeda, & Landolt, 2012). In complex terrain, the orography disturbs the atmospheric flow-field from large-scale to fine-scale, affecting the interactions between the precipitation

and the surrounding flow-field. Gonzalez et al. (2019) mentioned the complex nature of the multi-scales' interactions involved in dynamical and microphysical processes of precipitation and circulation. These interactions simultaneously impact the fine-scale flow-field and the meteorological conditions at the surface and aloft. The valley flow and the orography induce non-uniform solar heating, that also affect vertical temperature, humidity and wind profiles. Resulting variations of the atmospheric conditions from surface to the clouds lead to various hydrometeor characteristics (Thériault, Stewart, Milbrandt, & Yau, 2006).

At small-scales, the interactions include various thermodynamic processes such as seeder-feeder cloud formation, phase changes, preferential deposition and snow redistribution. The processes of hydrometeors formation have a feedback effect on atmospheric conditions through phase change induced latent heat flux and water content modifications. Minder, Durran & Roe (2011) showed the lowering of the transition region on a mountain's windward slope as a result of endothermic phase change of solid-particles and adiabatic cooling of rising air. Furthermore, Poirier, Thériault & Leriche (2019) highlighted that these thermodynamic processes impact wind fields in mountainous regions along with the evolution and distribution of precipitation amounts and types.

Model-based studies investigated the interactions between precipitation and flow-field. Gerber, Mott & Lehning (2019) investigated these interactions and highlighted their importance in complex terrain and they demonstrated their dependence on atmospheric temperature and humidity. Furthermore, Henn et al. (2018) demonstrated the necessity to consider wind fields to accurately reproduce precipitation distribution to better represent the orographic induced precipitation. Finally, Raderschall, Lehning & Schär (2008) investigated and defined preferential deposition of hydrometeors interacting with the surrounding flow-field.

Observations-based studies of winds and precipitations have been conducted in complex terrain. Using a Doppler Radar, Steiner, Bousquet, Houze Jr, Smull & Mancini (2003) studied rain events during fall 1999 over the Mediterranean side of Alpes, and demonstrated that subsidence caused by evaporation and melting cooling contribute to the formation of a down-valley flow-field. Similar wind patterns have been observed in the Whistler Valley, British Columbia, Canada (Thériault, et al., 2012). Additionally, Bossert, Sheaffer & Reiter (1989) studied the summer meso-scale circulation in the American Rockies (United-States) and showed that diurnal convection can lead to precipitation, strongly impacting the meso-scale

circulation. They demonstrated that thermal induced turbulence was mainly observed when forcing by synoptic systems was weak and they observed cloud-cooling processes.

The planetary boundary layer (PBL), being the lowest part of the atmosphere, is directly influenced by the Earth's surface, thermically and dynamically (Stull, 1988). The PBL is composed of a surface layer, typically with a depth of 10 % of the PBL, where the wind gradient is maximal due to non-slip surface condition, and where the wind speed rapidly increases with height and the potential temperature decreases with height. Above the surface layer there is the turbulent mixing layer (ML) with generally uniform potential temperature and winds, due to the strong mixing turbulent eddies. On the top of the PBL is the entrainment zone, separating the PBL and the free atmosphere above. At night, the solar income stops reaching the Earth's surface and the surface layer, which cools and stabilizes, forming a temperature inversion called the nocturnal boundary layer. A residual layer of convection lingers above the stable nocturnal boundary layer, and is eventually mixed with air released from unstable the surface layer reformed the following day (Olofson, 2008).

Turbulence plays a key role in dynamic meteorology as they vertically transport heat, moisture, and momentum away from the surface, altering the large-scale flow. Convective uplift in the PBL potentially leads to cloud formation at the adiabatic condensation level (ACL) (Berg, Newsom, & Turner, 2017). PBL mixing modifies the vertical temperature and humidity profiles and vertical motions.

Both dynamical and thermal processes can drive the PBL turbulence. Moreover, the turbulent mixing of an air parcel can be induced by below or above it, depending on thermodynamic processes and atmospheric conditions. Surface warming caused by daily-solar-forcing leads to positive buoyancy and thermally unstable convective PBL with turbulence driven by below an air parcel. Solar warming may occur at the top of a cloud layer creating convective turbulence in altitude. Cooling aloft due to endothermic phase changes or clouds' radiative loss, can result in negative buoyancy and convective eddies. Strong winds in altitude, such as nocturnal low-level-jet, drive dynamical turbulence, and the air parcel located under that jet undergo turbulent mixing induced by above. In thermally induced turbulence, a deep mixing-layer (ML) is formed with turbulent eddies of large vertical extent, sometimes as high as the PBL itself. A more flattened ML is formed by dynamically induced turbulence. The turbulence induced from below (above) an air parcel results in strong and wide updrafts (downdrafts), compensated by narrow downdrafts (updrafts), mathematically expressed by positive (negative) skewness of the vertical velocity.

Finally, previous studies such as Hogan, Grant, Illingworth, Pearson & O'Connor (2009) characterized the PBL using Doppler lidars and investigated the diurnal evolution of the PBL by distinguishing situations of turbulence driven by surface-warming of those of turbulence driven by cooling aloft. However, they did not investigate horizontal winds and wind shear induced turbulence.

To our knowledge, only few studies have investigated both fine-scale flow-field and precipitation characteristics, especially in the framework of observational campaign (Kim et al., 2021; Houze, 2012). A few field projects on fine-scale flow field over mountainous terrain were held in the Swiss Alps (e.g., Steiner et al. 2002; Gerber et al., 2019; Gonzalez et al. 2019; Raderschall et al., 2008) and United-States (e.g., Bossert et al., 1989; Henn et al., 2018). In Canada, fine-scale flow-fields studies using Doppler lidars were held to compare observations with numerical weather prediction models (Mariani, Stanton, Whiteway, & Lehtinen, 2020) revealing difficulties of high-resolution models to resolve wind fields in mountainous terrain.

Giving the need to improve our understanding of precipitation formation and associated atmospheric flow-field in mountainous terrain, the goal of this study is to characterize the atmospheric flow field in the PBL observed during spring precipitation events in the southeastern Canadian Rockies. To do so, the measurements collected during the 2019 *Storms and Precipitation Across the Continental Divide Experiment* (SPADE) project are used. Two Doppler wind lidars were deployed to measure flow-field, cloud, and precipitation layers in the Kananaskis valley and on Fortress Mountain. The Lidars were collocated with optical disdrometers and automatic measurements of precipitation, horizontal winds and meteorological conditions at the surface. The combination of these automatic instruments is a considerable advantage for PBL observational studies of remote and hardly accessible regions where no radio-sounding are launched.

The paper is organized as follows. Section 1.2. describes the experiment setup and presents the documented precipitation events. Section 1.3 details the methodology such as statistical algorithms applied to lidar data to retrieve the turbulence intensities and origins, along with cloud and precipitation layers. The method used to diagnosticate hydrometeors type using optical disdrometers is also presented in this section. An overview of the campaign and surface winds presented in sections 1.4. Three selected storms are analysed in detailed in sections 1.5 to 1.7, where precipitation characteristics and fine-scale flow-fields are deeply analysed. Discussion and conclusion are in the section 1.8.

1.2 EXPERIMENTAL DESIGN

1.2.1 Overview of the Field Experiment

The SPADE campaign was held in the southern Canadian Rockies from the end of April to June 2019 (fig. 1). Three main stations were installed to measure meteorological conditions and precipitation across the continental divide at the surface and aloft. One station was deployed on the western side of the divide, at Nipika Mountain Resort, and two were deployed on the eastern side along Fortress Mountain. These two sites are Fortress Junction station (FJS) located in the Kananaskis valley bottom (1591 m) and Fortress Powerline station (FPS) higher on the mountain at 2076 m altitude AMSL. A detailed description of the data collected is given in Thériault et al. (2021). This paper focuses on the two sites of the eastern side of the Rockies (fig. 1, fig. 2c).

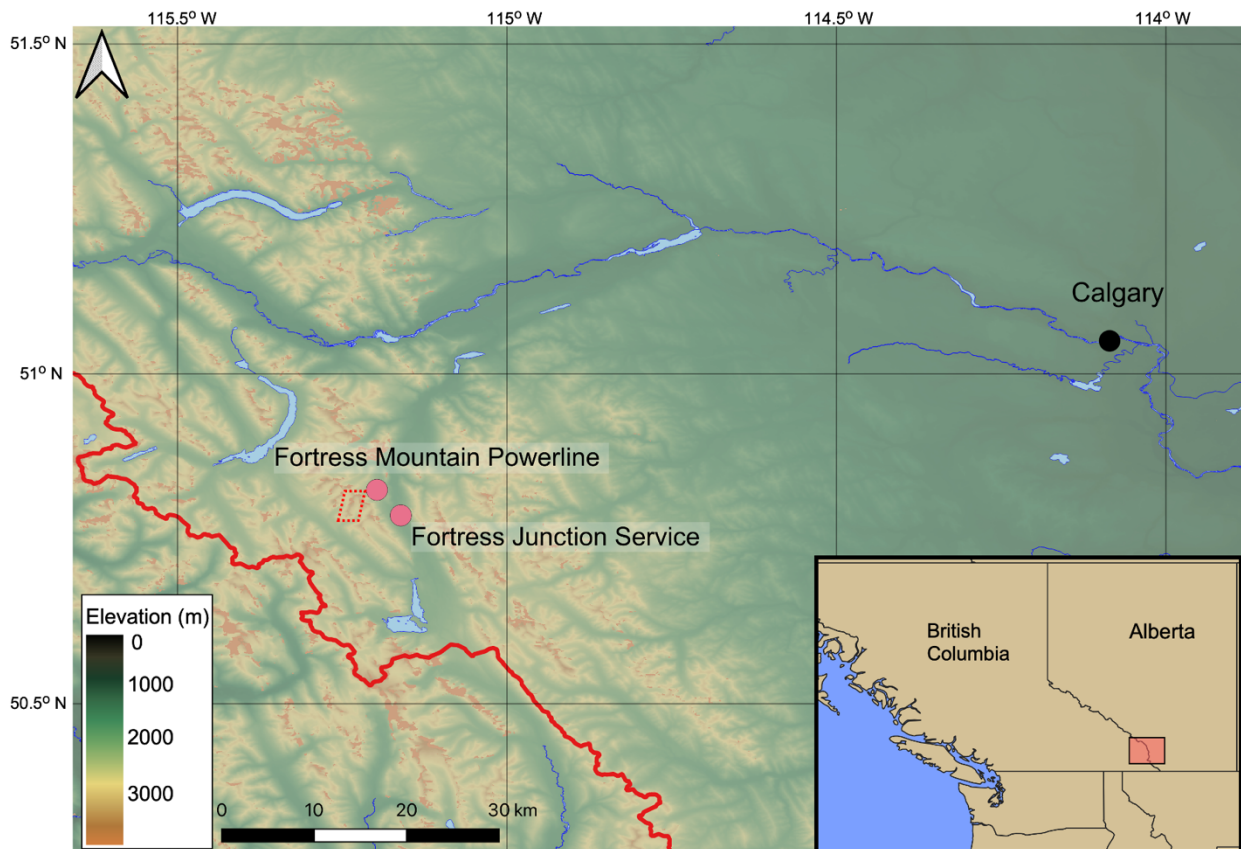


Figure 1.1 - Cartography of the studied domain. The terrain elevation is indicated by the color bar. The red line represents the continental divide and red dots are the observation sites Fortress Junction Station and Fortress Powerline Station. Red dashed line represents the Mount James Walker.

Both sites were equipped with a similar instrumental setup as depicted on figure 2a. The amount of precipitation at each site was measured using a weighing gauge installed in a single-Alter shield (fig. 2 b) located 30 m away from the main setup (fig. 2 a). The characteristics of the precipitation reaching the surface at each station, such as fall-speed and diameter, were measured with OTT Parsivel laser-optical disdrometers (fig. 2 a). This study focuses on the eastern side of the Canadian Rockies where wind lidars were deployed (fig. 2 a, c), allowing a deeper study of fine-scale flow fields. More specifically, in order to characterize the wind and turbulence fields in the Kananaskis valley and along Fortress Mountain, two identical StreamLine^{XR} Doppler wind lidars (Halo Photonics) were installed at FPS and FJS (fig. 2 a, c). They continuously conducted multiple scans to measure the fine-scale flow field above each site. In addition, surface meteorological conditions were measured by weather probes: air temperature, relative humidity, horizontal wind speed and direction. More information about the complete dataset collected during SPADE is given in Thériault et al. (2021).

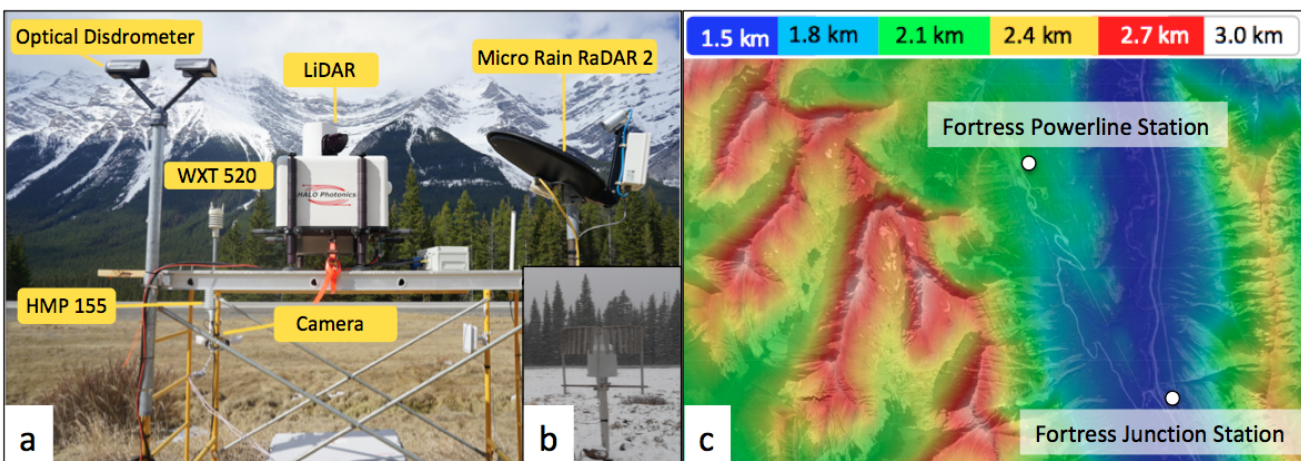


Figure 1.2 - a) Instruments setup and b) precipitation gauge located 30 m farther, adapted from Thériault et al. (2021). c) High-resolution topography of the Fortress Mountain region along with locations of FPS and FJS sites.

1.2.2 Instrumentation

The Doppler wind lidar is an active $1.5 \mu\text{m}$ heterodyne remote sensing instrument. Specifications are presented in Table 1. It is made to enable observations of the atmospheric flow field in clear sky circumstances (Pearson, Davies, & Collier, 2009). This is an added value in comparison with radars, that only enable measurements of clouds and precipitation and do not allow clear sky measurements. Lidars allow high-resolution measurements within the planetary boundary layer (PBL), from 60 m above-ground-

level (AGL) up to \sim 10 km. We note that this maximal measurement range is highly dependent on atmospheric content. These instruments have demonstrated their ability to conduct detailed observations of winds and cloud-precipitation layers in complex terrain, including observations of lake breezes, low-level jets, and stratified wind layers (Hogan, Grant, Illingworth, Pearson, & O'Connor, 2009; Manninen, Marke, Tuononen, & O'Connor, 2018; Mariani, et al., 2018; Newsom, Sivaraman, Shippert, & Riihimaki, 2019; Päschke, Leinweber, & Lehmann, 2015).

Table 1.1- Instrumental specifications of StreamLine^{XR} Doppler Lidar, Halo Photonics Ltd.

Wavelength	1.5 μm
Pulse repetition frequency	10 kHz
Number of range gates	3980
Radial effective resolution (along LOS)	3 m
Maximal range	9600 m
Velocity resolution	0.0382 m s^{-1}
Power	80 μJ

Every 10 min, the lidar was set to perform a 4-beams Velocity-Azimuth-Display (VAD) scan, at 80° elevation, to obtain a two-dimensional vertical wind profile (Browning & Wexler, 1968). This 58 s lasting VAD scan was followed by a Stare scan toward zenith, constituted of six consecutives beams over a 30 s period. Additional scans (PPI and RHI) were performed but not used in this study. For all scan types, raw outputs of the instruments contain backscatter coefficient (β), Doppler velocity (v_D) and signal-to-noise ratio (SNR), all discretized in 3980 range-gates along the line of sight (LOS) of every beam.

Backscatter (β) measurements serve to identify clouds, precipitation, and aerosol layers throughout their particle load and radiative properties. Atmospheric aerosols, cloud water droplets and precipitation particles act as different scatterers to the incident signal and hence can be distinguished. Aerosols act as a PBL tracer as they are small enough to follow the wind flow and are uniformly distributed due to mixing by turbulence. Doppler velocities (v_D) from Stare scans are used to characterize the vertical motion and turbulence characteristics. Doppler velocities (v_D) from VAD scans allow to retrieve the horizontal wind profile above the instrument, with an accuracy comparable to radiosondes, even in mountainous terrain (Mariani, Crawford, Casati, & Lemay, 2020). VAD scans Doppler velocities (v_D) are also used to retrieve the vertical wind shear (VWS) of the horizontal winds. WXT520 (Vaisala, 2012) surface weather transmitters provide surface wind measurements to cope for the lidar's blind zone from the surface to 60 m line-of-sight (LOS).

Precipitation characteristics were obtained using a laser-optical disdrometer OTT Parsivel (Battaglia, Rustemeier, Tokay, Blahak, & Simmer, 2010) installed on each site. Effective diameters (D) and fall-speeds (v_T) of falling particles were recorded in 32 discrete non-uniform bins, respectively, for sizes from 0.0 mm to 25.0 mm and velocity between 0 $m s^{-1}$ and 20.8 $m s^{-1}$. With a time-interval of 10 s, data are saved as a 1024 long precipitation spectrum. Each spectrum contains the number particles corresponding to each bin of the 32 X 32 size – fall speed coordinate. From these data, hydrometeor types can be determined of a chosen time interval (more details in section 1.3.5).

1.2.3 Precipitation Events

During the SPADE field campaign, 13 precipitation events were documented on the eastern side of the divide (Table 2). The definition of these precipitation events is primarily based on the precipitation gauge data indicating precipitation greater than 0.5 $mm h^{-1}$. Although short-term gaps in the data were accepted, extended period with no precipitation detected indicates starts and ends of these events. They are described in detail in Thériault et al., (2021) and (2022). The hydrometeor types were diagnosed by their fall speeds and diameters, following the method presented in (Ishizaka, et al., 2013) and based on the empirical relationships between particle types, fall speed and diameters (Rasmussen, Vivekanandan, Cole, Myers, & Masters, 1999). Details are presented in annexe A. In this study were classified in four categories: rain (R), snow pellets or graupel (G), wet snow (WS) and dry snow (DS).

When precipitation aloft were observed but did not reach the surface (virga), lidar data were used to identify precipitation or cloud layers aloft. Virga episodes are also documented using lidar data, which constitutes an added value compared to in-situ measurements. They were identified based on the vertical motion measurements, as falling virga particles contributes to downward motion in the lower part of the cloud. Moreover, surface weather conditions such as the humidity were considered, as virga occurred when precipitation falls into a drier lower atmosphere. In contrast, during intense precipitation, the lidar signal is attenuated due to absorption limiting the data availability, especially the maximal range measurable. To complement the dataset, pre- and post-precipitation event conditions were investigated.

Table 1.2 - Documented precipitation events of SPADE field campaign. Accumulated precipitation (pnpn acc) at FPS and at the main hydrometeor types at both sites. R = Rain; WS = wet snow; G = snow pellets; DS = dry snow.

Event #	Start – End (hhmm) [UTC] (date)	Pcpn acc at FPS [mm]	Main Hydrometeor Types at FPS	Main Hydrometeor Types at FJS
1	2250 UTC 26 April - 1100 UTC 28 April	32.5	WS + G	WS + G
2	1900 UTC 30 April - 0130 UTC 01 May	4.2	WS + DS	WS + DS
3	1700 UTC 04 May - 1120 UTC 05 May	15.3	WS	WS
4	1800 UTC 08 May - 0000 UTC 09 May	1.2	WS	R
5	0500 UTC 16 May - 2230 UTC 18 May	20.2	WS+R	R+WS
6	0445 UTC 24 May - 0600 UTC 25 May	8.5	R	R
7	1220 UTC 35 May - 0000 UTC 26 May	14.5	WS+R	R
8	1600 UTC 30 May - 2210 UTC 30 May	6.5	R	R
9	0100 UTC 07 June - 0530 UTC 08 June	21.4	WS+R	R
10	1010 UTC 14 June - 1040 UTC 14 June	1.3	R	R
11	2000 UTC 17 June - 2350 UTC 17 June	1.1	R	R
12	0830 UTC 19 June - 1940 UTC 20 June	12.6	WS+R	R
13	0330 UTC 21 June - 2340 UTC 21 June	56.0	WS+R	WS+R

1.3 DATA ANALYSIS

1.3.1 Quality Control

The primary quality control applied to the lidar dataset is using the Signal to Noise Ratio (SNR), ensuring the measured signal intensity to be significantly stronger than the noise of the instrument. The manufacturer of the StreamLine Doppler lidar suggests a SNR threshold values of 0.015 (-18.2 dB) to obtain a precision of the Doppler velocity better than 30 cm s^{-1} (Pearson, Davies, & Collier, 2009), a value qualified

as rather conservative in previous studies (Päschke, Leinweber, & Lehmann, 2015). The common approach of the SNR-based thresholding technique allows to determine a reasonable SNR threshold to ensure a quality control. Following the method presented in Päschke (2015), an optimal SNR threshold value of 0.003 (-25.2 dB) to filter our specific dataset was determined from the distribution of frequency occurrences (fig. 3). The data availability is increased by as much as 23 % by applying this new threshold in comparison to that obtained by applying the manufacturer's value. Moreover, as this study was conducted in a mountainous rural region where the aerosols concentration is generally lower in comparison with urban area as in Ackermann, et al (1998) and Blifford Jr & Ringer (1969), resulting in a decrease the backscattering of the lidar signal. This motivates even more the choice of a lower threshold to increase the dataset availability (Browning & Wexler, 1968). Finally, to fully ensure the quality of the dataset, raw data that was outside the scope of physically realistic values were discarded. Large discontinuities in data, in both radial and angular directions, along with improbably large velocity values ($> 28.5 \text{ m s}^{-1}$) were used to identify outliers.

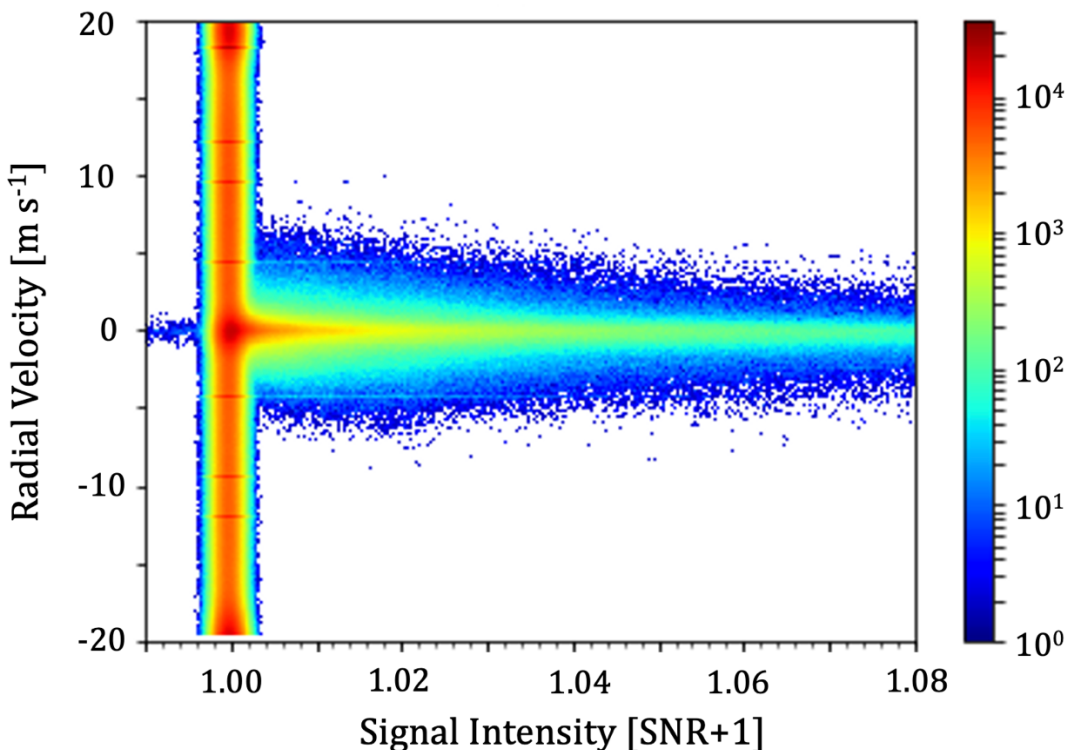


Figure 1.3 -Distribution of frequency occurrences (no units) encompassing both lidars Stare observations during the entire campaign for the determination of the Signal-to-Noise Ratio threshold value.

1.3.2 Wind Field Retrieval

Once the events were identified, the lidar data was used to characterize wind fields above each site, complemented by the surface weather transmitters (WXT520) for surface winds. The WXT520 supplies high temporal resolution (10 s) 2-m surface horizontal wind speed and direction with a velocity precision better than 0.05 m s^{-1} (Vaisala, 2012).

At heights of 60 m AGL and above, wind speed and directions are retrieved from lidar Doppler velocities (v_D), equivalent to radial velocities $\mathbf{v}_{r,i}$ in the LOS direction. Vertical winds are retrieved from Stare scan (zenith-viewing) data, with downward (upward) motions correspond to negative (positive) radial velocity as the air moves toward (away from) the instrument. From VAD scans data 3D wind Cartesian vectors $\mathbf{V} = u\mathbf{i} + v\mathbf{j} + w\mathbf{k}$ are retrieved from radial velocities $\mathbf{v}_{r,i}$ by solving the i-equations system:

$$V_{r,i} = u \cos \theta_i \cos \varphi_i + v \sin \theta_i \cos \varphi_i + w \sin \varphi_i \quad (1)$$

where φ_i is the elevation angle of the i^{th} beam and θ_i its azimuth angle, following the mathematical angle convention (Browning & Wexler, 1968). The three cartesian components of the winds (u, v, w) represent the west-east, south-north and vertical up-down directions, respectively. For the SPADE setup, VAD scans have $i = 4$ beams with a constant elevation ($\varphi_i = 80^\circ$) and known azimuths (θ_i). Hence, the retrieval requires solving the overdetermined linear equations system, vectorially expressed as:

$$\vec{V}_r^T = A \vec{V}^T \rightarrow \vec{V}^T \approx A^+ \vec{V}_r^T \quad (2)$$

where A^+ is the Moore-Penrose pseudo inverse of the coefficient matrix A . This method provides the least square solution (Päschke, Leinweber, & Lehmann, 2015). This algorithm relies on the assumption of a stationary and horizontally homogeneous wind field within the sampled air parcel in the scan disc. This hypothesis is, however, not ideal in highly turbulent conditions, especially at higher elevation as the scanning circle (distance from the lidar) increases with LOS distance. To ensure that the assumption is fulfilled, for each time and height, the wind vector retrieval is flagged by its Pearson correlation coefficient (R) as detailed in (Päschke, Leinweber, & Lehmann, 2015). Wind vectors associated with a $R < 0.9$ were rejected, which implies too weak correlation between the observed radial velocities and the theoretical radial velocities given by a perfectly stationary and horizontally homogeneous sine wave fit. The validity

of the algorithm was ensured within the framework of a previous field campaign (Mariani, Stanton, Whiteway, & Lehtinen, 2020) where retrieved wind flow agreed with radiosonde observations.

Horizontal flow-field data were then averaged, for both WXT520 surface weather transmitter and lidar VAD scans. This allowed us to analyze and study the air circulation and turbulence. Because winds are vectors, the method from Grange (2014) was used to average wind directions for values between 0° and 360°, where 0° = 360°.

1.3.3 Turbulence Characterization

Stare scans provide the highest temporal and spatial resolution data of vertical velocities $w(z)$. No assumption of stationary flow due to the travel time of the beams or duration of the scan sequence is required. Consequently, the turbulence of the low-level atmosphere was estimated by statistics moments of vertical velocities. More precisely, with $w'(z)$ being the variation from the mean vertical velocity as

$$w(z) = \overline{w(z)} + w'(z) \quad (3)$$

the variance σ_w^2 (2nd statistics moments) represents the intensity of the air mixing (turbulence intensity):

$$\sigma_w^2(z) = \overline{w'(z)^2} \quad (4)$$

and the skewness σ_w^3 (3rd statistics moments) provides information relative to turbulence's origin (O'Connor, et al., 2010; Hogan, Grant, Illingworth, Pearson, & O'Connor, 2009; Lenschow, Wulfmeyer, & Senff, 2000; Manninen, O'Connor, Vakkari, & Petäjä, 2016):

$$\sigma_w^3(z) = \overline{\left(\frac{w'(z)}{\sigma_w(z)}\right)^3} \quad (5)$$

Statistics were computed over 30 min periods, as in Newsom et al., (2019), Berg et al. (2017), Barlow et al., (2011) and de Arruda Moreira et al., (2018), centered at each 10 min; one third of the data is independent. Rolling averages over 1 h and 3 vertical range gates (9 m) were applied to smooth the data

to facilitate the analysis. This 9-m choice appears to be the best compromise to keep the finest vertical resolution and to smooth the data enough to enable a good analysis.

To investigate the origin of turbulence, the skewness of the vertical velocity, σ^3_w was computed as it represents the turbulent vertical transport of the momentum. Positive values of skewness ($\sigma^3_w > 0$) are associated with mixing initiated underneath the air parcel. This implies that the net upward transport of momentum is done by strong, narrow updrafts, compensated by downdrafts that are more widespread Hogan et al., (2009). Both thermal (convective, or buoyant) and mechanical (dynamical) processes can be responsible for turbulence initiated from below. For example, solar radiation causes surface-heating leading to convective instability of lower levels of the boundary layer and positive buoyancy. Purely mechanical turbulence can also be responsible for positive skewness measurements when strong near-surface wind shears occur because of surface roughness. In contrast, negative skewness ($\sigma^3_w < 0$) is associated with mixing initiated from above an air parcel. Processes such as radiative emissions by clouds, endothermic phase changes of atmospheric water content (condensation, solidification) or cold air advection at the top of the PBL cause negative skewness turbulence. In presence of a low-level or nocturnal jet, wind shear at the top of the PBL can initiate turbulence from above the mixing layer, witnessed by $\sigma^3_w < 0$. In this case, narrower, stronger downdrafts are observed, along with downdrafts that are more widespread Hogan et al., (2009).

The determination of the processes responsible for the turbulent mixing, whether initiated by below or above an air parcel, requires further investigations as they can be of dynamical and/ or thermal nature. Knowing that the PBL turbulence is initiated from the surface does not indicate whether it is driven by vertical shear of the horizontal wind near the surface, or by solar warming convective instability. Hence, assessing the relative importance of the vertical wind shear (VWS) along with other variables, such as cloud cover, surface temperature variations, winds (directions and magnitudes) as well as sunrise and sunset times must be considered. Following Manninen et al. (2018), we used the bulk VWS given by

$$VWS = \frac{(\Delta u^2 + \Delta v^2)^{\frac{1}{2}}}{\Delta z} \quad (6)$$

where higher VWS values indicate stronger dynamical induced turbulence, and lower or near-zero VWS mean weak or no dynamical mixing. Hence, in this study, when the variance of the vertical velocity has

higher values, indicating turbulent mixing, we use the VWS values to determine if the dynamical mixing contributes significantly, or whether the turbulence is thermally driven.

1.3.4 Atmospheric Water Content

Cloud and precipitation layers are composed of large liquid and solid water particles, typically 20 - 2000 μm (Russel, 2007); hence they exhibit high backscatter (β) capacities of the incident lidar's signal in comparison to aerosols. We note that hydrometeor and cloud phases impact β values.

In a cloud, liquid particles appear brighter to the lidar signal (higher backscatter β values) in comparison with solid particles, showing relatively lower backscatter value (β). This is due to the fact liquid (or mixed) clouds contain a large amount of small non-precipitating liquid droplets, highly reflective to the lidar. Clouds composed uniquely of solid particles only exist at temperatures lower than -38 °C in homogenic freezing (Pruppacher & Klett, 1997). However, in precipitation layers, solid particles are more reflective than liquid ones because they are better backscatters. It is important to mention that intense precipitation can extinguish the lidar's signal or can exhibit $\beta \geq 10^{-4.5} \text{ sr}^{-1} \text{ m}^{-1}$, hence be confused with cloud base. In this study, unsaturated, near-surface layers were identified by applying this reasoning, corresponding to lower β values. Specifically, a minimal threshold β value of $10^{-4.5} \text{ sr}^{-1} \text{ m}^{-1}$ was used to define cloud layers. It agrees with the threshold values found in the literature; Manninen, Marke, Tuononen, & O'Connor (2018) used a minimal β of $10^{-5} \text{ sr}^{-1} \text{ m}^{-1}$, while Huang et al. (2020) used a minimal β of $10^{-4} \text{ sr}^{-1} \text{ m}^{-1}$. After analysis, we chose a β value of $10^{-4.5} \text{ sr}^{-1} \text{ m}^{-1}$ as it fits more precisely the visual interpretation the data, for the whole campaign dataset, than either of the two latter threshold values. Moreover, backscatter coefficient values of $10^{-6} < \beta < 5 \times 10^{-6} \text{ sr}^{-1} \text{ m}^{-1}$ served to identify the PBL (Illingworth, et al., 2019; Manninen, Marke, Tuononen, & O'Connor, 2018), where aerosols act as tracers. Above the PBL, the concentration of aerosols decreases and $\beta < 10^{-6} \text{ sr}^{-1} \text{ m}^{-1}$. Analysing every vertical column of atmosphere with the Stare lidar data previously filtered by the SNR method, the PBL top was identified to match the altitude at which the backscatter values decrease below $\beta < 10^{-6} \text{ sr}^{-1} \text{ m}^{-1}$, for more than one range gate. However, the presence of low-level clouds or precipitation layers, identified by $\beta \geq 10^{-4.5} \text{ sr}^{-1} \text{ m}^{-1}$, can cause the extinctions of the lidar signal at altitudes lower than where β vanishes ($< 10^{-6} \text{ sr}^{-1} \text{ m}^{-1}$) due to the vertical extinction of aerosols. In this study, in that situation, we set the PBL top height equal to the cloud (or precipitation layer) base height.

The mixing layer or mixed layer (ML) is the convectively unstable layer of PBL, located above the surface layer and below the entrainment zone and the free atmosphere (Collaud Coen, et al., 2014). In the ML, the turbulence causes the mixing of the air in the layer, and may result in nearly homogenic gases concentration. The ML height (or depth) varies significantly in time, over the diurnal cycle, and depending on the meteorological conditions. Since the mixing and the turbulence intensities are directly related to one another, the ML is characterized using σ_w^2 . Specifically, the existence of a ML is characterized by a minimal turbulence intensity given by a minimal value of σ_w^2 . A multitude of methods exist to identify the ML height: e.g., Berg, Newsom & Turner (2017), used different threshold values of various variables to distinguish turbulent from laminar flow field. In this study, the turbulent flow is defined as an air parcel, at given time and height, where $\sigma_w^2 > 0.2 \text{ m}^2 \text{ s}^{-2}$ (Pearson, Davies, & Collier, 2009; Huang, et al., 2020). For a given time, if a ML exists, based on this threshold, this threshold also indicates its base and top heights. If the base of the ML is located below 60 m AGL, its height accuracy is missing due to the lidar's blind zone, and the retrieved value is set to 60 m AGL.

1.4 OVERVIEW OF THE PRECIPITATION EVENTS

To assess the origin of the air masses and the contribution of synoptic-scale processes onto the studied domain, this section presents the large-scale atmospheric patterns for all documented precipitation events of the SPADE campaign (Table 2). The whole campaign surface wind roses are also presented here to compare winds during and between the 13 documented precipitation events at both sites. More details about these events are given in Thériault et al. (2022). Fine-scale flow-fields over both sites, retrieved from Doppler lidars measurements, are presented and analysed in sections 1.6 and 1.7 of this paper.

1.4.1 Precipitation Events: Description and Synoptic Overview

Among the 13-documented SPADE precipitation events (Thériault et al., (2021); (2022)), the major ones (1, 5, 9, 13) brought more than 20 mm of precipitation, in water equivalent. They occurred during synoptic conditions favorable to precipitation development such as the passage of strong low-pressure systems composed of a deep upper-level trough (500 hPa) along the ocean coast supporting a well-formed closed surface low-pressure center located near southern Alberta. Only event #5 is attributed to a different synoptic pattern over southwest Canada, known as omega blockage. This blockage provides sustained

humidity advection from southern Pacific moist and warm air mass. This made event #5 being the longest-lasting event recorded during the campaign with more than 60 h of precipitation.

Intermediate-intensity precipitation events (3, 6, 7 and 12) brought 8 to 20 mm of precipitation and occurred during various large-scale circulation patterns; typically, shallower low-pressure systems with trajectories farther away from Fortress. Systems travelling north of the Kananaskis region results in less precipitation at our sites due to smaller moisture advected by flux from dryer Arctic air.

The synoptic pattern during event #12 consisted of a widespread low-pressure system advecting moisture from the Pacific. Specifically, even though a closed upper-level (500 hPa) low-pressure center over the northeastern BC travelling toward southwestern AB, the surface low-pressure center was not well formed offering unsuitable conditions for a major storm. The system grazed the coast along its trajectory and gained in intensity, deepening the aloft long-wave trough. That set up favourable conditions for upcoming high amounts of precipitation and the following days, 56.0 mm of precipitation were measured resulting in event 13. Both lidars data and large-scale patterns indicate that event #13 is the continuity of the event #12 and therefore, these two events (#12 and #13) may be considered as one single major storm giving almost 70 mm of precipitation.

Minor precipitation events (2, 4, 8, 10, 11) brought \leq 8 mm of precipitation to the southern Canadian Rockies and are linked with local and topographic effects. They are associated with high-pressure and upper-level ridge synoptic configurations inhibiting large-scale significant humidity advection over the Fortress region making it unfavorable to significant precipitation. Shallow low-pressure centers at the surface could exist over south-eastern Alberta but were constrained by the Pacific high-pressure extending inland over BC also resulting in minor precipitation.

1.4.2 Surface Winds

While large-scale systems drive winds in altitude, surface winds are channelled by the orography and have a dominant component aligned with the Rockies Mountains range axis (depicted in fig. 1, fig. 2c). Particularly, during the precipitation events, 2-m horizontal winds are dominantly oriented northwest, with few south-southeasterly winds occurrences (fig. 4). We note that the south-southeast component is attributed with precipitation events # 1 and #9. Between the documented events, overall surface winds

are distributed over broader directions, with the primary component of southerly winds and secondary component of northwesterly winds. The horizontal wind is generally parallel from the surface within all the valley height (i.e., between FJS and FPS altitudes) and turns above main orographic obstacles. The section 1.6 presents vertical profiles of horizontal winds. Moreover, the surface winds are more affected by the diurnal cycle during the precipitation events than between them (not shown). Daily winds were primarily south southeastward. Nocturnal winds were from either south or north-west. Between precipitation events, winds were lighter at both sites with weaker channeling effect, probably due to orography.

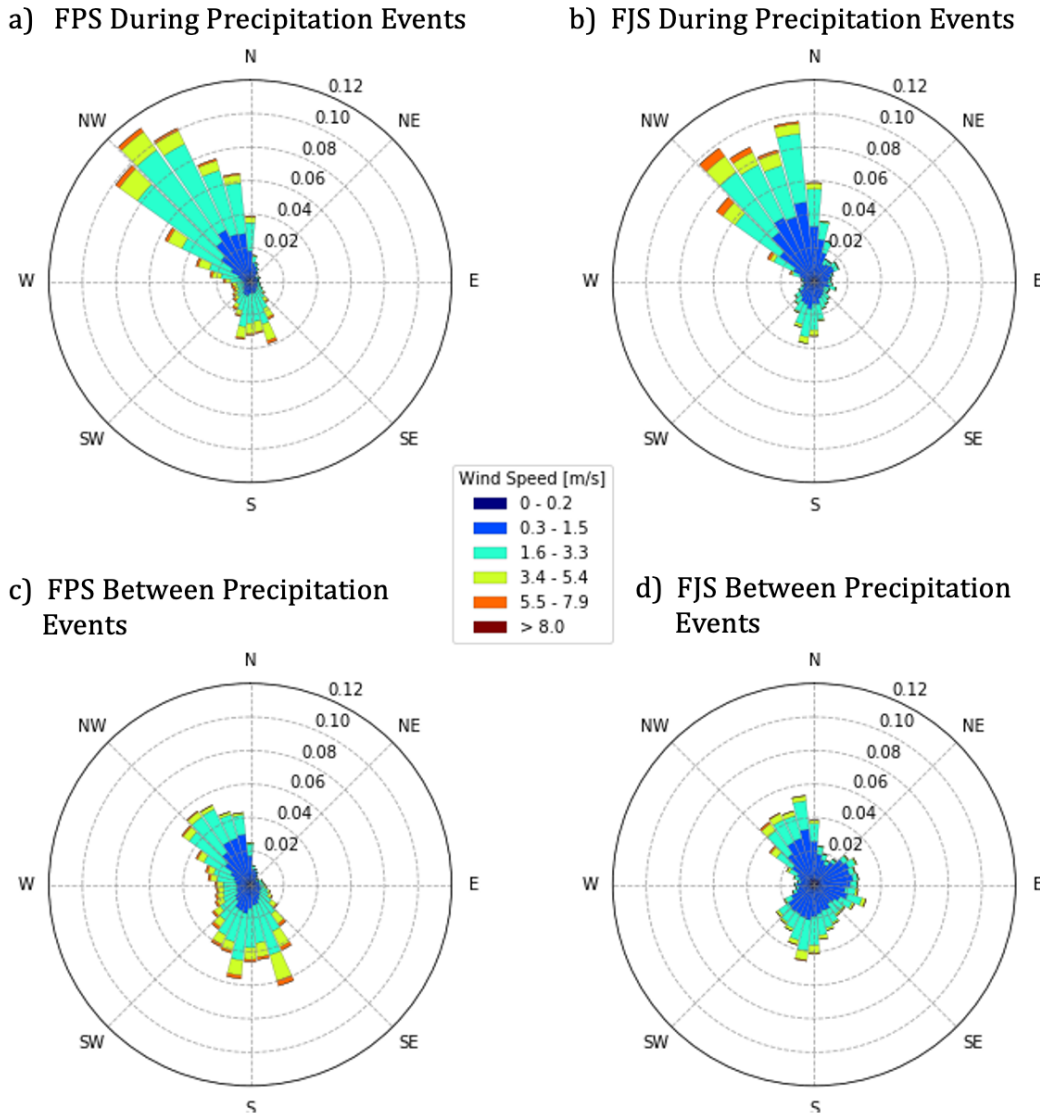


Figure 1.4 - Wind roses of occurrence of surface wind speeds and directions during the documented precipitation events at FPS (a) and FJS (b). and between the precipitation events at FPS (c) and FJS (d) measured by WXT520 (Thériault, et al., 2022).

1.5 ATMOSPHERIC AND SURFACE CONDITIONS OF THE CASE STUDIES

Further analysis is conducted using three representative case studies chosen to represent various atmospheric conditions reported during the 2019 SPADE: major precipitation events #1 and #13 and the minor precipitation event #8. Here after, they are respectively presented with daily data of 27 April 2019, 21 June 2019 and 30 May 2019. The event #5, constituting the storm occurring during an omega blockage pattern is not presented as a case study in this paper as the vertical motion were almost uniquely downward in quasi-constant precipitation. Furthermore, a clear-sky day with no precipitation (29 May 2019) is presented as a reference case for analysis. Large-scale circulation is investigated using synoptic map obtain from ERA5 (Hersbach, Bell, Berrisford, & Hirahara, 2020) as in Thériault J. M., et al. (2022). During the campaign, the weather station at FJS measured larger variations of daily temperature and humidity than at FPS, possibly due to less orographic cloud cover. Kananaskis valley was generally colder at night and warmer during the day resulting in more stable nocturnal PBL, hence less turbulent mixing and more turbulent unstable PBL at daytime.

1.5.1 Atmospheric and Surface Conditions of the Reference Case

The 29 May 2019, the reference day of this study, is characterized by a pressure ridge (fig. 5d). Sky clear conditions led to optimal solar radiation income. It resulted in important surface temperature variations with minimum reached right before sunrise (at 1144 UTC) and maximal reached in the local afternoon (approx. between 1800 UTC and 0100 UTC). This is especially true at FJS, where the temperature of $\sim 0^{\circ}\text{C}$ at night becomes $\sim 21^{\circ}\text{C}$ at ~ 1800 UTC. That diurnal temperature variation is as much as double that at FPS (fig. 7) where $\sim 9^{\circ}\text{C}$ at night becomes $\sim 19^{\circ}\text{C}$ at ~ 1800 UTC. Non-significantly varying dew points characterized the dry air. Weak surface winds of early morning strengthen throughout the day to become variable southwesterly winds at FPS and northerly winds at FJS, when PBL becomes unstable (presented in section 1.6). No precipitation was recorded that day. Along the field campaign, all the other days under a high pressure synoptic pattern presented very similar PBL and turbulence behaviours (not shown in this paper).

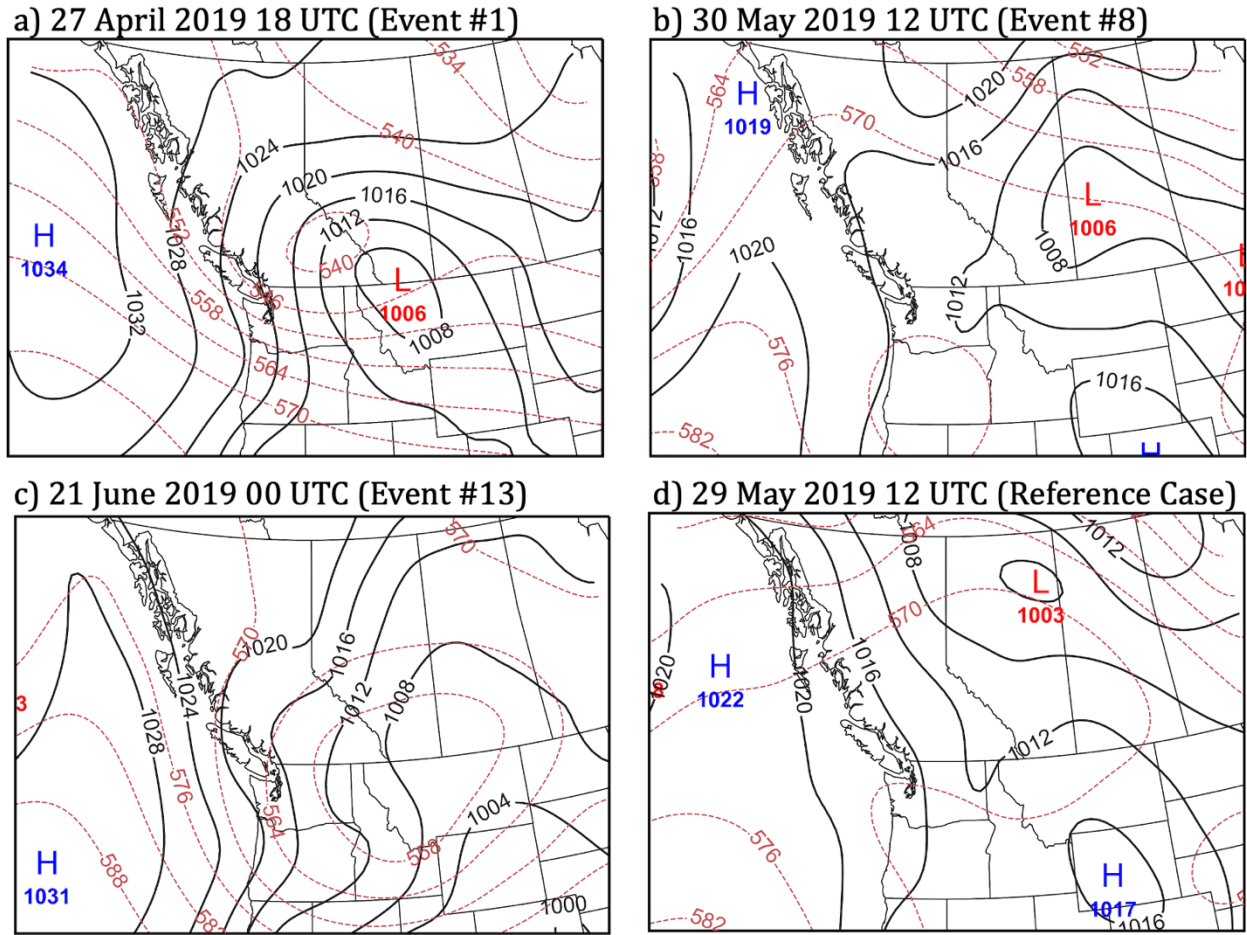


Figure 1.5 - Synoptic patterns during the case studies represented by the surface (MSL) pressure patterns (black lines) and upper level 500 hPa geopotential heights (red lines) computed by ERA5. a) event #1; b) event #2, c) event #3, d) reference case.

1.5.2 Atmospheric and Surface Conditions of the Event #1

Event #1 is characterized by a baroclinic low-pressure system supported by an upper level (500 hPa) trough and a strong high-pressure over the Pacific (fig. 5a). It created a surface pressure trough from northwestern BC to Colorado (USA). It brought precipitation over our sites on 26-28 of April 2019 (fig. 6). The surface low-pressure travelled from NW BC toward SE to pass directly through the SPADE domain, at 0500 UTC on 27 April 2019, and left toward Colorado. The passage of that synoptic system resulted in the pressure minima at 1900 UTC 27 April 2019 (fig. 6). An associated wind switch from southerly to north-easterly winds (fig. 6) was due to the synoptic cyclonic circulation around the system center initially located west of our sites then east.

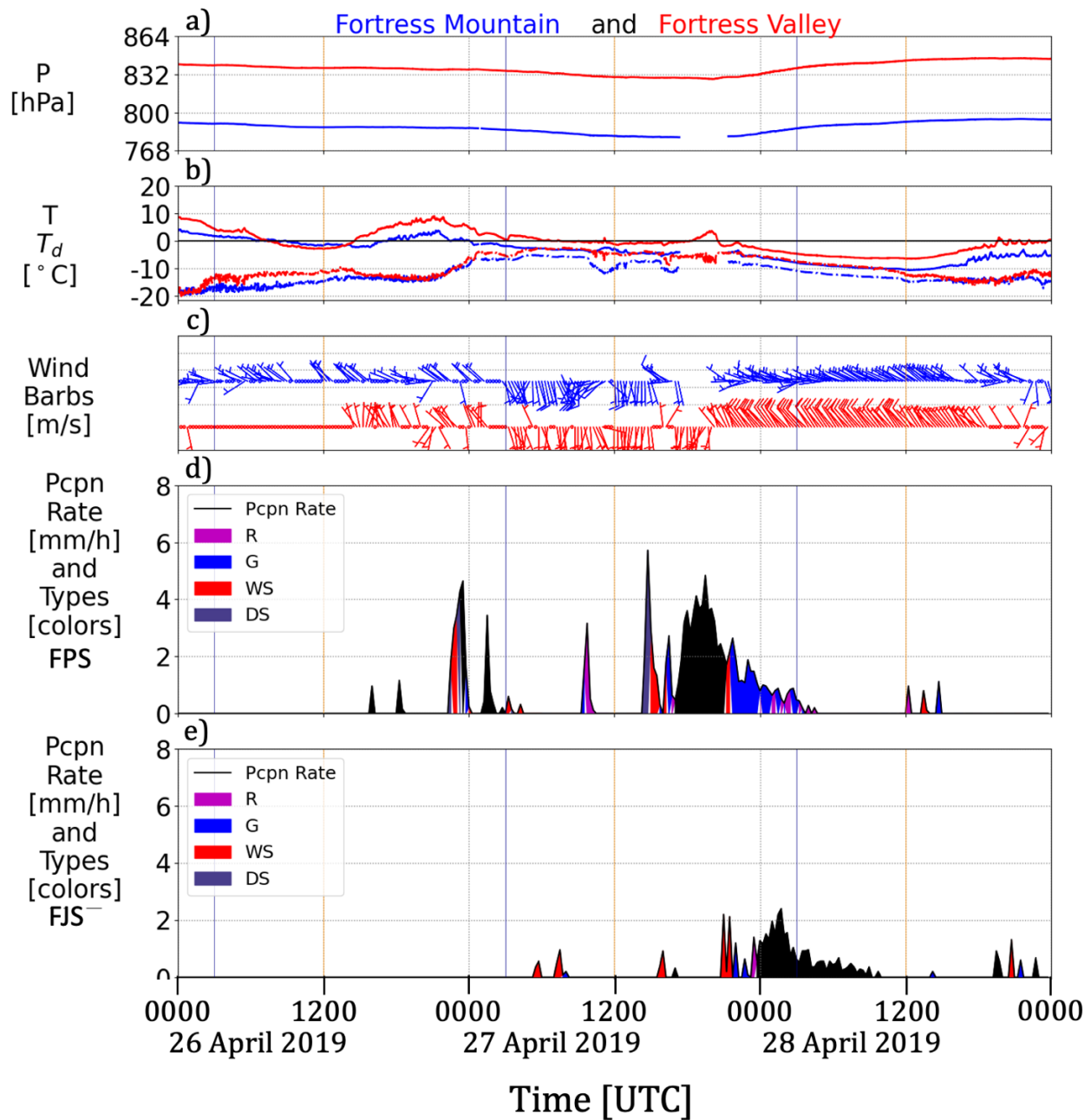


Figure 1.6 - Meteogram for on-site surface conditions during 3 days from 26 to 28 April 2019, including storm #1. Top three panels respectively represent surface atmospheric conditions as observed by the WXT520 (blue for FPS; red for FJS); a) station pressure (P); b) temperature (T) in solid lines and dew point temperature (T_d) in dotted lines; c) surface winds barbs. Bottom two panels show precipitation rates (pcpn rate) as measured by precipitation gauges and main hydrometeor types at the surface retrieved from disdrometers measurements (R: rain, G: graupels or snow pellets, WS: wet snow, DS: dry snow, black is unknown) at FPS (d) and at FJS (e). For all panels, sunrise and sunset are depicted by yellow and blue vertical lines respectively.

Initially on 26 April 2019, surface conditions were unsaturated with low dew points (fig. 6) and increasing temperatures due to solar radiation income and surface heating. Lidar data show uplifting motion around 1800 UTC 26 April 2019, lasting until the beginning of the precipitation event (discussed in section 1.6). Saturation eventually occurs at both sites around 0000 UTC 27 April 2019 when temperatures decrease at both sites, slightly below freezing point. Various precipitation types were recorded at FPS and wet snow at FJS until 1900 UTC 27 April 2019, corresponding to the passage of the system on Fortress and the maximal precipitation intensity (of unknown type) at FPS. Afterward, precipitation types are mainly wet snow with a few snow pellets at FPS and unknown at FJS. Winds at FPS have a western component and vary more compared to FJS due to orographic channeling. Moreover, precipitation was temporally delayed in the valley compared to that on the mountain even though weather conditions timing coincides over both sites (fig. 6). Finally, data also show early wet snow precipitating on the 26 April 2019, at FPS only. The temperature increase, the local diurnal cycle, along with mainly weak northwesterly winds, at times southerly, suggest this early precipitation is convectively driven and associated with large-scale warm air advection.

1.5.3 Atmospheric and Surface Conditions of the Event #8

After several sunny days of increasing daily mean temperature over 0°C , rain occurred over both sites as humidity advection from the Pacific, over southern Rockies area allowed precipitation. As for the first event, event #8 is associated with the passage of a low-pressure (fig. 5b). This time however, the system was weakly supported by a shallow upper-level trough (500 hPa) farther over the northern AB/BC border. A high-pressure over Wyoming (USA) constrained the low-pressure to the north of our domain resulting into a minor precipitation event of 6.5 mm. The surface pressure reached its minimum slightly after 0000 UTC 30 May 2019 (fig. 7) when temperatures decreased, and relative humidity increased. The low-pressure system crossed the northern AB-SK border at 0600 UTC 30 May 2019 and the surface winds at FPS shifted from southwesterly to northerly winds (fig. 7). At FJS, weak northerly winds on the 29 May 2019 only strengthened at 1400 UTC 30 May 2019, simultaneously with the rain. Clouds limited the solar heating, and weaker convection occurred in the afternoon compared to the reference day (both shown on fig. 7).

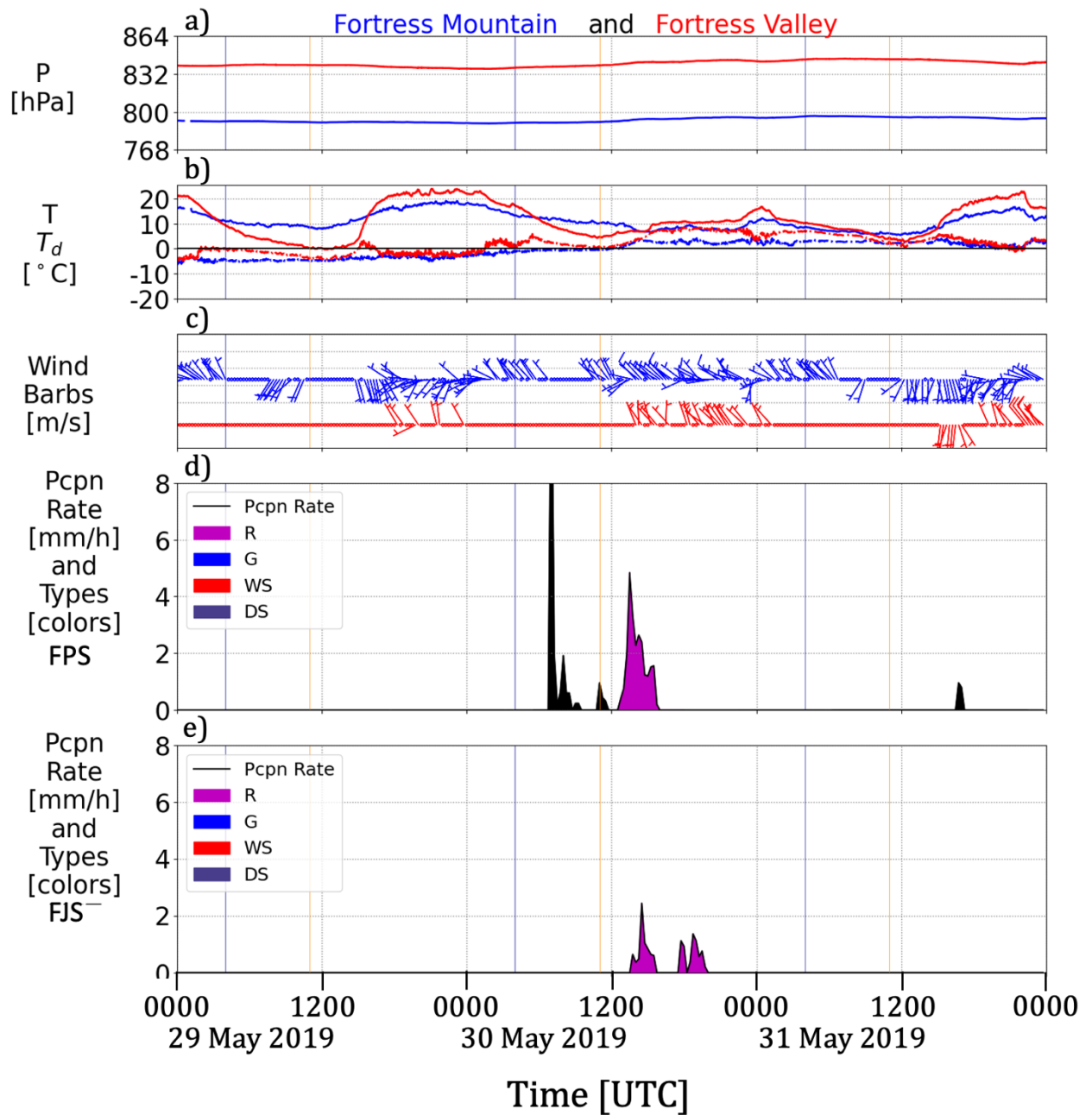


Figure 1.7 - Meteogram for surface conditions during 3 days from 29 to 31 May 2019, including storm #8 and the reference day. Top three panels respectively represent surface atmospheric conditions as observed by the WXT520 (blue for FPS; red for FJS); a) pressure (P); b) temperature (T) in solid lines and dew point temperature (T_d) in dotted lines; c) surface winds barbs. Bottom two panels show precipitation rates (pcpn rate) as measured by precipitation gauges and main hydrometeor types at the surface retrieved from disdrometers measurements (R: rain, G: graupels or snow pellets, WS: wet snow, DS: dry snow, black is unknown) at FPS (d) and at FJS (e). For all panels, sunrise and sunset are depicted by yellow and blue vertical lines respectively.

1.5.4 Atmospheric and Surface Conditions of the Event #13

Prior to the precipitation event #13, on the 17 June 2019, a deep low-pressure system, initially centered over northwestern Pacific and travelling eastward hit coastal northern BC. It resulted in a surface meridional trough along the coast, deepening and expanding from Vancouver Island to the low-pressure center. On the 19 June 2019, this large widespread system travelled southeast-ward, supported by a closed pressure-center at 500 hPa (fig. 5c). This instigated multiple precipitation occurrences over Fortress as rain at FJS and as a mix of rain and small iced particles at FPS. We observed associated fluctuating west winds at FPS and sporadic north winds at FJS (fig. 8). The diurnal temperature variation was damped by the presence of clouds and additional temperature fluctuations were measured along the day at both sites due to evaporative cooling of precipitation into the unsaturated lower atmosphere.

By the 20 June 2019, the system reached the southern Canadian Rockies, and the atmosphere became saturated. At 1200 UTC, the system slowed down and tightened as it travelled south of SPADE domain. Its cyclonic circulation caused an easterly upstream flow over the eastern side of the Canadian divide bringing important amounts of precipitation. Mostly wet snow was observed at FPS as the temperatures oscillated around freezing point at FPS. FJS received rain with temperatures above freezing point. At both sites, surface winds were southerly from 0200 UTC to 2100 UTC with the low-pressure centered over Wyoming (USA) constrained by the high-pressure building over the Pacific. More precisely, these orographically-enhanced precipitations affected all the Canadian Rockies with a maximal intensity of precipitation at Fortress sites around 0900 UTC 21 June 2019 (fig. 8).

The precipitation event #13 began at 2100 UTC 20 June 2019, simultaneously with a distinct surface wind switch from southerly to north-westerly. We notice an associated cooling at both FPS and FJS along with an increase of humidity at FJS. This corresponds to evaporative cooling by precipitation falling into the low atmosphere. Warmer and dryer air at FJS resulted in a delay in precipitation reaching the surface during the saturation process. Precipitation started as rain at both sites and switched to wet snow and snow pellets as their temperature decreased to 0°C. This phase transition happened at FPS at ~ 0400 UTC 21 June 2019 and approximately 4 hours later at FJS (fig. 8).

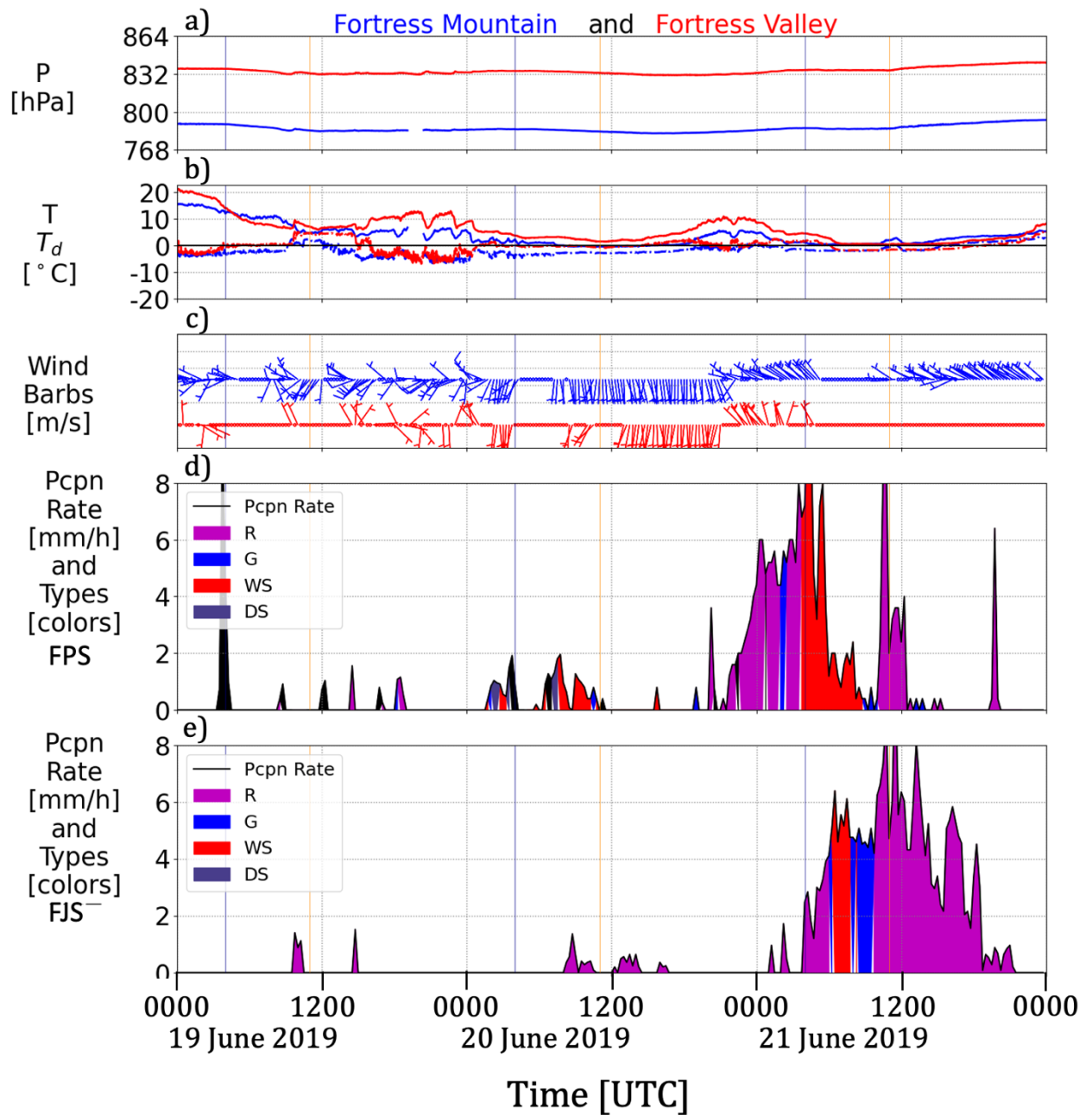


Figure 1.8 - Meteogram for surface conditions during 3 days from 19 to 21 June 2019, including storm #13. Top three panels respectively represent surface atmospheric conditions as observed by the WXT520 (blue for FPS; red for FJS); a) pressure (P); b) temperature (T) in solid lines and dew point temperature (T_d) in dotted lines; c) surface winds barbs. Bottom two panels show precipitation rates (pcpn rate) as measured by precipitation gauges and main hydrometeor types at the surface retrieved from disdrometers measurements (R: rain, G: graupels or snow pellets, WS: wet snow, DS: dry snow, black is unknown) at FPS (d) and at FJS (e). For all panels, sunrise and sunset are depicted by yellow and blue vertical lines respectively.

1.6 HORIZONTAL FINE-SCALE FLOW-FIELDS OF THE CASE STUDIES

In addition to the 2-m horizontal winds presented in section 1.4.2, horizontal winds retrieved by the 2 lidars (at FPS and FJS) are analysed to investigate the flow patterns on the eastern side of the divide above the surface, up to \sim 5 km AMSL.

Overall, the entire campaign dataset reveals that, at heights above FPS, horizontal winds were primarily westerly (fig. 9) in agreement with the large-scale cyclonic circulation (section 1.5). However, during major storms events 1, 9 and 13, data also reveals that winds were easterly, once the low-pressure systems have reached the eastern side of the divide with latitude as low as the studied area (50° N). These results agree with the literature with the large snowfalls associated with easterly flows (Stewart, et al., 1995). Moreover, the horizontal flow field was more laminar above the height of the continental divide (above 3 km AMSL) in comparison to lower altitudes where the flow was more variable (in direction and magnitude) due to the topography roughness and thermodynamic impacts.

For most of the campaign, the VWS was weak with values $\leq 0.03 \text{ s}^{-1}$. Most of the strongest VWS occurred during the afternoons and evenings (from 1600 UTC to 0400 UTC). This timing fits with a more developed mixing layer according to the solar diurnal cycle. Furthermore, a few periods of non-negligible VWS were recorded at night during clear-sky episodes indicating the presence of nocturnal low-level jets.

1.6.1 Fine-Scale Horizontal Flow-Fields of the Reference Case

During the reference day, 29 May 2019 (fig. 9), horizontal winds were stronger late at night between 0000 UTC and 0100 UTC and in the afternoon from 1800 UTC to 0000 UTC. Winds were maximal during the local afternoon with values up to 25 m s^{-1} . In the valley at FJS, these maximum winds were westerly and measured at ~ 2000 UTC above 2 km AMSL, corresponding to FPS's height. On the mountain at FPS, maximum winds were northerly and measured at ~ 1800 UTC above 3 km AMSL, corresponding to the continental divide's height (fig 9 a, b). These weaker winds at the surface intensifying with height in the PBL characterize a typical unstable thermally convective PBL. VWS confirms this convectively unstable behaviour with higher values ($\sim 10^{-1} \text{ s}^{-1}$) measured at all heights during the afternoon (1800 UTC to 0000 UTC) at both sites. In contrast, during night and morning, a calm atmosphere was measured at both sites with wind speeds of $\leq 5 \text{ m s}^{-1}$ and VWS $\sim 0.025 \text{ s}^{-1}$ (fig. 9).

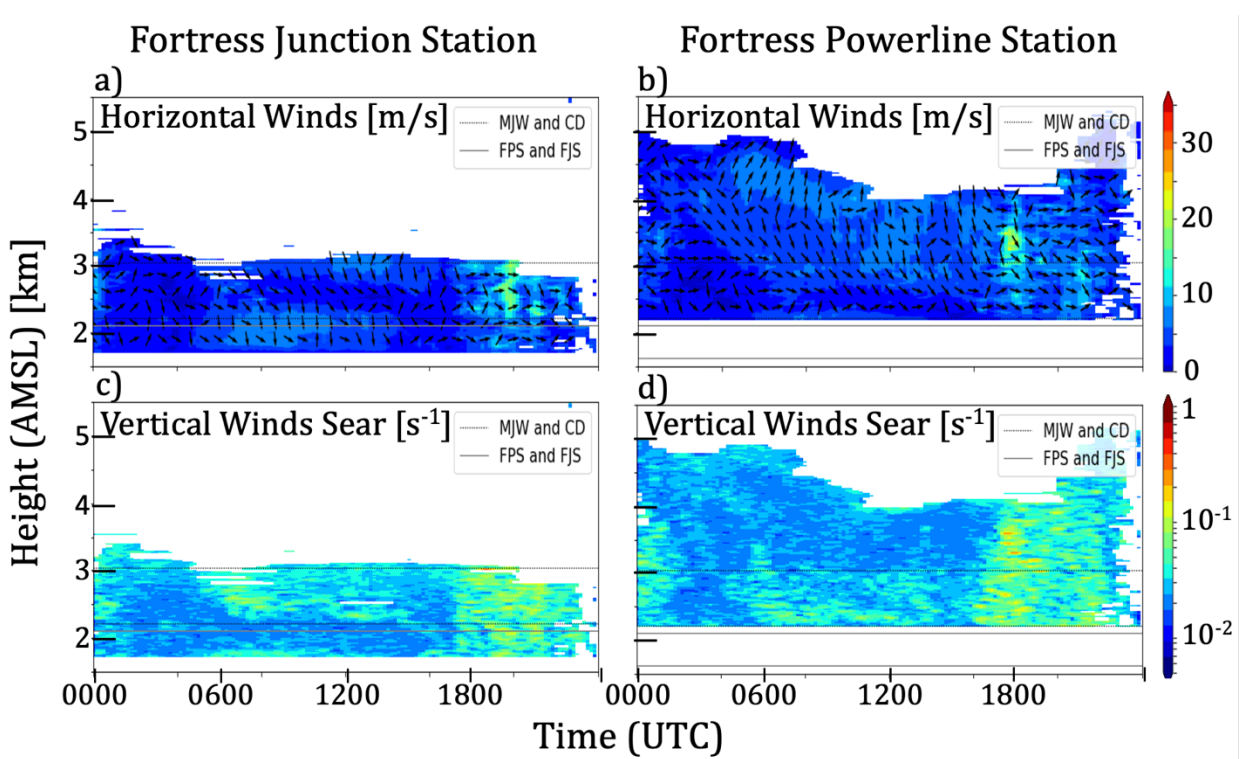


Figure 1.9 - Horizontal winds speed (colors) and direction (arrow) at FJS (a) and FPS (b) during the reference day, 29 May 2019, obtained by lidars VAD scan. Vertical shear of the horizontal wind (colors) at FJS (c) and FPS (d). Horizontal lines represent respectively from higher to lower altitudes, the Continental Divide (CD), Mount James Walker (MJW), FPS site and FJS site.

Moreover, at FJS a local maximum of horizontal wind speed $\sim 7.5 \text{ m s}^{-1}$ was measured from 0600 UTC to 1100 UTC below 2.3 km, suggesting a northwesterly nocturnal low-level jet. Associated VWS is maximal below and above this jet, namely very close to the surface ($\sim 0.05 \text{ s}^{-1}$) and above 2.3 km ($\sim 0.01 \text{ s}^{-1}$). Hence, the mechanical wind shear was maximal below and above the nocturnal low-level jet due to the maximal vertical gradients of wind velocity and direction. At FPS on the other hand, $\sim 7.5 \text{ m s}^{-1}$ south-southwesterly horizontal winds at higher altitude ($\sim 4 \text{ km}$) were measured from 0400 UTC. This flow settled temporally after a northwesterly flow, and constrained this later toward lower altitudes until $\sim 1000 \text{ UTC}$, when the northwesterly flow intensified just above the CD. Between 0400 UTC and 1300 UTC at FPS, higher values of VWS were confined between the surface and the CD's height.

1.6.2 Fine-Scale Horizontal Flow-Fields of the Event #1

During the event #1 on the 27 April 2019 (fig. 10), horizontal winds were stronger overnight and weaker in the afternoon, compared to the reference day (fig. 9). Average wind velocity of $\sim 15 \text{ m s}^{-1}$ was measured between 0700 UTC and 1700 UTC (fig. 10) and maximum wind speed of $\sim 25 \text{ m s}^{-1}$ was reached at ~ 1030 UTC at FPS and at ~ 1130 UTC at FJS. The 1 h delay between FJS and FPS may be due to the extra time required for the wind to overcome the valley channeling. More specifically, at FJS at ~ 2.3 km just above FPS's height and at FPS slightly below the CD height. At that moment, winds intensified throughout the entire vertical column and the upper level wind (above the CD) switch occurred from southwesterly to northwesterly flow. This wind switch occurred ~ 1100 UTC, hence ~ 6 h after the passage of the low-pressure center over Fortress domain (section 1.5.2). A gap in the data at FJS from ~ 1700 UTC and ~ 2000 UTC between ~ 2.1 km and ~ 2.8 km AMSL is associated with a loss of the lidar's signal. Specifically, very weak backscatter values, probably due to aerosols washed by precipitation.

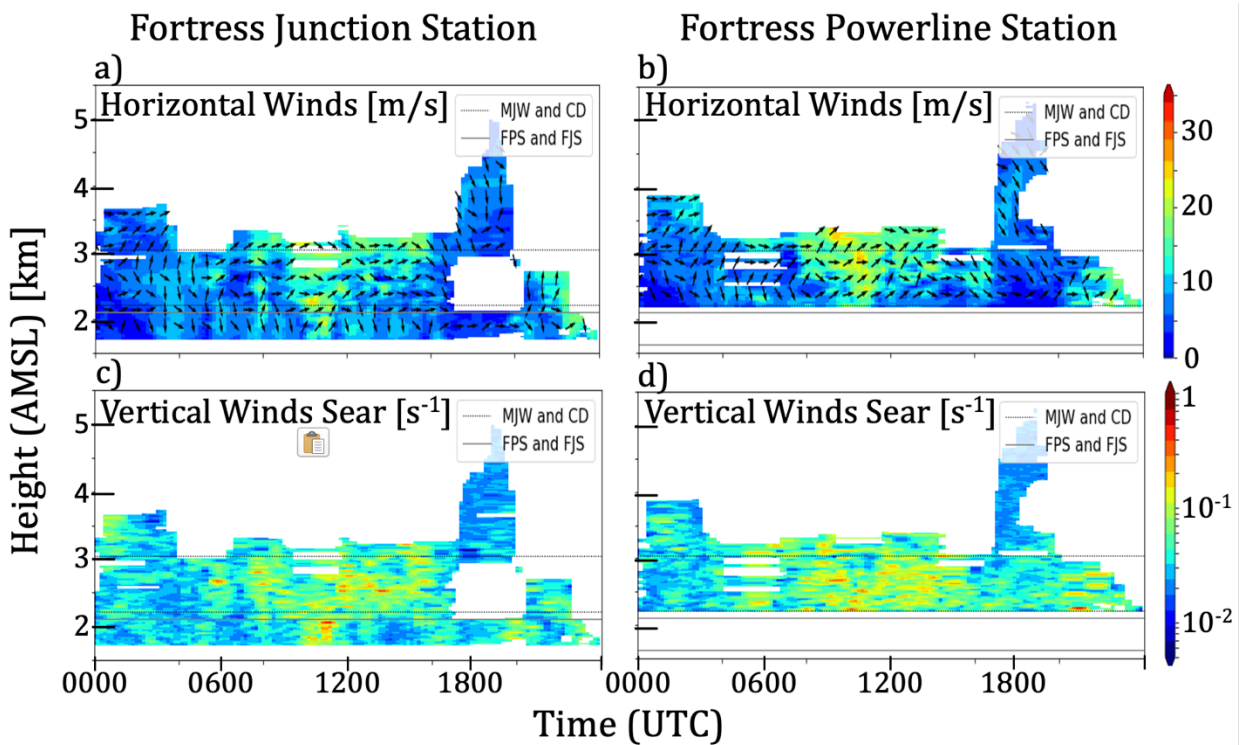


Figure 1.10 - Horizontal winds speed (colors) and direction (arrow) at FJS (a) and FPS (b) during the precipitation event #1, 27 April 2019, obtained by lidars VAD scan. Vertical shear of the horizontal wind (colors) at FJS (c) and FPS (d). Horizontal lines represent respectively from higher to lower altitudes, the Continental Divide (CD), Mount James Walker (MJW), FPS site and FJS site.

These stronger winds correspond to higher values of VWS ($\sim 0.1 \text{ s}^{-1}$) with its maximum VWS exceeding 0.5 s^{-1} at 1030 UTC (fig 10, c-d). This maximal VWS occurred just below FPS's height, meaning below the maximal wind speed, here again caused by vertical wind gradient. Around 1030 UTC, the VWS was mainly magnitude shear as the direction along the atmospheric column was dominantly from west and only slightly veering at that moment and height (fig. 10b). However, important directional shear occurred at other moments throughout the day at both sites; Particularly from 0200 UTC to 0600 UTC at FJS and from 0400 UTC to 0800 UTC at FPS where a southerly flow was measured above a northerly flow. In fact, low-level wind was channelled and oriented mainly along the valley while the zonal component was stronger with altitude. Finally, even with a dominant westerly flow, data show more variable winds, in time and along the vertical axis, during this event compared with the reference day, both in direction and velocity. These variabilities witness the presence of more fine-scale flow-field processes and features.

1.6.3 Fine-Scale Horizontal Flow-Fields of the Event #8

During event #8, 30 May 2019 (fig. 11), horizontal winds at Fortress were generally westerly and calm ($\sim 5 \text{ m s}^{-1}$), similarly with the reference day (fig. 9). More specifically, winds were slightly stronger late at night between 0000 UTC and 0100 UTC and in the afternoon, from 1300 UTC until 0000 UTC. However, winds strengthened to $\sim 7.5 \text{ m s}^{-1}$ slightly before 1400 UTC, simultaneously with the beginning of the rain at FJS. This corresponds to local morning (1000 MDT). Hence it was too early to be due to thermal convection driven by solar radiation income. At that moment, for a short period, shallow layers where the wind was up to $\sim 20 \text{ m s}^{-1}$ were measured at FJS as $\sim 2.8 \text{ km}$ and between 2.3 km and 3 km at FPS.

The VWS was maximal at both sites at $\sim 1300 \text{ UTC}$ with values up to 0.5 s^{-1} at FPS and VWS remained $\sim 0.1 \text{ s}^{-1}$ until 2200 UTC. More precisely, FJS data show VWS $\sim 0.2 \text{ s}^{-1}$ above the valley while FPS data show stronger VWS below CD's heights mainly due to directional shear. Additionally, during the previous night ($\sim 0400 \text{ UTC}$ to 0900 UTC , 30 May 2019) the wind was weak ($\leq 7.5 \text{ m s}^{-1}$) and the flow field was generally uniform with minimal VWS.

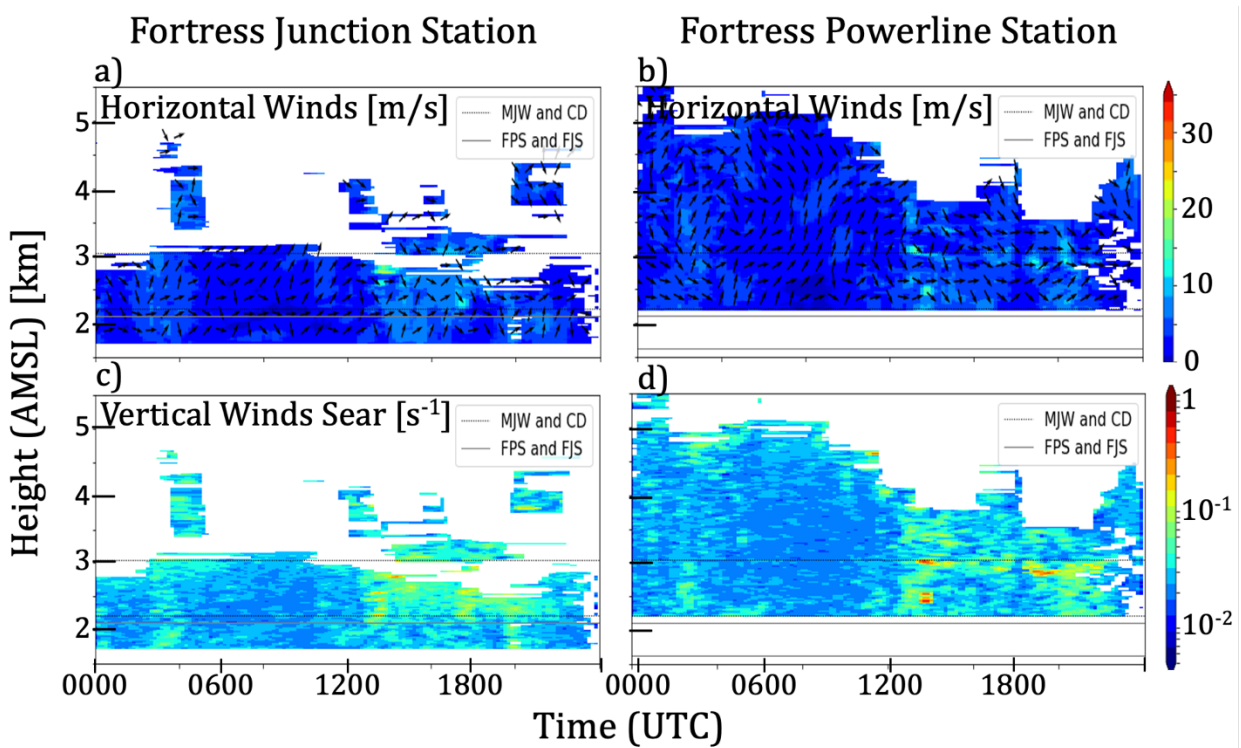


Figure 1.11 - Horizontal winds speed (colors) and direction (arrow) at FJS (a) and FPS (b) during the precipitation event #8, 30 May 2019, obtained by lidars VAD scan. Vertical shear of the horizontal wind (colors) at FJS (c) and FPS (d). Horizontal lines represent respectively from higher to lower altitudes, the Continental Divide (CD), Mount James Walker (MJW), FPS site and FJS site.

1.6.4 Fine-Scale Horizontal Flow-Fields of the Event #13

On the 21 June 2019, at the beginning of the event #13, horizontal winds were as fast as 20 m s^{-1} and VSW up to 0.2 s^{-1} , between 0000 UTC and ~ 0500 UTC. The strongly attenuated lidar signal, especially at FPS, restricts the analysis to a very shallow lower atmosphere. However, available data show calm wind and weak VWS between 0500 UTC and 1000 UTC at both sites. Afterwards, in the early morning (~ 1000 UTC) when precipitation changed to rain at both sites, winds strengthened to up to 25 m s^{-1} at $\sim 2.1 \text{ km AMSL}$ with a mainly westerly, downslope component. Associated VWS up to 0.6 s^{-1} were measured and lasted until the end of the precipitation, namely ~ 2200 UTC. FJS data reveals, here again, that low-level winds are aligned with the valley, except 0500 UTC and 1000 UTC when they are the weakest. We also note that winds are stronger above the valley and primarily south-westerly while they are weaker and more directionally variable at altitude lower $\sim 2 \text{ km}$.

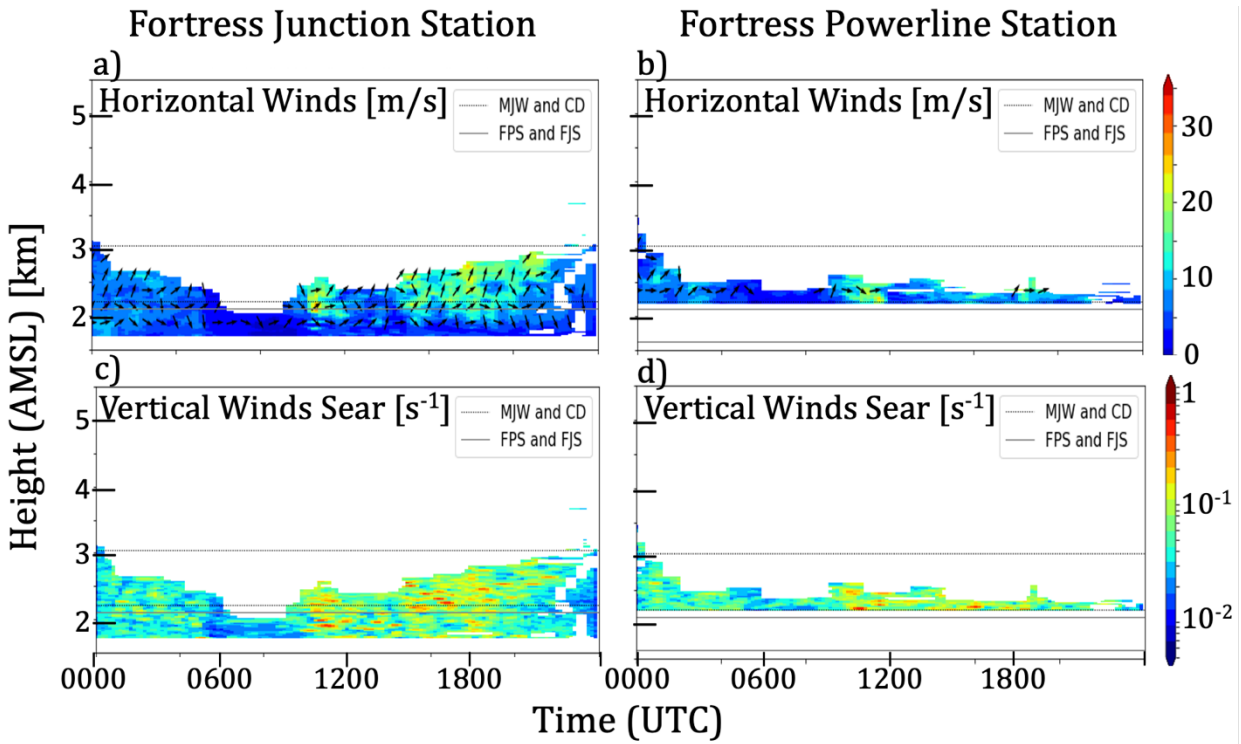


Figure 1.12 - Horizontal winds speed (colors) and direction (arrow) at FJS (a) and FPS (b) during the precipitation event #13, 21 June 2019, obtained by lidars VAD scan. Vertical shear of the horizontal wind (colors) at FJS (c) and FPS (d). Horizontal lines represent respectively from higher to lower altitudes, the Continental Divide (CD), Mount James Walker (MJW), FPS site and FJS site.

1.7 VERTICAL FINE-SCALE FLOW-FIELD AND TURBULENCE OF THE CASE STUDIES

Vertical air motion analysis of the entire field campaign revealed generalized upward motions prior to precipitation, followed by downward motion of precipitating particles prior to the precipitation recorded at the surface. During major precipitation events, the synoptic pattern (fig. 5a) created large-scale ascending motion in the vicinity of the low-pressure or the troughs. Moreover, the circulation around the low-pressure forcing the air to encounter the mountains enhanced orographic lifting inducing precipitation.-Additionally, during major precipitation events, the cloud cover reduced the solar radiation and limited the convective mixing, hence convective updrafts (fig. 14, 16).

In cases of minor precipitation events or local effects, upward motions are mainly convectively driven in an unstable atmosphere, as the larger circulation did not contribute significantly to the uplifting. This later upward motion contributes to fine-scale convective cloud formation aloft as during the reference day at ~ 1900 UTC.

1.7.1 Vertical Fine-Scale Flow-Field and Turbulence of the Reference Case

On clear skies conditions, the aerosol layer constituting the lower boundary layer was generally confined in the valley at FJS with a depth of ~800 m (i.e., a height ~ 2.5 km AMSL) (fig. 13a). On the mountain at FPS, the layer of higher concentration of aerosol was ~ 1.2 km depth, extending vertically higher than the continental divide (CDH ~ 3 km AMSL) up to $z_{aer} = 3.3$ km AMSL (fig. 13b). Retrieved PBL height, given by $\beta < 10^{-6}$ sr $^{-1}$ m $^{-1}$ are deeper with values of ~ 2 km at FJS and ~ 3 km at FPS, deeper than the typical, theoretical value of 1 km found in literature (Stull, 1988). This is explained by high orographic roughness with the closest orographic feature, Mt James Walker (MJW) being ~ 2.2 km AMSL high. Previous research over different terrain heights (e.g., Huang and al., 2020, Barlow and al., 2011, Berg et al., 2017) obtained values ranging from 1 to 2 km. At both stations, the boundary layer deepens when convection is diagnosed, in agreement with literature (Stull, 1988).

A calm atmosphere with weak vertical movement was observed from 0200 UTC to ~ 1700 UTC. Then at ~ 1700 UTC, a mixing layer was formed rapidly at both sites (fig. 13 e, f). At FJS, the ML height was equal to that of the continental divide while it was higher than 4 km at FPS (fig. 13 a, b), and continued to deepen until 0000 UTC to reach 5 km. So, from 1700 UTC until 0000 UTC, the atmosphere was turbulent. At FJS, the turbulence was consistent with $\sigma_w^2 \sim 2$ m 2 s $^{-2}$ for the entire period from the surface up to the PBL top. At FPS, on the other hand, the turbulence was maximal between 1700 UTC and 1900 UTC with $\sigma_w^2 \sim 3$ m 2 s $^{-2}$ while upward vertical motion was measured. Then at 1900 UTC, it weakened at $\sigma_w^2 \sim 1$ m 2 s $^{-2}$ at (fig. 13 e, f) when motion was replaced by downward motion (fig. 13 c, d). This time interval 1700 UTC until 0000 UTC corresponds to the period of stronger VWS (section 6 c, d). More specifically, at both sites, the stronger turbulence (fig. 13 e, f) occurred simultaneously with dominant upward motion from 1700 UTC to 1900 UTC at FPS and from 1830 UTC to 2200 UTC at FJS (fig. 13 c, d).

FJS measured weak downward motion for a ~ 1 h period from 1700 UTC to 1800 UTC, while the ML developed. The positive skewness of the vertical winds reveals that the turbulence was driven by the surface (fig. 13 g, h), mainly from 1830 UTC at FPS. At FJS, the positive skewness shows that until 2100 UTC, the turbulence was also mainly driven from below the air parcel but only at altitudes higher than the valley depth (~ 2.5 km). After 2100 UTC, the turbulence was driven from the surface. On the other hand, at FPS the turbulence from 1700 UTC to 1900 UTC originated from surface warming and from cooling aloft. Then, from 1900 UTC, surface warming became the dominant source of turbulence (fig 13 g, h).

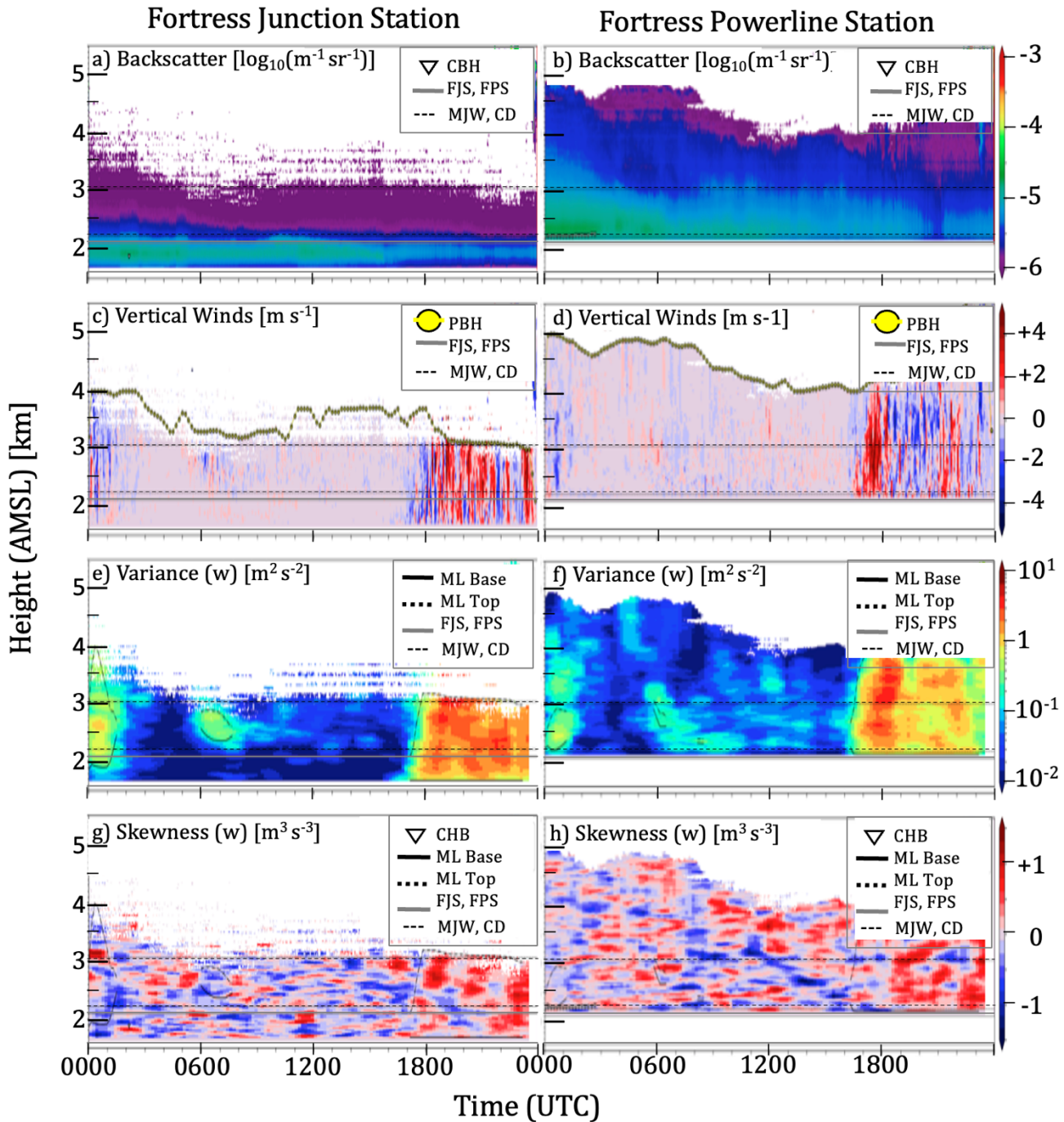


Figure 1.13 - Time-height section on the 29 May 2019 on the reference day from collected Doppler Lidar measurements at FJS (left) and FPS (right) sites. a-b) backscatter coefficient with higher (lower) values indicating more (less) reflectivity. Inverted triangles correspond to the cloud-base-height (CBH).; c-d) Vertical velocity with blue (red) indicating downward (upward) motions. Yellow dots indicate the planetary boundary layer (PBL) height.; e-f) Variance of the vertical velocity with larger (lower) values in red (blue).; g-h) Skewness of the vertical velocity with blue (red) indicating negative (positive) values. a-h) Grey solid horizontal lines represent FJS and FPS heights and black dotted lines illustrate Mount James Walker (MJW) and the continental divide (CD)'s heights. e-h) ML base (top) heights are given by the solid (dashed) lines.

Data reveals thermal stability at night, alternating with convective instability during sunny days (fig. 13). Therefore, the atmosphere was non-turbulent at night, with the nocturnal PBL at FJS being confined in the valley, while at FPS it extended up to 3 km above the surface. At daytime, a mixing layer was formed at both sites with the flow-field becoming turbulent. The turbulence was mainly driven by below the air parcel, which reveals that the solar radiation heated the surface and generated turbulent motion and updrafts. This also explains the temperature variations described in section 1.5.2. Moreover, at 1900 UTC, clouds formed at \sim 4,5 km height above both sites. This has affected the temperature between 1800 UTC and 0000 UTC, especially at FJS (fig. 7b).

During clear-sky periods, local night-time flow over both sites was mainly laminar as illustrated by low σ_w^2 values (fig. 13 e, f). This is confirmed by near-zero vertical velocities (fig. 13 c, d). The turbulence intensities increased at daytime until forming the ML around 1700 UTC. Through the highly noisy data, it is shown that surface warming primarily driven the mixing. This convective mixing is also highlighted by the strong updrafts at both sites, respectively between 1630 UTC and 1830 UTC at FPS (fig. 13d) and from 1830 UTC until the end of the day at FJS (fig. 13c).

1.7.2 Vertical Fine-Scale Flow-Field and Turbulence of the Event #1

During the major precipitation event #1, ceilings as low as hundreds of meters, due to clouds and precipitation were observed at both sites, as shown by backscatter values of $\beta \geq 10^{-4.5} \text{ sr}^{-1} \text{ m}^{-1}$. In particular, for the four periods included in 0000 UTC to 0100 UTC, 0300 UTC to 1000 UTC, 1300 UTC to 1600 UTC and 2100 UTC to 0000 UTC, the cloud base height (CBH) was measured at the surface itself (fig. 14 a, b) due to the lidar's signal extinguishment by precipitation.

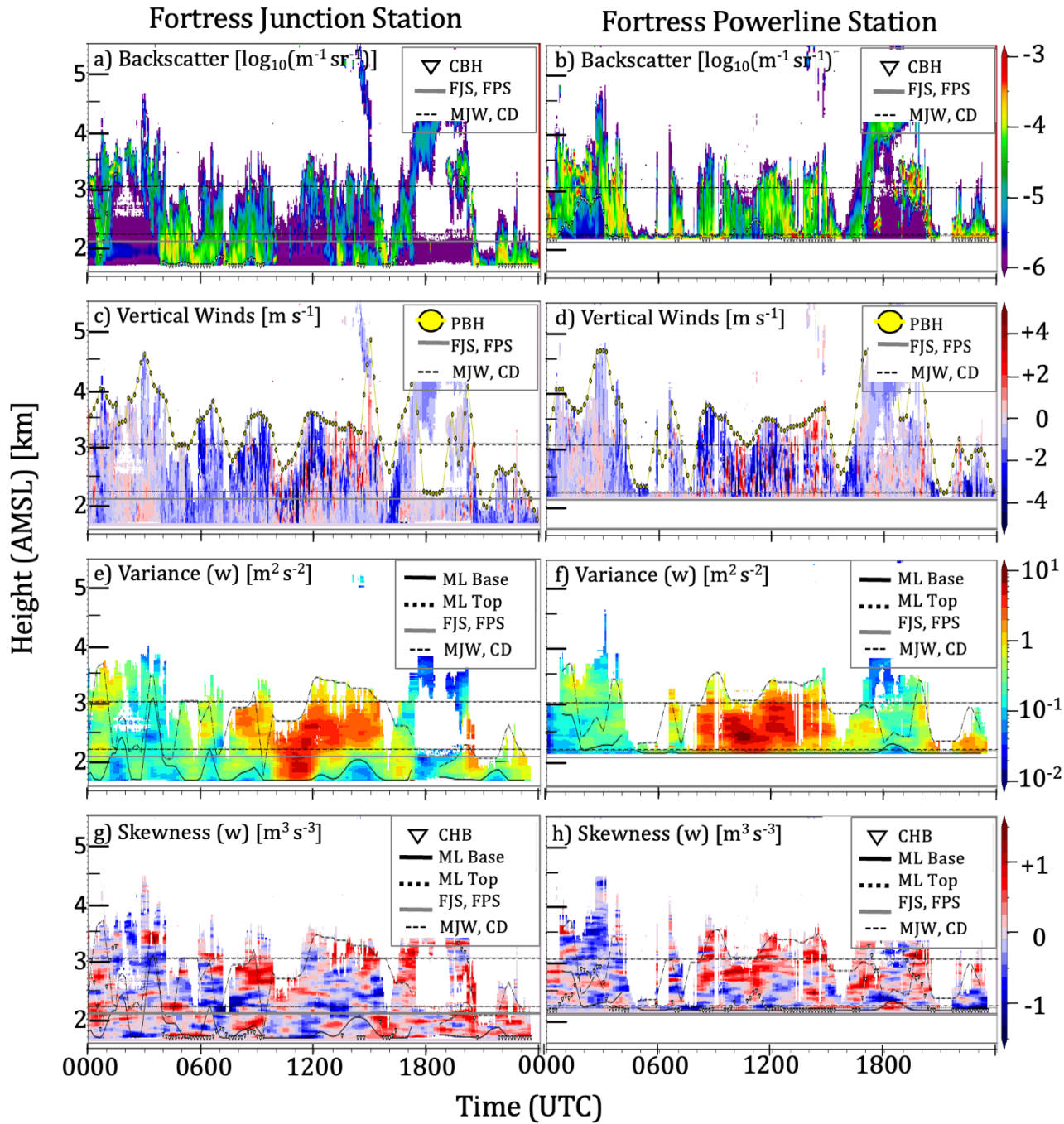


Figure 1.14 - Time-height section on the 27 April 2019 during the precipitation event #1 from collected Doppler Lidar measurements at FJS (left) and FPS (right) sites. a-b) backscatter coefficient with higher (lower) values indicating more (less) reflectivity. Inverted triangles correspond to the cloud-base-height (CBH).; c-d) Vertical velocity with blue (red) indicating downward (upward) motions. Yellow dots indicate the planetary boundary layer (PBL) height.; e-f) Variance of the vertical velocity with larger (lower) values in red (blue).; g-h) Skewness of the vertical velocity with blue (red) indicating negative (positive) values. a-h) Grey solid horizontal lines represent FJS and FPS heights and black dotted lines illustrate Mount James Walker (MJW) and the continental divide (CD)'s heights. e-h) ML base (top) heights are given by the solid (dashed) lines.

During the event #1, the diurnal cycle of PBL was affected by the cloud cover (fig. 14 a, b). It dampened the surface temperature variations leading to quasi-constant temperatures ($\sim -1^\circ\text{C}$ at FJS and $\sim -3^\circ\text{C}$ at FPS) from 0600 UTC to 1800 UTC 27 April 2019 (fig. 6b). The sharp loss of lidar's signal with height, and the extinguishment of backscatter values within the cloud or above the cloud indicates the presence of optically thick clouds. These optically thick clouds limit the income of solar radiation at the surface reducing surface heating. It diminished the diurnal convective turbulence, especially for synoptically driven clouds forming significant sky coverage.

Vertical motions were mainly downward, especially from 0300 UTC to 1800 UTC when surface winds were southerly. Because the precipitating particles generally move downward, their passage through the lidar's beam can contaminate partially the air motion measurements, increasing the contribution of downward motion. The precipitation can also have an entrainment effect on the surrounding air, enhancing the downward motions of the air in addition to the downward motion of the precipitation. However, the measurement of the vertical motions (fig. 14 c, d) revealed a mixt of upward and downward motions from ~ 0800 UTC to 1600 UTC of 27 April 2019. This upward motion, embedded in precipitation and downward air motion denotes the presence of turbulence during this same period.

In contrast with the reference day (29 May 2019, section 7a) where the flow was laminar at nighttime (from 0200 UTC to 1700 UTC) and turbulent in the afternoon (from 1700 UTC to 0000 UTC), during the event #1, the turbulence remained during the night, witnessing turbulence initiated by another source than solar convection. At both sites the turbulence was high ($\sigma_w^2 \sim 3 \text{ m}^2 \text{ s}^{-2}$) between ~ 0800 UTC and ~ 1600 UTC, prior to the maximal precipitation rate. A mixing layer, of varying height and depth, existed all day, also in opposition to the diurnal oscillation of reference day. The maximum of turbulence was measured at ~ 200 m above the surface around ~ 1100 UTC when the VWS was maximal (fig. 10). In particular, both sites reached σ_w^2 values of the order of $\sim 10 \text{ m}^2 \text{ s}^{-2}$ (fig. 14 e, f, these), respectively at ~ 1030 UTC at FPS and approximately 1 h later (~ 1130 UTC) at FJS. This occurred during a pause in precipitation, when the VWS was maximal at both sites and during a sharp increase in the surface horizontal SW winds at FPS (section 1.6.2). Precisely, between 1000 UTC and 1300 UTC, the significant precipitation paused, and the retrieved CBH rose above the ground: Ceilings remained within the first km above the surface at FPS while no cloud base was captured by the FJS's lidar at that moment. The strongest vertical winds (greater than 3 m s^{-1}) were also captured during this period of maximal turbulence. The high values (greater than 0.5 s^{-1}) of VSW (fig. 8 c, d) indicates that the dynamical component contributes

significantly to the turbulence during this event. The lidar skewness (fig. 14 g, h) analysis reveals that the maximal turbulence of the event #1 occurred, at both sites, at heights and time corresponding to a layer of positive skewness values located over a layer of negative skewness, with greater values of skewness at FPS than at FJS. Combining this lidar analysis with the simultaneous small temperature increases, the CBH rise and the precipitation pause, it indicates surface warming and cooling aloft both contribute to the turbulence. Hence, the turbulence originated from a combination of VWS, surface-heating and cooling-aloft (fig. 8, fig. 14 g, h).

Due to the strong lidar's signal attenuation by the clouds and precipitation, the PBL height retrieved by the algorithm corresponds to the altitude where the signal was lost. Furthermore, this strong precipitation rate caused the scavenging of fine aerosol particles, also limiting data availability shortly after strong precipitation occurrence.

At other times, notably from 0100 UTC to 0300 UTC and from 1000 UTC to 1300 UTC, the CBH rose above the ground. However, at FPS site, the CBH remained lower than the CD's height and more precisely, within the first km above the surface (fig. b, h, shown by downward triangle). Finally, the CBH was the highest, above the CD, between 1700 UTC and 2000 UTC right when the low-pressure center passed east to Fortress and the wind switched from southerly to northerly.

1.7.3 Vertical Fine-Scale Flow-Field and Turbulence of the Event #8

The event #8 occurred the day after the reference clear sky day. As detailed in the section 7a, on 29 May 2019, the diurnal thermic cycle led to atmospheric instability and clouds. This influenced the atmospheric conditions on the 30 May 2019, with instability remaining with σ_w^2 between $0 \text{ m}^2 \text{ s}^{-2}$ and $1 \text{ m}^2 \text{ s}^{-2}$ (fig. 15 e, f), especially from 0000 UTC to 0500 UTC when a mixing layer existed from the ground to ~ 3 km high. Light upward vertical winds were recorded at that time and heights (fig 15 c, d). At FPS, the turbulence was initiated from below the air parcel between the surface and the CD's height and from above it from the CD's height to the CBH.

Moreover, the clouds formed the previous night (29 May 2019) were still present until 0600 UTC at ~ 4.5 km height at both sites. Associated downward motion was measured under these clouds from 4.5 km to 3.5 km high (fig. 15 a, b). The β values greater than those characteristic of the PBL suggest these

downdrafts are virga. From \sim 0500 UTC to \sim 1200 UTC during the early night-time, a calm atmosphere, similarly to the night of the reference case (29 May 2019) occurred (fig. 15 c, f). Precipitation gauge data indicated precipitation during that period, which disagrees with the disdrometer data that detected no significant precipitation. Considering the lidar data showing no cloud at that time, this period was considered as a non-precipitation period, and instrumental issues with the precipitation gauge are suspected for that specific case.

During the event #8 on 30 May 2019, turbulence was measured from 1300 UTC to 2030 UTC and was driven by cooling aloft, and was associated with strong downward motion and precipitation. Here again, this is in opposition with the reference day on 29 May 2019 (section 1.7) which was characterized by strong upward motion during a clear-sky afternoon from 1700 UTC to 0000 UTC. That turbulent time of event #8 (from 1300 UTC to 2030 UTC) corresponds to non-negligible surface horizontal winds at FJS (fig. 7c).

More specifically, at FPS around 1200 UTC, the CBH started to move downward from 4.5 km to 3 km high and the cloud base reached an altitude close to that of the CD at \sim 3 km (fig. 15 a). The precipitation reached the surface a little before \sim 0100 UTC, in rain at both sites. At FPS at that corresponding time, the temperature decreased, and the dew point increased (fig 7b). The turbulence intensity increased, and a ML formed from the surface to \sim 3.5 km high at both sites (fig. 15 e, f). Between 1230 UTC and \sim 1400 UTC, FPS experienced intense turbulence, with its maximum at $\sigma_w^2 \sim 10 \text{ m}^2 \text{ s}^{-2}$ from the ground to above the CD (fig. 15 e, f). This period corresponds to that of the maximal downward velocity with $w \sim 4 \text{ m s}^{-1}$, in which upward motion was embedded (fig. 15 c, d). Hence, in these conditions, the rapid downward motion measurement is dominated by the hydrometeors.

The skewness analysis reveals that, for both sites from \sim 1300 UTC to \sim 1500 UTC, the convection was initiated from above the air parcel, meaning it is driven by endothermic phase changes such as evaporation or melting. The rapid increase in the local relative humidity corroborates the presence of evaporation. However, the lidar measurements include the velocity of hydrometeors and not only of aerosols, as discussed previously. Moreover, the turbulence weakened at FJS during the rain intermittence at \sim 1600 UTC, supporting the precipitating particles contributing to the downward motion measurements and the associated retrieved turbulence. Furthermore, from 1300 UTC to 2100 UTC, downward motion and precipitation caused scavenging of the PBL at both sites, as indicated by the vertical stripes of decreased β values (fig. 15 a, b).

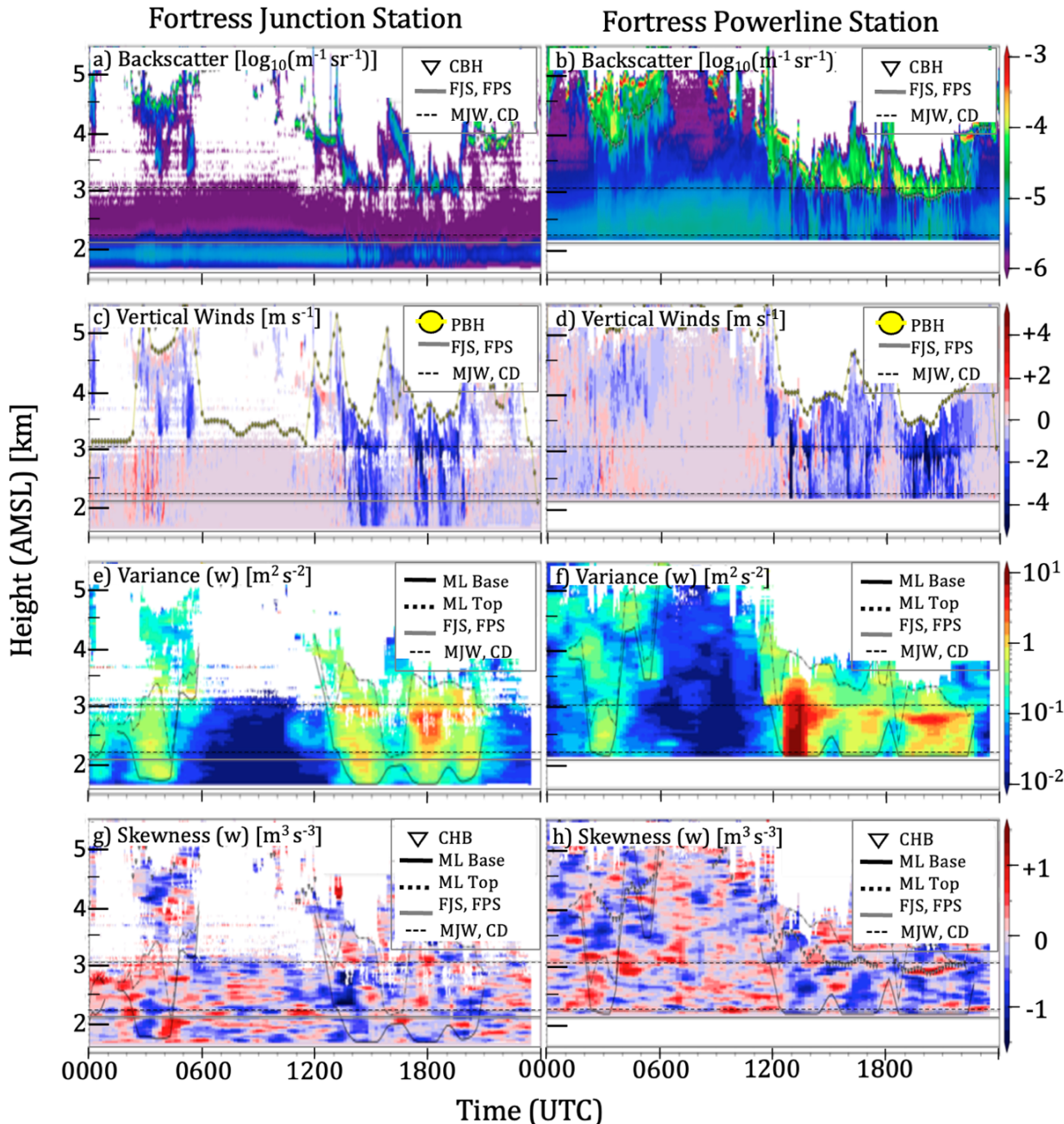


Figure 1.15 - Time-height section on the 30 May 2019 during the precipitation event #8 from collected Doppler Lidar measurements at FJS (left) and FPS (right) sites. a-b) backscatter coefficient with higher (lower) values indicating more (less) reflectivity. Inverted triangles correspond to the cloud-base-height (CBH).; c-d) Vertical velocity with blue (red) indicating downward (upward) motions. Yellow dots indicate the planetary boundary layer (PBL) height.; e-f) Variance of the vertical velocity with larger (lower) values in red (blue).; g-h) Skewness of the vertical velocity with blue (red) indicating negative (positive) values. a-h) Grey solid horizontal lines represent FJS and FPS heights and black dotted lines illustrate Mount James Walker (MJW) and the continental divide (CD)'s heights. e-h) ML base (top) heights are given by the solid (dashed) lines.

At \sim 1900 UTC, a second intensity peak of rain was recorded at FJS but no significant precipitation was measured by the precipitation gauge at FPS. However, the precipitation rate measured by the disdrometer is non-negligible, specifically, the precipitation rate of that second rainfall equals the half of the intensity of that of the rainfall that occurred at \sim 1300 UTC. Here again, based on the lidar data of backscatter and vertical velocity, precipitation is diagnosed (fig. 15 a-d). For this period, the cloud base height is very similar to the continental divide's height, respectively \sim 2.8 km at FPS and \sim 3.0 km at FJS.

Moreover, at both sites, abrupt changes in both β values and downward velocities were observed at the altitudes of the cloud bases. This indicates changes in the characteristics of the particles, such as their sizes and fall speeds. Surface weather stations revealed stable temperatures and humidity during that period at both sites. Furthermore, from \sim 1900 UTC to \sim 2030 UTC, disdrometer data indicates precipitation with an increased fall speed and smaller size, suggesting the melting layer to get higher.

At FPS, the turbulence was stronger than at FJS and was maximal at the altitude of between \sim 2.6 km and 2.8 km, hence slightly below the detected cloud base \sim 2.8 km (fig. 15 b, h). Specifically, the detected CBH corresponded to a thin layer of strong positive skewness (fig. 15 f). This suggests seeding cloud-precipitation formation with the positive skewness associated with condensation (liquid and/or solid) of supercooled water-droplets into precipitating particles. In fact, exothermal phase change generated positive buoyancy characterized by the positive skewness. Moreover, the latent heat released can corresponds to the height of the melting layer with temperatures increasing above 0 °C.

Just below the cloud base, accelerated downward velocities were measured (fig. 15 d) and maximum turbulence was observed with $\sigma_w^2 \sim 5 \text{ m}^2 \text{ s}^{-2}$ (fig. 15 f), where the skewness was negative (fig. 15 h) indicating turbulence initiated from above the air parcels. Precipitation under the CBH resulted in turbulence production by evaporative cooling into an unsaturated atmosphere, along with a decrease in the downward motion velocity. Finally, around 2100 UTC, the atmosphere became calm again as the event #8 was over and the cloud base rose to up to 4 km.

1.7.4 Vertical Fine-Scale Flow-Field and Turbulence of the Event #13

For event #13, the cloud-precipitation base was detected at low heights, removing a lot of the lidar data. Consequently, the vertical extent of the lidar data presented in this section is limited, in comparison to the other events (sections 1.7.1 - 1.7.3).

Initially, around 0100 UTC at FJS, the CBH was measured at ~ 2.1 km and at FPS, the cloud base was directly at the ground-level (fig. 16 a, b). The high backscatter values at FPS, $\beta \sim 10^{-3.5} \text{ sr}^{-1} \text{ m}^{-1}$ (fig. 16 b) were due to the heavy rain and snow pellets precipitation rate occurring at that time (fig. 8 d). At FJS, the backscatter values of the clouds ($\beta \sim 10^{-4} \text{ sr}^{-1} \text{ m}^{-1}$) were above that of the precipitation, $\beta \sim 10^{-5.5} \text{ sr}^{-1} \text{ m}^{-1}$, under the cloud to near the surface (fig. 16 a). At the beginning of the day, both sites had light-to-moderate turbulence, $\sigma_w^2 \sim 1 \text{ m}^2 \text{ s}^{-2}$ (fig. 16 e, f), in their planetary boundary layer (PBL). In fact, their mixing layer heights were equal to the PBL heights from 0100 UTC to 0500 UTC (fig. 15 c-f), initially of ~ 2.5 km and lowering and weakening until it vanished at both sites, respectively between 0700 UTC and 1000 UTC at FJS, and earlier between 0500 UTC and 0800 UTC at FPS. It corresponds to the period of weak horizontal winds and wind shear (section 1.6.4).

From 0100 UTC, FJS data showed clearly negative skewness values under the cloud base and positive skewness values from the CBH and above (fig. 16 g). Under the cloud, this indicates evaporative cooling as the precipitation fell into drier atmospheric conditions. The warming induced turbulence in the cloud, was associated with solar warming at cloud top or exothermal phase change in the clouds, as only weak VWS was measured. Specifically, the optical disdrometer indicated a mixt of rain and snow pellets turning into wet snow at ~ 0400 UTC. The solidification of the precipitation released latent heat causing local heat to increase and positive buoyancy. Moreover, downward motion velocities were maximal just under the CBH, corresponding to the precipitation falling. The CBH lowered until it reached the ground level ~ 0600 UTC. The turbulence was the weakest at both sites from 0600 UTC to 0900 UTC.

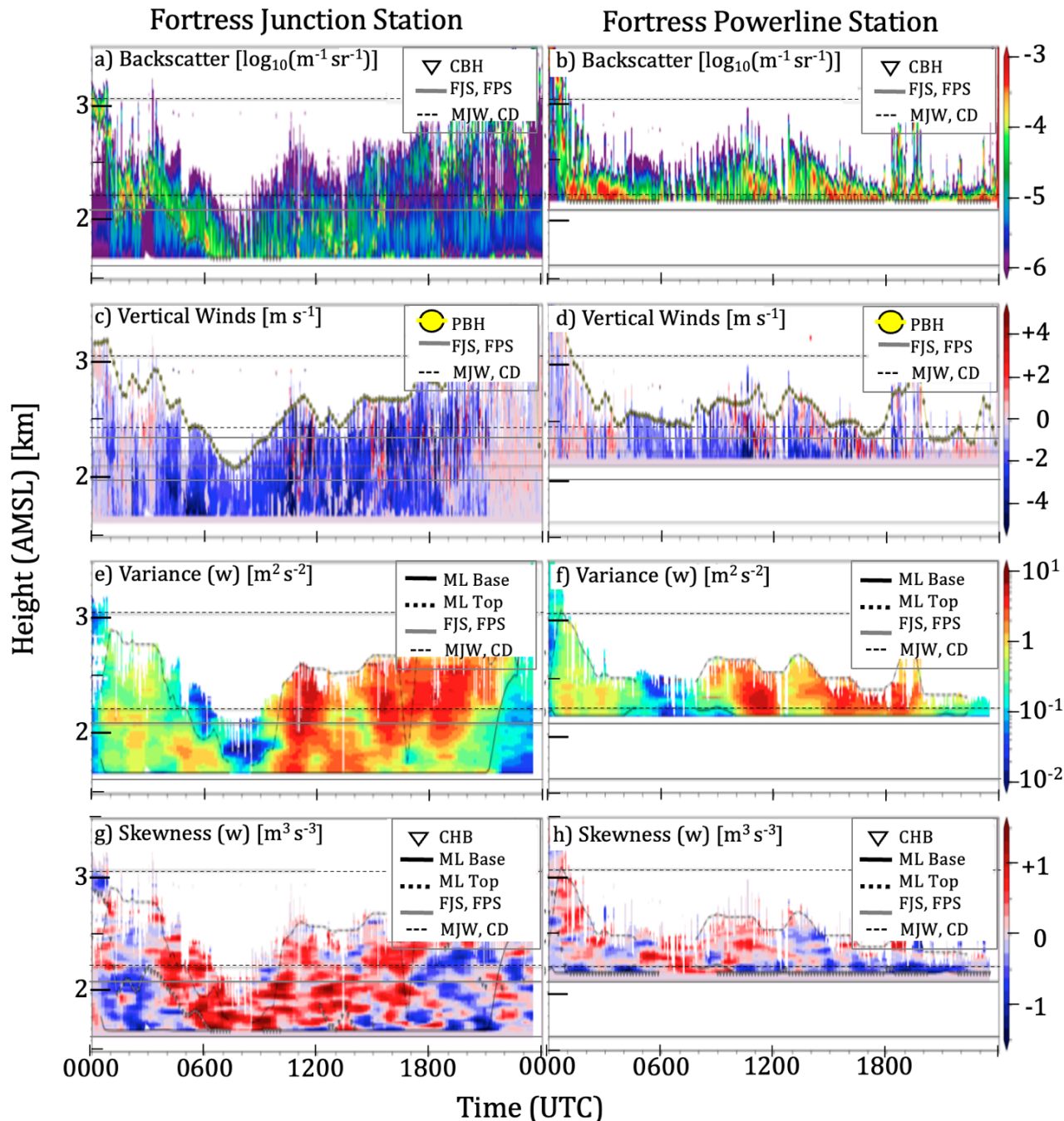


Figure 1.16 - Time-height section on the 21 June 2019 during the precipitation event #13 from collected Doppler Lidar measurements at FJS (left) and FPS (right) sites. a-b) backscatter coefficient with higher (lower) values indicating more (less) reflectivity. Inverted triangles correspond to the cloud-base-height (CBH).; c-d) Vertical velocity with blue (red) indicating downward (upward) motions. Yellow dots indicate the planetary boundary layer (PBL) height.; e-f) Variance of the vertical velocity with larger (lower) values in red (blue).; g-h) Skewness of the vertical velocity with blue (red) indicating negative (positive) values. a-h) Grey solid horizontal lines represent FJS and FPS heights and black dotted lines illustrate Mount James Walker (MJW) and the continental divide (CD)'s heights. e-h) ML base (top) heights are given by the solid (dashed) lines. Vertical axes are of reduced extent in comparison to figures 13-15 to better suit the data.

1.7.5 RELATIVE CONTRIBUTION OF TURBULENCE SOURCES

To assess the relative contributions of mixing sources during the whole field campaign period, the vertical profiles of daily mean and standard deviation of the skewness are retrieved (fig. 17), based on the proportions of positive and negative skewness values associated with turbulence. We distinguish between the turbulent mixing induced by below an air parcel (fig. 17a) and the turbulence initiated by above the air parcel by cooling aloft or VWS (fig. 17b). The turbulent mixing induced by below an air parcel included the combined effect of both processes of surface warming and vertical wind shear, that needs to be distinguished subsequently by additional analysis to the skewness.

Mean values of skewness contributions lies between 40 % and 62 %. This corresponds to a narrower range than that obtained by Huang, et al., (2020) with values laying between 25 % and 45 %. Their results show that surface warming and vertical wind shear were the main driver of the turbulence, especially in the lower 800 m AGL with a contribution of ~ 45 % near the surface. Hence, unstable PBL can lead to cloud formation such as stratocumulus and in cases of humid atmosphere to convective precipitation showers. Huang, et al., (2020) also obtained a cloud radiative cooling contribution of ~ 32 % and increased with height to peak at ~ 800 m AGL due to clouds at altitude of ~ 1 km AGL. These heights of 800 m can correspond to the top of the PBL or to the ACL height, where convective clouds a formed, explaining the radiative cooling at that height, by the cloud top emissions.

In this study, at 1.8 km AMSL (~200 m AGL at FJS), the relative contributions of the different processes were approximately similar (~ 50 %), indicating no dominant driver. However, the contribution of surface warming and VWS increased in the first next few tens of meters, with FJS data revealing a contribution of 55 % at mid-height of the valley (~ 1.9 km). From ~ 2.0 km to ~ 2.2 km AMSL, their contribution decreased, becoming <50 %, at the expense of the cooling aloft reaching a local maximum at both sites (~ 48 % at FJS; ~ 45 % at FPS).

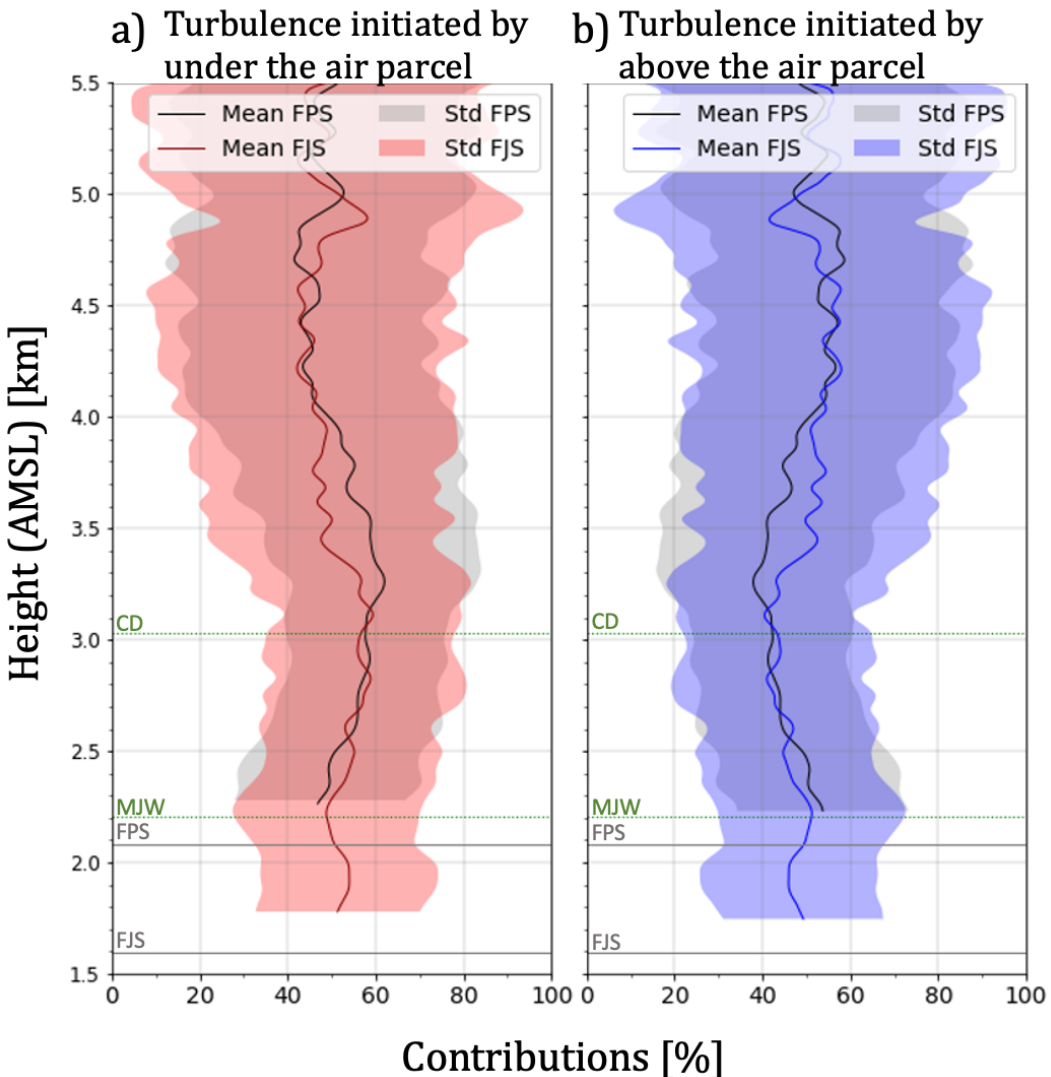


Figure 1.17 - Statistic of the relative contributions of turbulences sources at both sites as retrieved from lidars data. a) Mixing induced by under the air parcel (combination of surface warming and shear). b) Mixing induced by above the air parcel due to cooling. On both panels, horizontal grey lines represent the altitude of both lidar's sites FJS and FPS and green dotted lines identify the altitude of MJW and the CD.

From the MJW's height, the combined contribution of warming below and vertical wind shear increased with altitude at both sites. At FJS, the maximal contribution (~59%) associated with positive skewness was measured at heights close to that of the continental divide, at ~2.8 km and ~3.1 km AMSL. Then, it decreased with height to become < 50 % at ~3.4 km AMSL. At FPS, the maximal combined contribution of warming below and VWS was ~62 % at ~3.2 km AMSL. As in FJS, it decreased with height, but at a lower rate at FPS to become < 50 % at ~4 km.

In contrast, cooling of an air parcel aloft was the main contributor ($\sim 52\%$ at FJS; $\sim 55\%$ at FPS) to the turbulent mixing at the top of the valley at Mount James Walker's (MJW) height. The occurrence of cloud base height detected at this altitude was common during the fields campaign, as during the event #8. Hence, radiative cooling by these clouds, virga's evaporative cooling of precipitation into dryer air were responsible for this cooling aloft turbulence. Furthermore, the melting of solid hydrometeor into rain contributed to negative skewness and are counted in this category. The relative contribution to turbulence of the cooling aloft decreased from the MJW's height to the continental divide's height to $\sim 42\%$ at both sites. Furthermore, it increased again with altitude to reach another maximum above 4 km AMSL. At that height, the standard deviations are larger and indicate a less significative contribution of any source.

1.8 DISCUSSION AND CONCLUSIONS

During the Storm and Precipitation Across the Continental Divide Experiment (SPADE) field campaign that Thériault et al., (2022) held from April to June 2019 in the Canadian Rockies 13 precipitation events were documented. On the eastern side of the Canadian Rockies in Alberta, two observations sites were set up with in-situ and remote sensing instruments along the same slope of Fortress Mountain. Doppler lidars measured the flow-field and low-levels clouds and precipitation layers at both sites, respectively at Fortress Junction Station (FJS) in the valley bottom (1591 m) and at Fortress Powerline Station (FPS) higher on the mountain (2976 m). Optical disdrometers were used to characterize hydrometeor types collected at the surface and classified in 4 categories: rain, snow pellets (also known as graupels), wet snow and dry snow.

From the 13 precipitation events presented during SPADE (Thériault et al., (2021); (2022)), three storms were selected to investigate the fine-scale flow-field, precipitation and atmospheric conditions in the Kananaskis Valley and on the Fortress Mountain. They were compared with a clear-sky reference day, in order to compare the turbulence sources and intensities, in particular initiated by the solar surface warming in clear sky in opposition to in cloudy situations. We compared atmospheric behaviours on the mountain and in the valley for all 4 cases. Stare scans were used to characterize the PBL content in aerosols, mixing layer, clouds and precipitation layers. Moreover, the vertical wind, its variance and skewness were used to characterize the turbulence intensity origin. We distinguished between thermic turbulence induced by surface warming and by cooling aloft. The VAD scans provide 3D winds flied above both sites and indicate the presence of vertical wind shear of the horizontal wind driving the dynamical

turbulence. Surface measurements show that the wind in the PBL near the surface is primarily north-northwesterly and southerly during precipitation events, and more evenly distributed over all the directions during fair weather. A decoupling of the wind flow with height is shown in the data. Horizontal winds aloft the height of the continental divide follow large-scale patterns of circulations.

We measured PBL heights of ~ 2 km AGL in the valley at FJS and ~ 3 km AGL on Fortress Mountain at FPS, typically thicker than values ranging from 1 km to 2 km reported in previous studies (Barlow, et al., 2011; Huang, et al., 2020). These thicker PBL are probably induced by the complex terrain, in comparison with mid-latitude urban areas. At both stations, the PBL deepened when convection was diagnosed and became shallower in stable atmospheric condition.

Diurnal solar surface warming led to the development of a convective planetary boundary layer, resulting in updrafts which sometimes reached the condensation level leading to cloud formation. The turbulence induced by this surface warming was maximal under clear sky conditions, as in the reference day on 29 May 2019, with variance of $\sigma_w^2 \sim 3 \text{ m}^2 \text{ s}^{-2}$ developing during local afternoon (~ 1700 UTC) and lasting until the night (~ 0100 UTC the following day). Cloudy conditions damped this effect, modifying the periods and intensities of maximal turbulence. During the precipitation events, the turbulence was due to a mixture of diabatic cooling aloft driven by endothermic phase change, warming below driven by both solar heating and exothermic melting, along with dynamical turbulence driven by vertical wind shear. The precipitation type has an influence on the turbulence in the PBL through the thermodynamical variations resulting from the phase change occurring in the atmosphere. Strong turbulence occurred with variance as intense as $\sigma_w^2 \sim 10 \text{ m}^2 \text{ s}^{-2}$ during the precipitation events, with these maximum lasting only 1-2 h. The turbulent conditions were associated with the development of a mixing layer, duration which corresponds to presence of precipitation.

Various turbulence intensities and processes were measured during the selected events. Firstly, during event #1, a well-developed low-pressure system brought 32.5 mm of wet snow and snow pellets over Fortress at FPS site. The turbulence was of $\sigma_w^2 \sim 3 \text{ m}^2 \text{ s}^{-2}$ at both sites between ~ 0800 UTC and ~ 1600 UTC, just prior to the maximum precipitation rate. The maximum of turbulence was reached at ~ 200 m AGL at ~ 1100 UTC. Secondly, during event #8, the passage of a weak low-level system north of Fortress brought 6.5 mm of rain. The turbulence was significantly stronger at FPS than at FJS. From 1230 UTC to 1400 UTC, FPS measured values of $\sigma_w^2 \sim 10 \text{ m}^2 \text{ s}^{-2}$ from the surface to the continental divide's

height, corresponding to the first rainfall. The second rainfall was associated with turbulence at the cloud base height (CBH) and in a seeding cloud-precipitation formation situation. Thirdly, during event #13, 56.0 mm of rain and wet snow affected our sites due to another low-pressure system supported at 500 hPa. The precipitation was intense, decreasing the amount of available lidar data, especially at FPS. However, FJS data revealed turbulence for most of the event. From 0100 UTC to 0700 UTC, light-to-moderate turbulence with values of $\sigma_w^2 \sim 1 \text{ m}^2 \text{ s}^{-2}$ was driven by a mixture of evaporative cooling under the cloud and freezing warming into the cloud associated with the phase change of hydrometeor at the surface from rain to wet snow. Delays in precipitation intensity peaks at the surface were observed in the valley compared to the Mountain due to the required time for the drier levels to allow condensed particles to reach to ground before evaporating. Overall, different intensities and sources of turbulence at different times and altitudes, depending on atmospheric conditions and precipitation types at the surface and aloft. In opposition, clear-sky days turbulence was limited to surface warming and large diurnal temperature variation at the surface, especially in the valley bottom.

This observational nature of this study raises necessarily a few instrumental limitations. First, Doppler lidars allowed to measure tridimensional winds, PBL's characteristics, and cloud and precipitation layers above each site. However, high precipitation intensity can reduce significantly the lidar's range of measurement, due to attenuation of the lidar's signal by the water/snow particles. In particular, this phenomenon limited the range of available lidar data during event #13. The lower 60 m AGL also constitutes the lidar's blind zone, and in-situ weather transmitter were used in this study to cope for the missing low-level winds data, leading to a gap in winds data between the surface and 60 m AGL. Moreover, precipitation gauges sometime under- or overestimated the precipitation amount reaching the surface. In those cases, the errors in the measurements were detected by crossing the information of other instruments, such as the Parsivel's precipitation flux, and the lidar's backscatter. Consequently, we based our analyses on Parsivel's flux data and lidar's backscatter data to assess the presence of significant precipitation.

Finally, the collected dataset provides crucial added value, considering the lack of observations in remote and hard to access areas and the predominance of studies conducted in other regions of the world. The addition of automatic observations in altitude in remote areas where observers and radio-sounding launches are sparse could help to measured flow-field and hydrometeor formation and precipitation processes. A better understanding of these processes will help improving our understanding of the

atmospheric conditions and the associated fine-scale flow-field associated with spring precipitation events Kananaskis Valley, Calgary, Alberta. interactions between precipitations and fine-scale flow-field. These will contribute to improve modelling and forecasting of precipitation over complex terrain.

ANNEXE A

HYDROMETEOR TYPES DIAGNOSIS

Using disdrometers, hydrometeors were classified in four categories: rain (R), snow pellets also known as graupels (G), wet snow (WS), and dry snow (DS) (Table 3). To do so, empirical relationships between hydrometeor types and their characteristic diameters D and fall speed v_T were used (Rasmussen, Vivekanandan, Cole, Myers, & Masters, 1999; Ishizaka, et al., 2013). The later parameters are linked throughout power laws:

$$v_T(D) = aD^b \quad (7)$$

with a , b being coefficient values proper to each hydrometeor type (Table 3). For a chosen temporal period, the main hydrometeor type is obtained by computing the shortest-distance between the theoretical size - fall speed curves to the measured fall speeds and diameters coordinates of a captured particle. The nearest theoretical curve then indicates the corresponding hydrometeor type of the given time period.

Table 1.3 - Empirical relationships used for identification of hydrometeor types using equation 7 from diameter [mm] and fall speed [m s^{-1}].

Hydrometeors	Coefficient numerical values		Sources
	$a [\text{ms}^{-1}\text{mm}^{-1}]$	b	
Rain (R)	3.78	0.67	Atlas & Ulbrich (1977)
Snow pellets or graupels (G)	1.3	0.66	Locatelli & Hobbs (1974)
Wet Snow (WS)	1.35	0.2	Rasmussen, Vivekanandan, Cole, Myers & Masters (1999)
Dry Snow (DS)	0.68	0.2	Rasmussen, Vivekanandan, Cole, Myers & Masters (1999)

To ensure quality control, precipitating particles that were simultaneously too small and too slow ($D < 1.0 \text{ mm}$ and $v_T < 2.0 \text{ m s}^{-1}$) are discarded from dataset, as they are associated with weak measured signal, contaminated with instrument's noise, and because the theoretical curves intersect for these small values. Moreover, for a given diameter, particles with fall speeds superior to that of rain are considered as physically unrealistic values and are discarded through the quality control process. Similarly, particles with fall speeds inferior to that of dry snow are also discarded as they are physically unrealistic. To consider the

discrete nature of the bins, we added a 10 % tolerance margin on the fall speeds. In this paper, the term *snow pellets* indicates to *Graupels* (G) or *ice pellets* (IP) or and refers to supercooled water droplets freezing onto an ice crystal by a process called rimming (NOAA).

CONCLUSION

Dans le cadre du projet *Storm and Precipitation Across the Continental Divide Experiment* (SPADE), une campagne de terrain s'est tenue dans le sud des Rocheuses Canadiennes entre avril et juin 2019. Les données recueillies lors de cette campagne ont permis de mesurer et documenter 13 événements de précipitation. Sur le côté à l'est de la division continentale, deux sites d'observations ont été mis en place sur la montagne Fortress et dans la vallée de Kananaskis, en Alberta, respectivement *Fortress Powerline Station* (FPS) situé sur la montagne Fortress (2076 m AMSL) et à *Fortress Junction Station* (FJS) dans la vallée de Kananaskis (1591 m AMSL). Des instruments de mesures in-situ et de télédétection fut déployés. Des lidars Doppler ont permis de mesurer l'écoulement à fine-échelle et les couches de nuages et de précipitations au-dessus de chaque site. Des disdromètres optiques ont été utilisés pour caractériser les types d'hydrométéores collectés à la surface, à chaque site. Les précipitations de surface ont ainsi été classées en quatre catégories: la pluie, le grésil, la neige mouillée et la neige sèche.

Une présentation générale des 13 événements de précipitations et de leurs patrons de circulation à grande-échelle est d'abord présentée afin de mettre en contexte l'apport d'humidité sur la région de chacun des événements. Trois événements choisis sont analysés et présentés plus en détails, en comparaison avec une journée de ciel-clair. Plus spécifiquement, l'écoulement de fine-échelle de chacun est présenté à l'aide des vents horizontaux obtenus par balayage *VAD* et des vents verticaux obtenus par des mesures verticales *Stare*. L'intensité de la turbulence est donnée par la variance de la vitesse verticale et est utilisée pour déterminer la présence de couche de mélange dans la structure de la couche limite planétaire. Les sources de la turbulence sont d'abord investiguées à l'aide de l'asymétrie de la vitesse verticale. Les asymétries positives indiquent que la turbulence est induite par un le cisaillement du vent ou par un réchauffement de la surface (ou un réchauffement sous une parcelle d'air donnée). Les cas d'asymétrie négatives impliquent une turbulence due à un refroidissement altitude. Le cisaillement vertical du vent horizontal est également présenté afin d'évaluer sa contribution dans les cas d'asymétries positives.

Les données d'observations lidars de rétrodiffusion (*backscatter*, en anglais) sont utilisées pour déterminer la hauteur de la couche d'aérosols dans la couche limite planétaire ainsi que la présence des couches de nuages et de précipitations et la hauteur de leur base, leur sommet étant très difficile à observer avec un lidar à 1.5 μm .

Les vents à la surface sont mesurés à l'aide des instruments in-situ puisque les premiers 60 m au-dessus du sol ne sont pas accessibles par les lidars. Nos données indiquent des vents de surface plus forts et de directions canalisés durant les évènements de précipitations (du sud ou du Nord-Nord-Ouest). Les données des lidars nous ont permis d'identifier un découplage entre les vents horizontaux plus haut que la hauteur de la division continentale de ceux plus bas. En effet, au-dessus de cette barrière orographique, les vents suivent les patrons synoptiques et présentent moins de variabilités spatiales que les vents des bas-niveaux affectés davantage par l'orographie. Les évènements majeurs de précipitations sont associés à des systèmes dépressionnaires synoptiques passant à proximité du domaine d'étude. Ainsi, la circulation cyclonique autour de ces systèmes de basse-pression engendrait la transition des vents en du Nord-Ouest à des vents d'Est en altitude.

Nous avons mesuré des épaisseurs de couche limite atmosphérique (CLA) de ~ 2 km dans la vallée et de ~ 3 km sur la montagne. Ces épaisseurs sont supérieures à celles de 1 km à 2 km des couches limites d'études précédentes telles que Barlow et al., (2011) et Huang et al., (2020) en raison de la grande complexité du terrain des Rocheuses canadiennes et de la rugosité de surface, en comparaison à ces études menées dans des régions urbaines plus planes. De plus, lorsque la couche limite étaient convective, des couches de mélange se développaient et la CLA s'épaississaient et inversement, dans des conditions stables, les couches de mélange dissipant la CLA, était alors formée d'une couche résiduelle, s'amincissait. Le réchauffement de la surface par le soleil a conduit au développement de couche limite convective et de flottabilité positive responsables de mouvements ascendants. Dans certains cas, ces mouvements ascendants ont mené à la formation de nuages par refroidissement adiabatique. Les cas de turbulence induite par le réchauffement solaire furent maximaux lors de ciels clairs, tel qu'illustre par le cas de référence du 29 mai 2019. Lors de cette journée, la turbulence s'est développée en fin d'après-midi (~ 1700 UTC) avec une variance de la vitesse verticale de $\sigma_w^2 \sim 3 \text{ m}^2 \text{ s}^{-2}$ et a persisté jusqu'en soirée (~ 0100 UTC). À l'inverse, le refroidissement nocturne des bas niveaux menait à une couche limite nocturne stable, et permettant d'observé un cycle diurne convectif en accord avec la théorie de la CLA. De façon général tout long de la campagne, la présence d'un couvert nuageux a amorti cet effet diurne en limitant les gains et les pertes radiatives. En effet, nos résultats démontrent que durant les évènements de précipitations, la turbulence était d'origine mixtes et que les périodes de turbulence maximale ne correspondaient pas au cycle diurne. Ces sources mixtes de turbulence ont inclus le brassage mécanique dû au cisaillement vertical du vent horizontal (présenté par le VWS dans notre étude), ainsi que le chauffage par-dessous et le refroidissement par-dessus d'une parcelle d'air. Ces réchauffement et

refroidissement peuvent être radiatif, comme dans le cas du réchauffement solaire à la surface terrestre ou au sommet d'une couche de nuage, mais peut également être latent, comme dans les cas de réchauffement par solidification d'eau surfondue ou de condensation de l'humidité, ou encore de refroidissement évaporatif ou de fonte. Parmi les événements investigués, la turbulence maximale était associée à une variance de l'ordre de $\sigma_w^2 \sim 10 \text{ m}^2 \text{ s}^{-2}$ pour une durée de 1 à 2 heures.

Le 27 avril 2019 lors de l'évènement #1, la CLA turbulente était caractérisée par une variance de $\sigma_w^2 \sim 3 \text{ m}^2 \text{ s}^{-2}$ pour la période de 0800 UTC à 1600 UTC, soit un peu avant le moment de précipitation maximale. Le maximum de turbulence de cet évènement fut mesuré à ~ 1100 UTC à ~ 200 m au-dessus du sol alors que le cisaillement du vent était maximum. Ainsi, le cisaillement du vent constitue la source principale de turbulence ici, en plus d'une contribution du refroidissement en altitude.

Le 30 mai 2019 durant l'évènement #8, la turbulence était significativement plus importante sur la montagne (FPS) que dans la vallée (FJS). FPS a enregistré son maximum de turbulence avec $\sigma_w^2 \sim 10 \text{ m}^2 \text{ s}^{-2}$ de 1230 UTC à 1400 UTC sur toute la profondeur de la CLA, soit de la surface à la hauteur de la division continentale, dû à du refroidissement évaporatif et des précipitations. Un second maximum de turbulence fut observé à la base du nuage à ~ 2.8 km avec $\sigma_w^2 \sim 4 \text{ m}^2 \text{ s}^{-2}$ de 1900 UTC à 2200 UTC. Une combinaison des effets de refroidissement en altitude, de cisaillement de vent et de réchauffement de solidification a mené à cette turbulence.

Le 21 juin 2019 durant l'évènement #13, la précipitation était intense, de façon à limiter le signal lidar et les données accessibles, surtout à FPS où la base de nuage fut détectée directement à la surface. Les données de FJS indiquent de la turbulence pour la majeure partie de la journée, en lien avec les précipitations, indépendamment du cycle solaire diurne. Pour la période de 0100 UTC à 0700 UTC, de la turbulence légère à modérée avec $\sigma_w^2 \sim 1 \text{ m}^2 \text{ s}^{-2}$ était causée par une combinaison de refroidissement évaporatif sous le nuage et de réchauffement dans le nuage. Ce réchauffement dans le nuage correspond à un changement de précipitation de surface de pluie vers neige mouillée, suggérant la création de flottabilité positive de réchauffement latent. Finalement, le délai temporel entre les précipitations collectés à la surface à FJS par rapport à FPS corrobore l'idée de refroidissement évaporatif dans une couche plus sèche. En effet, ce délai temporel de l'ordre de 1 à 4 heures peut s'expliquer par le temps requis pour saturer les bas niveaux par les hydrométéores.

Pour conclure, considérant le manque d'observations dans les milieu éloignés et difficiles d'accès, ainsi que le manque de données dans les Rocheuses Canadiennes, cette analyse constitue une valeur ajoutée pour la recherche scientifique des précipitations et des écoulements de fine-échelle. De plus, les lidars permettent d'observations automatiquement les conditions en altitude en complément aux stations in-situ qui mesures les conditions de surface. Dans les régions où il n'est pas possible d'avoir d'observateur humain, les lancés de radiosondages sont alors impossibles et les conditions en altitudes demeurent plutôt inconnus, surtout en terrain montagneux où la présence de l'orographie contamine les images radars. Pour terminer, cette étude contribue à améliorer notre compréhension des interactions entre les précipitations et l'écoulement de fine-échelle. Alors que les modèles ont de la difficulté à représenter l'orographie des terrains montagneux, une meilleure compréhension pourrait mener à de meilleure paramétrisation de ces processus et ainsi améliorer les prévisions numériques du temps, surtout lors d'évènements de précipitations à forts-impacts.

RÉFÉRENCES

- Ackermann, I. J., Hass, H., Memmesheimer, M., Ebel, A., Binkowski, F. S., & Shankar, U. M. (1998, September). Modal aerosol dynamics model for Europe: Development and first applications. *Atmospheric environment*, 32(17), 2981-2999.
- Almonte, J. D., & Stewart, R. E. (2019, September 12). Precipitation transition regions over the southern Canadian Cordillera during January–April 2010 and under a pseudo-global-warming assumption. *Hydrology and Earth System Sciences*, 23(10), 3665-3682.
- Atlas, D., & Ulbrich, C. W. (1977, September). Path-and area-integrated rainfall measurement by microwave attenuation in the 1–3 cm band. *Journal of Applied Meteorology and Climatology*, 16(12), 1322-1331.
- Barlow, J. F., Dunbar, T. M., Nemitz, E. G., Wood, C. R., Gallagher, M. W., Davies, F., . . . Harrison, R. M. (2011, March 9). Boundary layer dynamics over London, UK, as observed using Doppler lidar during REPARTEE-II. *Atmospheric Chemistry and Physics*, 11(5), 2111–2125.
- Battaglia, A., Rustemeier, E., Tokay, A., Blahak, U., & Simmer, C. (2010, February 01). PARSIVEL snow observations: A critical assessment. *Journal of Atmospheric and Oceanic Technology*, 27(2), 333-344.
- Berg, L. K., Newsom, R. K., & Turner, D. D. (2017, September 01). Year-long vertical velocity statistics derived from Doppler lidar data for the continental convective boundary layer. *Journal of Applied Meteorology and Climatology*, 56(9), 2441-2454.
- Blifford Jr, I. H., & Ringer, L. D. (1969). The Size and Number Distribution of Aerosols in the Continental Troposphere. *Journal of Atmospheric Sciences*, 26(4), 716-726.
- Bossert, J. E., Sheaffer, J. D., & Reiter, E. R. (1989, July 01). Aspects of regional-scale flows in mountainous terrain. *Journal of Applied Meteorology and Climatology*, 28(7), 590-601.
- Browning, K. A., & Wexler, R. (1968, Feb 01). The determination of kinematic properties of a wind field using Doppler radar. *Journal of Applied meteorology and climatology*, 07(01), 105-113.
- Collaud Coen, M., Praz, C., Haefele, A., Ruffieux, D., Kaufmann, P., & Calpini, B. (2014, Dec 11). Determination and climatology of the planetary boundary layer height above the Swiss plateau by in situ and remote sensing measurements as well as by the COSMO-2 model. *Atmospheric Chemistry and Physics*, 14(23), 13205-13221.
- De Arruda Moreira, G., Guerrero-Rascado, J. L., Bravo-Aranda, J. A., Benavent-Oltra, J. A., Ortiz-Amezcua, P., Róman, R., & Alados-Arboledas, L. (2018, Nov 15). Study of the planetary boundary layer by microwave radiometer, elastic lidar and Doppler lidar estimations in Southern Iberian Peninsula. *Atmospheric Research*, 213, 185-195.
- Gerber, F., Mott, R., & Lehning, M. (2019, Feb 01). The importance of near-surface winter precipitation processes in complex alpine terrain. *Journal of Hydrometeorology*, 20(2), 177-196.

- Gonzalez, S., Bech, J., Udina, M., Codina, B., Paci, A., & Trapero, L. (2019, May 01). Decoupling between precipitation processes and mountain wave induced circulations observed with a vertically pointing K-band doppler radar. *Remote Sensing*, 11(9).
- Grange, S. K. (2014). *Technical note: Averaging wind speeds and directions*. Research Gate.
- Hauer, F. R., Baron, J. S., Campbell, D. H., Fausch, K. D., Hostetler, S. W., Leavesley, G. H., & Stanford, J. A. (1997, Dec 04). Assessment of climate change and freshwater ecosystems of the Rocky Mountains, USA and Canada. *Hydrological Processes*, 11(8).
- Henn, B., Clark, M. P., Kavetski, D., Newman, A. J., Hughes, M., McGurk, B., & Lundquist, J. D. (2018, Jan). Spatiotemporal patterns of precipitation inferred from streamflow observations across the Sierra Nevada mountain range. *Journal of Hydrology*, 556, 993-1012.
- Hersbach, H., Bell, B., Berrisford, P., & Hirahara, S. (2020, June 15). The ERA5 global reanalysis. *Quarterly Journal of the Royal Meteorological Society*, 146(730), 1999-2049.
- Hogan, R. J., Grant, A. L., Illingworth, A. J., Pearson, G. N., & O'Connor, E. J. (2009, April). Vertical velocity variance and skewness in clear and cloud-topped boundary layers as revealed by Doppler lidar. *Quarterly Journal of the Royal Meteorological Society: A journal of the atmospheric sciences, applied meteorology and physical oceanography*, 135(640), 635–643.
- Houze Jr, R. A. (2012, March). Orographic effects on precipitating clouds. *Reviews of Geophysics*, 50(1).
- Huang, T., Yim, S. H., Yang, Y., Lee, O. S., Lam, D. H., heng, J. C., & Guo, J. (2020, May 11). Observation of turbulent mixing characteristics in the typical daytime cloud-topped boundary layer over Hong Kong in 2019. *Remote Sensing*, 12(9), 1533.
- Illingworth, A. J., Cimini, D., Haefele, A., Haeffelin, M., Hervo, M., Kotthaus, S., & Potthast, R. (2019, April 01). How can existing ground-based profiling instruments improve European weather forecasts? *Bulletin of the American Meteorological Society*, 100(4), 605-619.
- Ishizaka, M., Motoyoshi, H., Nakai, S., Shiina, T., Kumakura, T., & Muramoto, K. I. (2013). A new method for identifying the main type of solid hydrometeors contributing to snowfall from measured size-fall speed relationship. *Journal of the Meteorological Society of Japan*, 91(06), 747-762.
- Kim, K., Bang, W., Chang, E. C., Tapiador, F. J., Tsai, C. L., Jung, E., & Lee, G. (2021). Impact of wind pattern and complex topography on snow microphysics during ICE-POP 2018. *Atmospheric Chemistry and Physics Discussions*, 21(15), 1-36.
- Lehning, M., Löwe, H., Ryser, M., & Raderschall, N. (2008, July). Inhomogeneous precipitation distribution and snow transport in steep terrain. *Water Resources Research*, 44(07).
- Lenschow, D. H., Wulfmeyer, V., & Senff, C. (2000, Oct 01). Measuring second-through fourth-order moments in noisy data. *Journal of Atmospheric and Oceanic technology*, 17(10), 1330-1347.
- Lilly, D. K. (1978, Jan 01). A severe downslope windstorm and aircraft turbulence event induced by a mountain wave. *Journal of Atmospheric Sciences*, 35(01), 59-77.

Locatelli, J. D., & Hobbs, P. V. (1974, May 20). Fall speeds and masses of solid precipitation particles. *Journal of Geophysical Research*, 79(15), 2185-2197.

Manninen, A. J., Marke, T., Tuononen, M., & O'Connor, E. J. (2018, August 16). Atmospheric boundary layer classification with Doppler lidar. *Journal of Geophysical Research: Atmospheres*, 123(15), 8172-8189.

Manninen, A. J., O'Connor, E. J., Vakkari, V., & Petäjä, T. (2016, March 03). A generalised background correction algorithm for a Halo Doppler lidar and its application to data from Finland. *Atmospheric Measurement Techniques*, 9(2), 817-827.

Mariani, Z., Crawford, R., Casati, B., & Lemay, F. (2020, Jan 18). A Multi-Year Evaluation of Doppler Lidar Wind-Profile Observations in the Arctic. *Remote Sensing*, 12(2), 323.

Mariani, Z., Dehghan, A., Gascon, G., Joe, P., Hudak, D., Strawbridge, K., & Corriveau, J. (2018, Feb 16). Multi-Instrument Observations of Prolonged Stratified Wind Layers at Iqaluit, Nunavut. *Geophysical Research Letters*, 45(3), 1654-1660.

Mariani, Z., Stanton, N., Whiteway, J., & Lehtinen, R. (2020, September). Toronto Water Vapor Lidar Inter-Comparison Campaign. *Remote Sensing*, 12(19), 3165.

Markowski, P., & Richardson, Y. (2011). *Mesoscale Meteorology in Midlatitudes*. John Wiley & Sons.

Milrad, S., Gyakum, J., & Atallah, E. (2015, July 01). A meteorological analysis of the 2013 Alberta flood: Antecedent large-scale flow pattern and synoptic–dynamic characteristics. *Monthly Weather Review*, 143(7), 2817-2841.

Minder, J. R., Durran, D. R., & Roe, G. H. (2011, September 01). Mesoscale controls on the mountainside snow line. *Journal of Atmospheric Sciences*, 68(9), 2107–2127.

Newsom, R. K., Sivaraman, C., Shippert, T. R., & Riihimaki, L. D. (2019). *Doppler lidar vertical velocity statistics value-added product*. DOE ARM Climate Research Facility, Washington, DC (United States), USDOE Office of Science (SC), Biological and Environmental Research (BER). Washington, DC (United States): DOE ARM Climate Research Facility.

NOAA. (s.d.). *SEVERE WEATHER 101*. Récupéré sur nssl.noaa.education: <https://www.nssl.noaa.gov/education/srvwx101/hail/types/>

O'Connor, E. J., Illingworth, A. J., Brooks, I. M., Westbrook, C. D., Hogan, R. J., Davies, F., & Brooks, B. J. (2010, October 01). A method for estimating the turbulent kinetic energy dissipation rate from a vertically pointing Doppler lidar, and independent evaluation from balloon-borne in situ measurements. *Journal of atmospheric and oceanic technology*, 27(10), 1652-1664.

Olofson, F. (2008). *Lidar Studies of Tropospheric Aerosols and Clouds*. Department of Chemistry, Atmospheric Science, University of Gothenburg. Göteborg,: Geson Hylte Tryck AB.

Päschke, E., Leinweber, R., & Lehmann, V. (2015, June 03). An assessment of the performance of a 1.5 µm Doppler lidar for operational vertical wind profiling based on a 1-year trial. *Atmospheric Measurement Techniques*, 8(6), 2251-2266.

- Pearson, G., Davies, F., & Collier, C. (2009, Feb 01). An analysis of the performance of the UFAM pulsed Doppler lidar for observing the boundary layer. *Journal of Atmospheric and Oceanic Technology*, 26(2), 240-250.
- Poirier, É., Thériault, J. M., & Leriche, M. (2019, Oct 02). Role of sublimation and riming in the precipitation distribution in the Kananaskis Valley, Alberta, Canada. *Hydrology and Earth System Sciences*, 23(10), 4097-4111.
- Pomeroy, J., Marks, D., & Fang, X. (2016, May 03). The cold rain-on-snow event of June 2013 in the Canadian Rockies — characteristics and diagnosis. *Hydrological Processes*, 30(17), 899-2914.
- Pruppacher, H., & Klett, J. (1997). *Microphysics of Clouds and Precipitation. 2nd Edition*. Atmospheric and Oceanographic Sciences Library, Springer.
- Raderschall, N., Lehning, M., & Schär, C. (2008, Sep 17). Fine-scale modeling of the boundary layer wind field over steep topography. *Water Resources Research*, 44(9).
- Rasmussen, R. M., Vivekanandan, J., Cole, J., Myers, B., & Masters, C. (1999, Oct 01). The estimation of snowfall rate using visibility. *Journal of Applied Meteorology and Climatology*, 38(10), 1542-1563.
- Ressource Naturelles Canada. (2022, 03 14). *Ressources naturelles Canada*. Récupéré sur Eau, Bassins versants: <https://ressources-naturelles.canada.ca/eau/16889>
- Reuter, G., & Yau, M. (1990, Feb 01). Observations of slantwise convective instability in winter cyclones. *Monthly weather review*, 118(2), 447-458.
- Richardson, L. F. (1922). *Weather Prediction by Numerical Processes*. London: Cambridge University Press.
- Russel, R. (2007). *Sizes of Aerosols, Raindrop and Cloud Droplets*. Récupéré sur UNIVERSITY CORPORATION FOR ATMOSPHERIC RESEARCH: <https://scied.ucar.edu/image/aerosols-raindrop-cloud-droplets-sizes>
- Steiner, M., Bousquet, O., Houze Jr, R. A., Smull, B. F., & Mancini, M. (2003, Jan). Airflow within major Alpine river valleys under heavy rainfall. *Quarterly Journal of the Royal Meteorological Society: A journal of the atmospheric sciences, applied meteorology and physical oceanography*, 129(588), 411-431.
- Stewart, R. E., & Donaldson, N. R. (1989, Nov 19). On the nature of rapidly deepening Canadian east coast winter storms. *Atmosphere-Ocean*, 27(1), 87-107.
- Stewart, R. E., & Yiu, D. T. (1993, May). Distributions of precipitation and associated parameters across precipitation type transitions over southern Ontario. *Atmospheric research*, 29(3-4), 153-178.
- Stewart, R., Bachand, D., Dunkley, R., Giles, A., Lawson, B., Legal, L., . . . Yau, M. (1995). Winter storms over Canada. *Atmosphere-ocean*, 33(2), 223-247.
- Stoelinga, M. T., Hobbs, P. V., Mass, C. F., Locatelli, J. D., Houze Jr., R. A., Colle, B. A., . . . Colman, B. R. (2003, Dec 01). Improvement of Microphysical Parameterization through Observational Verification Experiment. *American Meteorological Society*, 84(12), 1807-1826.

Stull, R. B. (1988). *An Introduction to Boundary Layer Meteorology* (Vol. 13). Springer Science & Business Media.

The Candian Press. (2023, Janvier 18). *The 10 most expensive natural disasters in Canada by insurance payouts*. Récupéré sur toronto.citynews.ca: <https://toronto.citynews.ca/2023/01/18/the-10-most-expensive-natural-disasters-in-canada-by-insurance-payouts/>

Thériault, J. M., Déry, S. J., Pomeroy, J. W., Smith, H. M., Almonte, J., Bertoncini, A., . . . Hébert-Pinard, C. (2021). Meteorological observations collected during the Storms and Precipitation Across the continental Divide Experiment (SPADE), April–June 2019. *Earth System Science Data*, 13(3), 1233–1249.

Thériault, J. M., Hung, I., Vaquer, P., Stewart, R. E., & Pomeroy, J. W. (2018). Precipitation characteristics and associated weather conditions on the eastern slopes of the Canadian Rockies during March–April 2015. *Hydrology and Earth System Sciences*, 22(8), 4491–4512.

Thériault, J. M., Leroux, N. R., Stewart, R. E., Bertoncini, A., Déry, S. J., Pomeroy, J. W., . . . Almonte, J. (2022). Storms and Precipitation Across the continental Divide Experiment (SPADE). *Bulletin of the American Meteorological Society*, 103(11), E2628–E2649.

Thériault, J. M., Rasmussen, R., Ikeda, K., & Landolt, S. (2012). Dependence of snow gauge collection efficiency on snowflake characteristics. *Journal of applied meteorology and climatology*, 51(4), 745–762.

Thériault, J. M., Rasmussen, R., Trevor Smith, Mo, R., Milbrandt, J. A., Brugman, M. M., . . . Denis, B. (2012). A case study of processes impacting precipitation phase and intensity during the Vancouver 2010 Winter Olympics. *Weather and forecasting*, 27(6), 1301–1325.

Thériault, J. M., Stewart, R. E., Milbrandt, J. A., & Yau, M. K. (2006). On the simulation of winter precipitation types. *Journal of Geophysical Research: Atmospheres*, 111(D18).

Vaisala. (2012). *User's Guide: Vaisala Weather Transmitter WXT520*. Récupéré sur vaisala.com: <https://www.vaisala.com/sites/default/files/documents/M210906EN-C.pdf>

Xue, M. (2015, Spring). *Mesoscale Meteorology - METR 4433*. Récupéré sur Center for Analysis and Prediction of Storms (CAPS): <https://twister.caps.ou.edu/MM2015/docs/chapter1/chapter1.pdf>

